Niels Bohr Institute

University of Copenhagen

Master's Thesis

Development and Characterization of MicroMegas Detectors for the Upgrade of the ATLAS Muon Spectrometer

Author:
Maria Hoffmann

Supervisors:
Joerg Wotschack (CERN)
Peter Hansen (NBI)

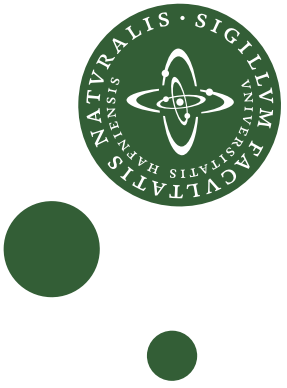

October 2013

Abstract

The scheduled upgrades of the Large Hadron Collider complex at CERN will increase the instantaneous luminosity to 5×10^{34} cm^{-2} s^{-1}. As a result, the radiation levels in parts of the ATLAS Muon Spectrometer will reach levels that are beyond the limit of safe operation of the present detector technologies. To accommodate to the post-upgrade operating conditions, the Muon Spectrometer will undergo a complete replacement of its innermost end-cap stations in 2018. The MicroMegas detector technology has been chosen as a part of the new instrumentation because of its excellent performance under high irradiation rates. Experience with this relatively new technology is rather limited, and a set of milestones therefore had to be fulfilled before the technology could be accepted by the ATLAS Collaboration. We describe an extract of the work that led to the fulfillment of these milestones. We demonstrate that adequate single-plane spatial resolution close to 100 μm can be achieved by combining the μTPC technique with the traditional charge centroid method for tracks with an inclination in the range $10^\circ - 40^\circ$. We afterwards describe the R&D efforts that led to the successful construction of the first operational 1×1.2 m^2 and 1×2.4 m^2 MicroMegas prototypes.

Acknowledgements

I am enormously grateful for my year at CERN. To have received training with instrumentation from nothing but experts has been a unique opportunity, which I feel lucky to have had and appreciate deeply. I wish to express my thankfulness to all my colleagues and friends from the MicroMegas group, the RD51 laboratory and from everyone else who contributed to making my time at CERN irreplaceable.

From the MicroMegas group I wish to thank

- My supervisor **Joerg Wotschack** for giving me the opportunity to join the MicroMegas efforts without any prior hardware-experience. Having been a part of this exciting and highly topical project has been a privilege. Thank you for your daily supervision, overall helpfulness, and for your extensive help with my thesis.
- **Givi Sekhniaidze** for providing me with laboratory skills and for teaching me basically everything I know about electronics (not an impressive amount, but still!). Thank you for your kindness and for always taking your time to explain things to me. Also thanks for our countless coffee breaks – I look forward to many more.
- **Michele Bianco** for excellent teamwork, good physics discussions and for always taking your time to answer my questions. Most of all thanks for company and cheerful times in the lab. Also thank you for introducing me to the relevant subject of number series in Italian (good thing we have a few more years to practice!).

It has been a pleasure working with you all and I look forward to more fruitful collaboration in the upcoming years.

I also owe many thanks to

- All the GEMs (**Eraldo51 Oliveri**, **Patrick Thuiner**, **Jeremie Merlin** and **Christopher Armaingaud**), **Silvia Franchino** and **Spyros Papadatos** for good times in the lab, during coffee breaks and in general. ~~A special thanks to Patrick for letting me invade your office space~~.
- My dear friend **Sune Jakobsen** for mentoring, company and for always taking your time (although you always lack it) for a coffee and a talk.
- My supervisor at NBI, **Peter Hansen**, for physics discussions and for helping me transforming my work into a thesis.
- My proof-readers: **Christine Awesome Rasmussen, Hass AbouZeid** and **Thomas Berlok**. You rock my socks!

Forewords

The author was employed as a CERN Technical Student for the period 1/7/2012 - 31/8/2013 in the PH-ADE-MU unit under the supervision of Joerg Wotschack. This thesis describes an extract of the work that was conducted throughout this period by the CERN-based ATLAS MicroMegas group, which at the time consisted of Joerg Wotschack, Givi Sekhniaidze, Michele Bianco and the author. All results presented in Chapter 6 were produced independently by the author. The hardware activities with the large chambers (L1 and L2) were performed with the support from the PH-DT and TE-MPE-EM support units (the latter also known as the PCB workshop). The author participated actively in all phases of the work with the large chambers. The presented results related to the large chambers were produced independently by the author in close collaboration with the CERN-based group. All photographs were taken by the author unless otherwise specified.

Contents

List of Figures

List of Tables

Abbreviations

ADC	Analog-to-Digital Converter
ASIC	Application Specific Integrated Circuit
ATLAS	A Toroidal LHC ApparatuS
BI, M, O	Barrel Inner, Middle, Outer
BNC	Bayonet Neill–Concelman (connector)
CERN	European Organization for Nuclear Research
CSC	Cathode Strip Chamber
DAQ	Data Acquisition
EI, M, O	End-Cap Inner, Middle, Outer
FD	Fermi-Dirac (function)
FEC	Front-End Card
FPGA	Field-Programmable Gate Array
GEM	Gas Electron Multiplier
HDMI	High-Definition Multimedia Interface
HV	High-Voltage
LHC	Large Hadron Collider
LVDS	Low-Voltage Differential Signaling
LVL1	Level-1 (trigger)
MDT	Monitored Drift Tube
MPGD	Micro Pattern Gaseous Detector
MWPC	Multi-Wire Proportional Chamber
NIM	Nuclear Instrumentation Module
NSW	New Small Wheel(s)
PCB	Printed Circuit Board
RPC	Resistive Plate Chamber
SHV	Safe High-Voltage (connector)
SRS	Scalable Read-out System
SPS	Super Proton Synchrotron
SW	Small Wheel(s)
TGC	Thin Gap Chamber
TPC	Time Projection Chamber

Chapter 1

Introduction

This thesis concerns the MicroMegas detector technology – a gaseous device that is one of the many breeds of Micro-Pattern Gaseous Detectors (MPGD). This relatively new class of detectors have undergone a rapid phase of development over the last few years and are by now mature enough for the LHC environment.

The LHC accelerator complex will during the next 10 years be subject to several upgrades, which will increase both the instantaneous luminosity and the collision energy. To accommodate the new operating conditions, the ATLAS detector will undergo several refurbishments. In 2018 the innermost end-cap disks in the ATLAS Muon Spectrometer (MS), the Small Wheels (SW), will be replaced with New Small Wheels (NSW). This entails a full replacement of the current instrumentation with detectors that are better suited for the post-upgrade environment. One of the two detector technologies chosen for this purpose is MicroMegas.

Since MicroMegas is a fairly young technology, the experience with its use in high-energy physics is sparse – especially at the scale of the NSW. Therefore, to receive the consent from the ATLAS community, a set of milestones had to be fulfilled by the Muon ATLAS MicroMegas Activities (MAMMA) Collaboration[1]. The list of milestones concerned

- Demonstrating that a single-plane spatial resolution < 100 μm is obtainable for inclined tracks
- Demonstrating that detectors with dimensions similar to those needed for the NSW could be built with the required mechanical precision
- Demonstrating that sparks do not create long-term damage to the detectors

[1]The MAMMA Collaboration is a working group within ATLAS dedicated to the development of large-area MicroMegas detectors in the context of the NSW. The list of participating institutes includes Arizona, Athens, Brookhaven, CERN, JINR Dubna, LMU Munich, Naples, CEA Saclay and Thessaloniki among others.

- Demonstrating that detector operation in a magnetic field can provide the required spatial resolution

This thesis describes a selection of the work conducted by the CERN-based ATLAS MicroMegas group in the latter half of 2012 and the first half of 2013 to fulfil the first two points in the list. The focal point for our efforts were the ATLAS-contextualized milestones, but also included basic R&D activities. Our progress was hence often shared with the RD51 Collaboration, which is dedicated to the development of MPGDs. The MAMMA Collaboration succeeded in the fulfilment of all milestones and the MicroMegas technology will thus be implemented in the ATLAS Muon Spectrometer during the shutdown in 2018. The summary of the ambitious NSW project is found in the technical design report [4].

We initiate the thesis with appropriate background theory. In Chapter 2 we review the interactions of charged particles with matter and the physical principles governing the behaviour of the proportional counter. This knowledge will prove itself necessary for performing laboratory work and interpreting results. Hereafter, in Chapter 3, we describe the MicroMegas technology. Chapter 4 covers the ATLAS detector, its Muon Spectrometer and motivates its scheduled upgrade.

Our experimental work is segmented into five chapters. In Chapter 5 we describe the test-beam campaign among with the experimental equipment used. This is useful since later chapters will be based on either the data recorded at this occasion or utilize the experimental setup from the campaign.

Chapter 6 contains a study of the spatial resolution. We here demonstrate the so-called μTPC technique where the MicroMegas is exploited as a Time Projection Chamber (TPC). Afterwards we compare it to and combine it with the traditional charge centroid method. By doing so we demonstrate that a single plane spatial resolution nearly independent of the inclination of the incoming track can be obtained and that the yield is less than or very close to the desired 100 μm. This study is performed to fulfil the first point in the list of milestones.

In Chapter 7 we review the construction of the first large-area detector, L1, and compare its functionality to the well-known T chambers. Chapter 8 describes the design, construction and assessment of the full-sized prototype, L2. Both chambers were constructed within the scope of the milestones. New construction schemes had to be developed and customized for this endeavour, among this the floating mesh technique, which is an alternative to bulk construction. Our large-scale detectors were, and still are, state of the art.

Chapter 9 concludes the thesis.

Part I

Theory

Chapter 2

Detection with Proportional Counters

The detector technology of interest for this thesis belongs to the category of proportional counters – a broad class of gaseous ionization detectors that have found great use in modern high-energy physics experiments. In this section we set up the theoretical framework that governs the underlying physical principles of the proportional counter. This theory will provide the basis for understanding the characteristics of our particular detector type, among with the assessment of its functionality and performance. In this context we find it useful to review the relevant theory concerning energy deposition by charged particles. The MicroMegas technology will be reviewed in Chapter 3.

2.1 Nomenclature and definitions

The particle velocity measured with respect to the speed of light is $\beta = v/c$ and the Lorentz factor is defined as $\gamma = 1/\sqrt{1-\beta^2}$ [1]. The total particle energy is given by $E^2 = p^2c^2 + m^2c^4$ [17]. The product $\beta\gamma$ is equal to $\beta\gamma = p/Mc$ such that $p = \beta\gamma Mc$. If using the natural units $\hbar = c = 1$, the mass, energy and momentum of the particle will be measured in energy, here in units of electronvolt [17]. A particle is considered relativistic if its energy is much greater than its rest-mass, i.e. $E \gg M$. Definitions of the parameters used throughout this section are summarized in Table 2.1.

2.2 Charged particle interactions in matter

We will throughout this thesis mostly conduct studies with minimum ionizing particles, a concept applying to charged particles propagating at a velocity where the average energy loss is at a minimum. To grasp this we briefly review the basic theory behind

TABLE 2.1: Summary of parameters used in this section [1, 15].

Symbol	Definition	Units/Value
r_e	Classical electron radius	2.8179403 fm
$m_e c^2$	Electron mass $\times$ c^2	0.5109989 MeV
N_a	Avogadro's number	$6.0221415 \times 10^{-23}$ mol^{-1}
K	$4\pi N_A r_e^2 m_e c^2$	
I	Mean excitation potential	Z dependent, see [15]
Z	Atomic number of absorber	
A	Atomic mass of absorber	g mol^{-1}
ρ	Density of absorber	g cm^{-3}
z	Charge of incident particle in units of e	z 1.6×10^{-19} C
$\delta(\beta\gamma)$	Density correction	Z dependent, see [15]
C	Shell correction	Z dependent, see [15]
Q_{max}	Max. energy transfer in single collision	
X_0	Radiation length	g cm^{-2}
M	Mass of incident particle	MeV/c^2
E	Energy of incident particle	MeV
β	v/c of incident particle	
γ	Lorentz factor, $1/\sqrt{1-\beta^2}$	
b	Interaction cross-section	$b = 1 \times 10^{-28}$ m^{-2}

the interactions of charged particles with matter. This will include descriptions of the average energy loss experienced by the propagating particle, the fluctuations in its energy loss and the ionization mechanisms that cause these. A profound understanding of these concepts will be highly useful when conducting experimental work with gaseous devices.

2.2.1 Energy loss

The mean stopping power for a high-energy muon (or another charged particle with mass $M \gg m_e$) with energy E in a material can be described by [18]

$$-\left\langle \frac{dE}{dx} \right\rangle = a(E) + b(E)E \tag{2.1}$$

The term $a(E)$ is the electronic stopping power, which represents the energy deposition through random, individual collisions where the particle looses a random amount of energy, which will cause either ionization or excitation of the atoms in the medium. The term $b(E)$ is due to radiative processes: bremsstrahlung, pair production and photo-nuclear interactions [18]

$$b \equiv b_{\text{brems}} + b_{\text{pair}} + b_{\text{nucl}} \tag{2.2}$$

The notation in Equation 2.1 is convenient since $a(E)$ and $b(E)$ are slowly varying functions of the energy at the energy scales where radiative corrections are important.

The energy level where the electronic stopping power and radiative effects for electrons contribute with an equal amount is known as the critical energy. For $E < 100$ GeV, $b(E)E$ is less than 1% of $a(E)$ for muons in most materials [18] and will therefore not be considered further.

The description of the stopping power due to interactions with atomic electrons is summarized in the Bethe-Bloch equation given by [15, 18]

$$-\left\langle \frac{dE}{dx} \right\rangle = Kz^2 \frac{Z}{A} \frac{1}{\beta^2} \left[\frac{1}{2} \ln \left(\frac{2m_e c^2 \beta^2 \gamma^2 Q_{max}}{I^2} \right) - \beta^2 - \frac{\delta(\beta\gamma)}{2} - \frac{C}{Z} \right] \tag{2.3}$$

This expression holds for intermediate-Z materials in the range $0.1 \lesssim \beta\gamma \lesssim 1000$ [1]. With the symbol definitions and values given in Table 2.1 the units are MeV g^{-1} cm^2. The maximum energy transfer, Q_{max}, occurs in a head-on collision and can from kinematic theory be shown to yield [1, 15]

$$Q_{max} = \frac{2m_e c^2 \beta^2 \gamma^2}{1 + 2\gamma m_e/M + (m_e/M)^2} \tag{2.4}$$

The total stopping power of a muon in copper as a function of its momentum is shown in Figure 2.1.

Equation (2.3) contains the so-called close collision and distant collision terms. These names originate from a classical calculation where an impact parameter at the order of the size of the atom was used to distinguish the two. The terms are still in use although a quantum-mechanical treatment has replaced the classic estimate, classifying the collisions in terms of momentum transfer [19].

Some noteworthy features of Equation (2.3) are the close collision dependence on Z of the material and the proportionality to the square of the particle charge z. Another notable property is the $\ln(\beta\gamma)$ behaviour of the distant collision term. This logarithmic rise happens as a result of the Lorentz contraction, which causes the electric field of the particle to flatten and extend as the energy increases [15]. Only a minor dependence on M is present at the highest energies, introduced through the definition of Q_{max}. For all practical purposes, the stopping power in a given material is a function of the velocity of the incoming particle alone. This dependence becomes obvious from the curve in Figure 2.1.

At non-relativistic energies, the energy loss is dominated by the overall $1/\beta^2$ factor and it decreases with increasing velocity until it reaches a plateau. This implies that as a particle slows down and begins to stop it starts to lose energy very rapidly, and it will preferentially deposit more energy per unit path length when it is going slowly [20]. Fundamentally this behaviour reflects the length of time that the particle is near the scattering center; for a constant force, the momentum transfer from the projectile to the electron cloud of the atom is proportional to the length of time the particle spends near

the atom. In this way the $1/\beta^2$ behaviour of the energy loss at non-relativistic velocities reflects the loss of kinetic energy $\Delta p^2/2m$.

Throughout this thesis we will conduct studies with relativistic particles carrying velocities in the specific range where the mean energy loss is at a minimum. Particles in this range are commonly referred to as minimum ionizing particles, or MIPs. This region is instantiated at $\beta\gamma \approx 3$ [1], which for muons with a mass of $M_\mu \approx 100$ MeV corresponds to $p \approx 0.3$ GeV.

As the energy increases beyond the minimum ionizing regime, the $1/\beta^2$ term becomes almost constant and the energy loss starts to rise again because of the logarithmic dependence, which can be understood from the relativistic transformation of the projectile electric field [15]. This rise is however constricted by the density effect correction, which also is included in Equation (2.3). The density effect arises because the medium becomes polarized as the particle propagates. Because of this, the extension of the electric field is limited, and the logarithmic rise in the distant collision term is truncated. Since the induced polarization will be greater in condensed materials than in lighter substances such as gases, the magnitude of the density effect depends on the medium [15]. The correction for the density effect is given by the $\delta(\beta\gamma)/2$ term. Details on the density effect and analytic expressions for the values of δ for various values of Z can be found elsewhere [15, 16, 21].

Equation (2.3) also contains the shell correction, which accounts for the binding energy of the atomic electrons. This does in particular play an important role as the velocity of the particle approaches the orbital velocity of the atomic electrons. At such energies the assumption that the electron is stationary with respect to the incident particle is no longer valid. The shell correction is generally small, at the few percent level [1, 15].

The Bethe-Bloch formula with the density and shell corrections is sufficiently accurate for elementary particles [15]. Its validity and accuracy can however be extended by including a number of corrections pertaining to, among others, bremsstrahlung from both the atomic electrons and the incident particle, a correction accounting for opposite charges, higher-order terms in the scattering cross-section etc. [15].

For everyday calculations the Bethe-Bloch equation in its full form is rarely used. When considering MIPs calculations can be simplified drastically. By assuming a constant stopping power, the quoted value for typical energy losses of a MIP, here denoted $\langle dE/dx \rangle_{MIP}$, is 1.5 MeV g^{-1} cm^2 [20]. Exact values for different absorbers can be found in appropriate tables [20]. By knowing this value among the density and thickness of the absorber, the energy loss can be calculated very simply. For example, given that the density of iron is $\rho_{Fe} = 7.87$ g cm^{-3} [20], a cosmic (minimum ionizing) muon will in 100 cm of iron deposit the energy $\langle dE/dx \rangle_{MIP} \times \rho_{Fe} \times \Delta x \approx 1.2$ GeV. A frequently

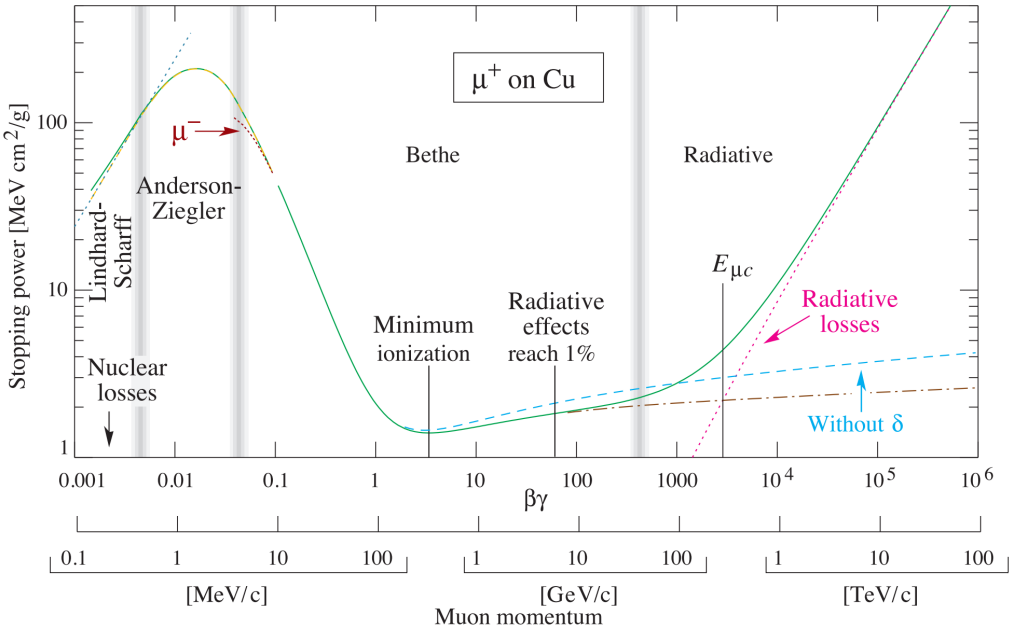

FIGURE 2.1: The stopping power for positive muons in copper as a function of p and $\beta\gamma$ over nine orders of magnitude in momentum. Solid curves indicate the total stopping power. The vertical bands indicate boundaries between different theoretical approximations of dominant physical processes [1].

encountered situation throughout this thesis will be a minimum ionizing muon traversing 5 mm of argon gas. Given that argon in gas-form at room temperature possess the density $\rho_{Ar} \approx 1.7 \times 10^{-3}$ g cm^{-3} [22], a relativistic muon will deposit ≈ 1.3 keV.

2.2.2 Energy loss fluctuations in thin absorbers

The energy loss is a statistical process and will therefore fluctuate from event to event, even for particles with the same energy. The Bethe-Bloch equation provides the average energy loss of the traversing particle, but does not describe its fluctuation. The theory regarding energy loss fluctuation, or energy straggling, has found extensive applications in experimental high-energy physics, in particular in the task of particle identification. As will be demonstrated throughout this thesis, knowledge of this subject becomes useful in the context of verifying detector performance.

We will exclusively treat the case of energy loss fluctuations in thin absorbers, which is a rather non-trivial topic compared to thick absorbers. The parameter often used to distinguish the two is the ratio [15]

$$\kappa = \bar{\Delta}/Q_{max} \tag{2.5}$$

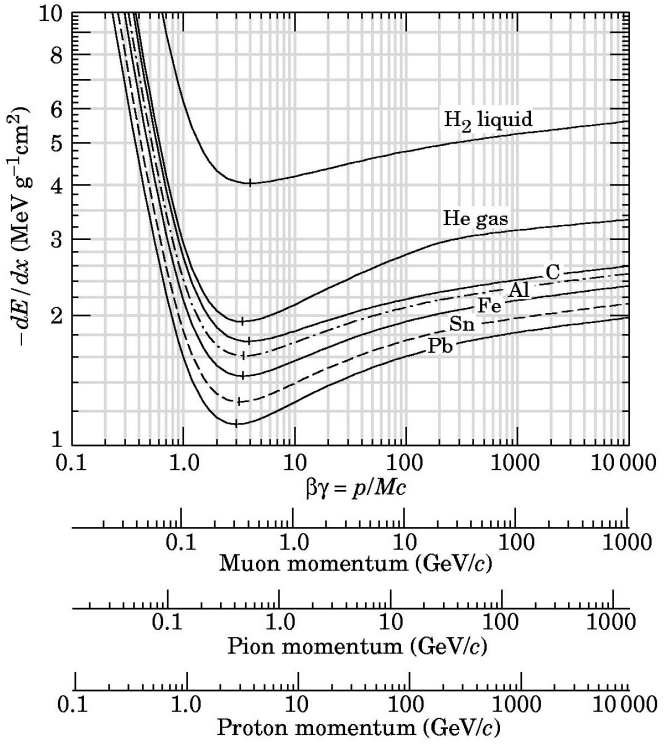

FIGURE 2.2: Mean energy loss rate in liquid hydrogen, gaseous helium, carbon, aluminum, iron, tin and lead for muons, pions and protons [1].

the fraction between the mean energy loss, $\bar{\Delta}$, and the maximum energy transfer permitted in a single collision (defined in Equation (2.4)). The mean energy loss is typically approximated with the first multiplicative term from the Bethe-Bloch equation [23]. Assumptions about the absorber thickness can be made with κ; for example, Landau's theory was developed for thin absorbers with $\kappa \ll 1$ [19].

The first calculations on energy loss fluctuations were introduced by Landau, and straggling functions do in the high-energy community therefore often go under the name Landau functions. We will in the following make the convention that the term Landau function (or distribution) refers to his specific calculations, meanwhile energy loss distributions calculated by other means will be referred to as straggling functions.

The probability distribution function $f(\Delta; x, \beta\gamma)$ for the energy loss Δ in an absorber with thickness x is uniquely determined by the collision cross-section differential in energy loss and the electron density in the layer [23]. There are no simple analytic functions representing straggling functions, but two approaches are commonly used in the derivation of these: a convolution method and the Laplace transform method, the latter introduced by Landau in his original calculations. The following review is an extract from the detailed work by Bichsel [2, 24–26], who calculates straggling functions with the convolution method; a technique that we find both intuitive and instructive.

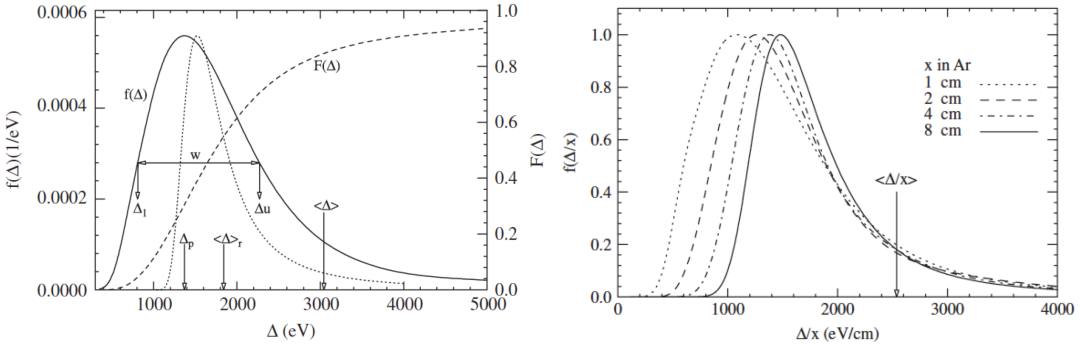

FIGURE 2.3: Left: The straggling function $f(\Delta)$ for particles with $\beta\gamma = 3.6$ traversing 1.2 cm of Ar is given by the solid line. The dotted line is Landau's function. The dashed line is the cumulative straggling function $F(\Delta)$ [2]. Right: Straggling functions $f(\Delta/x)$ for $\beta\gamma = 3.6$ particles traversing segments $x = 1, 2, 4, 8$ cm in Ar [2]. A noticeable feature is the discrepancy between the most probable and the mean value of the distributions.

At first $\sigma(E;\beta\gamma)$ is defined as the collision cross-section differential in energy loss, which is the probability of the energy loss E in one single collision. The accuracy of the straggling function calculation is highly dependent on how realistic this quantity is. Landau performed his calculations by approximating it with the Rutherford cross-section [2], the collision cross-section for two free charged particles. This model is applicable at energies far above the atomic binding energies where the atomic structure can be ignored. For lower energies the binding energy of the electrons must be accounted for.

Another model that succesfully has been implemented in the straggling function calculations is the Bethe-Fano (B-F) cross-section. Here the electronic interaction is treated with the Born approximation for inelastic scattering on free atoms. This method is found to yield a collision cross-section very true to real life, but the B-F calculations are not available for gases [2].

A third model, the Fermi virtual photon (FVP) method (or photo-absorption ionization) describes the electronic interactions as the emission of a virtual photon by the fast particle that gets absorbed by the material [2]. This cross-section will thus be closely related to that of the photo-electric absorption. Calculations with the FVP method are available for both gases and solids. We will not treat these three models in detail, but instead refer to [2, 16, 23], in which a rigorous review of the models and their applicability can be found.

As the particle propagates it will undergo multiple collisions with the absorber and as a result experience the total energy loss Δ. The spectra for the particular energy loss Δ occurring as a result of exactly n collisions, $\sigma(\Delta)^{*n}$, can be calculated by iterating the n-fold convolution of the single collision spectrum [2]

$$\sigma(\Delta)^{*n} = \int_0^{\Delta} \sigma(E) \cdot \sigma^{*(n-1)}(\Delta - E)dE \tag{2.6}$$

where [2]

$$\sigma(\Delta)^{*0} = \delta(\Delta) \text{ and } \sigma(\Delta)^{*1} = \sigma(E) \tag{2.7}$$

The $\beta\gamma$ dependence is implicit.

Since the number of collisions in the absorber is random in nature, the distribution is governed by the Poisson distribution, which describes the probability of n collisions in the segment x with the relation [2]

$$P(n) = \frac{m_c^n}{n!} e^{-m_c} \tag{2.8}$$

Here $P(n)$ gives the fraction of particles suffering n collisions, and m_c is the average number of collisions experienced by the incoming particles. The quantity m_c can be determined with the total collision cross-section, which is obtainable by integrating the collision cross-section differential in energy loss [2]

$$\Sigma_t(\beta\gamma) \equiv N \int \sigma(E;\beta\gamma)\mathrm{d}E \tag{2.9}$$

Given that N is the number of atoms per cm^3, Σ_t describes the number of collisions per cm. Therefore is the average number of collisions in a segment with length x equal to $m_c = x\Sigma_t$.

The straggling function $f(\Delta; x, \beta\gamma)$ can be obtained from the convolution [2]

$$f(\Delta; x, \beta\gamma) = \sum_{n=0}^{\infty} \frac{m_c^n e^{-m_c}}{n!} \sigma(\Delta)^{*n} \tag{2.10}$$

Examples of straggling functions calculated by Bichsel are seen in Figure 2.3 among with the Landau function.

We observe the characteristic asymmetric nature of the distributions, which strongly resembles the Poisson distribution. The conspicuous long tail is due to the the rare occurrences of very large energy transfers, while events with lower energy transfers, resulting in excitations and ionizations, constitute the bulk of the distributions.

The most probable value (MPV), Δ_p, the location of the peak of the distribution, corresponds to the most probable energy loss. An important point is the big discrepancy between Δ_p and the mean energy loss $\langle\Delta\rangle$, which is seen in Figure 2.3. The latter is what is represented as $\langle dE\rangle$ in the Bethe-Bloch equation. It is noteworthy that $\langle dE\rangle$ does not change much with x, whereas Δ_p does. Because of this some authors argue [2] that the concept of mean energy loss is used inappropriately in the description of the physics of most high-energy particle detectors, and that the most probable energy loss Δ_p and the width of the distribution is more representative of $f(\Delta)$ than the Bethe-Bloch mean energy loss.

2.2.3 Ionization mechanisms and yield

In this section we review the different ionization mechanisms that are relevant in the context of proportional counters. These mechanisms account for the electronic interactions, which we have referred to extensively throughout this chapter.

Primary and secondary ionization are distinguished. A primary ionization is the event where one or sometimes two or three primary electrons are ejected from the atom A as a result of being encountered by the incoming particle. In the case of an incoming μ this process would look like [16]

$$\mu A \longrightarrow \mu A^{+} e^{-},\ \mu A^{++} e^{-} e^{-}, ... \tag{2.11}$$

A secondary ionization denotes the process where the primary electrons are energetic enough to cause further ionization. These electrons are known as δ-rays and they may ionize through processes like [16]

$$e^{-} A \rightarrow e^{-} A^{+} e^{-}, e^{-} A^{++} e^{-} e^{-} \tag{2.12}$$

The occurrences of δ-rays are rare and correspond to the high tail in the straggling function.

Ionization might also occur through intermediate excited states A^{*}. An example of such an interaction is the following reaction chain involving the collision of the excited state with a second species, B, of atoms or molecules that is present in the gas [16]

$$\mu A \rightarrow \mu A^{*} \tag{2.13}$$

or

$$e^{-} A \rightarrow e^{-} A^{*} \tag{2.14}$$

which cause ionization like

$$A^{*} B \rightarrow A B^{+} e^{-} \tag{2.15}$$

The latter reaction occurs if the excitation energy of A^{*} is above the ionization potential of B. In most gaseous detectors A^{*} is often the metastable state of a noble gas created in the reaction 2.14, and B is one of the molecular additives known as quenchers, which is required for the stability of operation in the proportional mode. More details on quenchers are given in Section 2.3.7.

Ionization energies for most gases used for radiation detection ranges between 10 and 25 eV [16]. However, since excitations of the detecting medium frequently happens, the average energy spent by the incident particle on one ionization, W, is higher than the actual ionization energy. Theoretically W depends on the gas-mixture and the type

TABLE 2.2: Energy W spent, on average, for the creation of one ionization electron in various gases. W_α and W_β are from measurements using either α or β sources, respectively. I is the energy theoretically needed to ionize [16].

Gas	W_α[eV]	W_β[eV]	I[eV]
H_2	36.4	36.3	15.43
He	46.0	42.3	24.58
Ne	36.6	36.4	21.56
Ar	26.4	26.3	15.76
Kr	24.0	24.05	14.00
Xe	21.7	21.9	12.13
CO_2	34.3	32.8	13.81
CH_4	29.1	27.1	12.99
C_2H_6	26.6	24.4	11.65
Air	35.0	33.8	12.15
H_2O	30.5	29.9	12.60

and energy of the incident radiation. Empirical studies however show that the value is remarkably constant for many gas and radiation types. An overview of the ionization energies for different gases, both predicted and measured, is shown in Table 2.2 [16]. The fluctuation in the average number of ions pair created is the Fano factor, which is an empirically determined constant.

2.3 Working principle of proportional counters

Gaseous devices can be operated in different modes that are specified by the magnitude of the applied electric field. This dependence is visualized in Figure 2.4. The term proportional counter refers to a class of ionization detectors that are operated in the regime where the amount of charge liberated by the incident particle and the multiplied amount of charge are proportional. The traditional wire-based proportional counters were introduced in the late 1940s. The continuous development culminated in 1968 in the pioneering invention of the Multi-Wire Proportional Counter (MWPC), for which Charpak was awarded the Nobel Prize in 1992 [27]. Since proportional counters mostly are gas-based and therefore relatively cheap, they are particularly feasible for large-area usage. Numerous present-day detector technologies used in modern high-energy physics experiments are proportional counters and they come in a broad variety of geometries and performance characteristics that can be customized to the given application.

Proportional counters rely on a series of physical effects that combined enable particle detection. They are ionization detectors meaning that the detecting mechanism is the creation of electron-ion pairs, as described in Section 2.2.3. An external electric field is applied to the electrodes of the counter to make the liberated charges drift, see Section

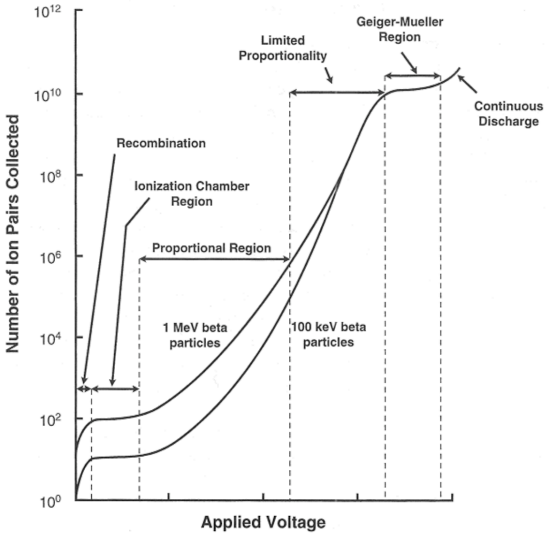

FIGURE 2.4: Modes of operation for a gaseous device [3].

2.3.2. The unique physical feature of this detector type is the Townsend avalanche described in Section 2.3.3, which is a mechanism resulting in the amplification of the number of primary electrons. The movement of the charges liberated in the avalanche, both electrons and ions, induces an electrical current in the electrodes, which is the signal that is measured by the chosen read-out electronics. This latter process is described in Section 2.3.4.

2.3.1 Relating the ionization yield to energy loss

We continue our discussion from Section 2.2.3. The actual energy loss in an absorber is not directly measurable, however, it can be measured indirectly by assuming that it is directly related to the ionization yield. The number of liberated electrons in the absorber n_i is connected to the energy deposition Δ by the relation

$$\Delta = n_i W \tag{2.16}$$

where it is assumed that W (defined in Section 2.2.3) is independent of Δ[1]. Some deposited energy will escape detection in the form of δ-rays or ultraviolet photons. This amount is however assumed to be negligible, since it corresponds to rare occurrences of large energy transfers.

To calibrate the absolute ionization distribution to energy loss, the response to a known energy deposition must be measured. This is for example done with portable

[1]For the energy deposition of Equation 2.16, we assume linearity between the energy deposition and the ionization yield, both at the level of individual energy transfers and for the combined energy loss Δ. Concerns about these assumptions are treated in [23].

radioactive sources. The relation between the ionization yield and the energy loss allows proportional counters to provide an energy loss measurement. All data presented throughout this thesis will be shown relative to other data.

2.3.2 Transport of charges in gases

In the absence of an external field the liberated electrons and ions will diffuse uniformly from their point of creation. At thermal equilibrium their mean speed will be given by the Maxwell distribution [15]

$$v = \sqrt{\frac{8k_BT}{\pi M}} \tag{2.17}$$

with T being the temperature, k_B Boltzmann's constant and M the mass of the charge.

Because of the random nature of the collisions between the charges and the atoms of the medium, the distribution of the charges around the point of creation after a fixed time t can be shown to be Gaussian. The spherical spread in radius will be given by [15]

$$\sigma(r) = \sqrt{6Dt} \tag{2.18}$$

where D is the diffusion constant [15]

$$D = \frac{1}{3}v\lambda \tag{2.19}$$

The mean free path of the charge in the gas is given by [15]

$$\lambda = \frac{1}{\sqrt{2}}\frac{k_BT}{p\Sigma_t} \tag{2.20}$$

where p is the pressure and Σ_t was defined in Section 2.2.2. The inverse dependence on the mean free path on the pressure and total collision cross-section is intuitively meaningful. When solving for D the following expression is obtained

$$D = \frac{2}{3\sqrt{\pi}}\frac{1}{p\Sigma_t}\sqrt{\frac{(k_BT)^3}{M}} \tag{2.21}$$

The dependence of the diffusion on the various gas parameters now become evident. In practice, the parameters that are most easily controlled are the pressure and temperature.

By applying an external electric field the liberated electrons and ions will accelerate towards the anode and cathode, respectively. This acceleration is interrupted by collisions with the gas molecules, which sets an upper limit on the maximum velocity that can be obtained. In kinetic theory the drift velocity of electrons can be assumed to be

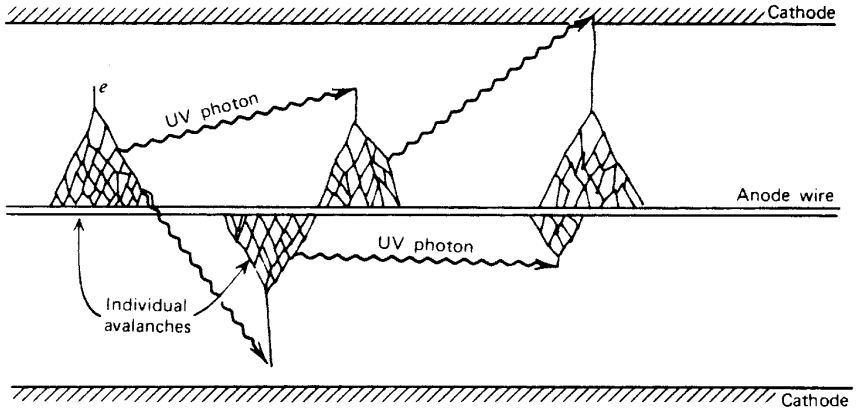

FIGURE 2.5: A schematic of a wire tube. The grids represent individual electron avalanches. UV photons originating from the original avalanche trigger the formation of additional avalanches – a so-called Geiger-Muller discharge. This situation is avoided in proportional counters by adding a quenching gas that absorbs the stray photons [3].

proportional to their acceleration between collisions and therefore expressed as [28]

$$v_{drift} = \mu E \tag{2.22}$$

where μ is the mobility and E the electric field strength. The electron drift velocity is typically several order of magnitudes larger than the drift velocity of the ions [16]. The mobility of ions does not depend much on the field strength, but varies inversely proportional to the pressure, i.e. $\mu \cdot p \approx$ constant [16]. The different behaviour of the ions is because of their much larger mass. In the following sections it will be seen how the slow drift of ions has a rather large impact on the performance and operation of proportional counters.

2.3.3 The Townsend avalanche

The Townsend avalanche is a type of breakdown mechanism [29]. If the applied electric field is sufficiently strong, the primary electrons will gain adequate kinetic energy to ionize further. The newly liberated electrons will be accelerated in a similar way and obtain the ability to ionize as well. The net result is a cascade of electrons that develops towards the anode with the electrons forming the front of the avalanche. This physical effect is exploited in proportional counters.

The number of electrons created by the avalanche over a distance from x_{min} to x_{max} is given by [30]

$$n(x) = n(x_{min}) \exp\left[\int_{x_{min}}^{x_{max}} \alpha[E(x')]dx'\right] \tag{2.23}$$

where $n(x_{min})$ is the initial number of electrons. The parameter α is known as the first Townsend coefficient and represents the number of ion pairs per unit path length created by a single electron. No fundamental expression exists for α and the various analytical expressions appearing in the literature differ [31]. However, the expression postulated by Diethorn is frequently used. It is natural to assume that α is proportional to the kinetic energy obtained by an electron over a mean free path. This is proportional to the acceleration and indeed Diethorn found empirically that α is proportional to E [16]

$$\alpha[E(x')] = \beta E(x') \tag{2.24}$$

In this formulation β is a parameter related to the average energy $e\Delta V$ required to produce one more electron in the avalanche [16]. More details can be found in [16]. Diethorn's assumption will play a central role in detector operation and performance assessment throughout this thesis.

Another important parameter in the context of proportional counters is the gain, which is the multiplicative factor of the avalanche defined as [30]

$$G = \frac{n_e(x)}{n_e(0)} = \exp\left[\int_{x_{min}}^{x_{max}} \alpha[E(x')]dx'\right] \tag{2.25}$$

That is, G is the fraction between the total number of electrons created after the avalanche has developed and the number of incoming electrons. Using Equation (2.24) we see that the gain is expected to grow exponentially with the applied voltage. This fact will be used frequently throughout the thesis to verify the functionality of our detectors.

The propagation of the Townsend avalanche gives rise to a current in the detector. Since the duration of an avalanche is around one ns and the gain typically approaches 10^4, the detector current caused by, say 10 primary electrons is $e \times 10^5/1$ ns $= 16$ μA. The detector current can easily be monitored in the laboratory from the power supply and thus provides a quick way to evaluate the operational condition of the detector. The occurrence of a single avalanche is difficult to register because of its short duration, but a steady flux of incoming radiation at a sufficiently high rate will cause a continuous and measurable current.

2.3.4 Formation of the signal

The movement of the electron-ion pairs created during the avalanche induces an electronic signal in the electrodes. We will not treat this subject in great details, but simply extract a few essential points from [16].

The current induced on a grounded electrode by a point charge q moving along a

trajectory $x(t)$ is given by Ramo's theorem, yielding [16]

$$I_n^{ind}(t) = -\frac{dQ_n(t)}{dt} = -\frac{q}{V_n} E_n[x(t)]v(t) \tag{2.26}$$

where $I_n^{ind}(t)$ is the current induced in electrode n, $dQ_n(t)$ is the charge induced in electrode n in a small time interval, and $v(t)$ is the particle velocity. The parameter $E_n[x(t)]$ is the electric field when the charge q is removed, electrode n is set to voltage V_n and all other electrodes are grounded. The current will be defined by the sign of the charge but also by the orientation of the particle velocity with respect to the electric field.

The total amount of charge, Q_n^{ind}, that flows between electrode n and ground when the charge q moves along the trajectory $x(t)$ from the position $x_0 = x(t_0)$ to $x_1 = x(t_1)$ can from Equation (2.26) be proven to be given by [16]

$$Q_n^{ind} = \int_{t_0}^{t_1} I_n^{ind}(t)dt = \frac{q}{V_n} \left[\psi_n(x_1) - \psi_n(x_0)\right] \tag{2.27}$$

where $\psi_n(x_0)$ and $\psi_n(x_1)$ are the potentials at the two points. From Equation (2.27) we see that the induced charge only depends on the end points and not on the specific path traveled. Here we encounter an important physical fact: if the charges q and $-q$ are liberated in an ionization event, and q moves to the surface of electrode n while $-q$ moves to the surface on some other electrode, the total induced charge in electrode n will be q, since $\psi_n = V_n$ on electrode n and $\psi_n = 0$ on the other electrodes. This fact enables the measurement of deposited energy as described in Section 2.3.1, and allows for techniques like the charge centroid method, which will be elaborated in Chapter 6.

From the above equations we expect the movement of the electrons to induce a rapid current because of their high drift velocity, meanwhile the ions will induce a current with a smaller magnitude, but longer duration. An illustration of this is shown in Figure 2.6, where t_e and t_i denote the drift time of the electrons and ions, respectively. When being read out the induced signal is usually integrated and shaped, which means that the shape of the actual observed pulse is dominated by the characteristics of the read-out electronics and therefore differs from that indicated in Figure 2.6.

2.3.5 Space charge effects

The presence of ions in the gas occurring as a result of the avalanche can lead to so-called space charge effects. Two types are usually distinguished.

Since the collection time of ions is relatively long with respect to that of the electrons, non-evacuated positive ions will be present in the gas in the wake of an avalanche. If the detector is exposed to radiation with a rate that is higher than the ion collection time,

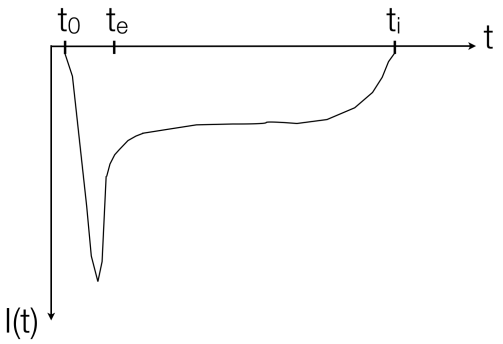

FIGURE 2.6: Illustration of the induced signal in a proportional counter. Here t_e and t_i denotes the drift time of the electrons and ions, respectively. The current induced by the movement of the electrons is expected to be short and rapid compared to that induced by the ions.

the ions build up a stationary space charge density in the detector volume. This results in a drop in the applied electric field and likewise in the gain – reliable operation is lost.

Self-induced effects arise when the gain is sufficiently high such that positive ions formed during the avalanche can alter the applied electric field and reduce the number of electrons produced in further stages of the avalanche [31]. This effect depends on the magnitude of the gain and the geometry of the counter, but does not depend on the rate of the incoming radiation [31].

As will be explained in Chapter 4, the first type of effect can be severe for the performance of a counter and it often defines the upper limit on rate capability. A rigorous treatment of the subject can be found in [16].

2.3.6 Discharge

Another type of breakdown mechanism relevant in the context of proportional counters is streamer breakdown. It is qualitatively different from the Townsend mechanism, being characterized by narrow, well-defined regions of plasma produced by single electron avalanches [30], commonly known as sparks. A spark occurs when the electron avalanche becomes so large that the electric field it produces at the avalanche front greatly enhances the amount of ionization there. Raether empirically observed that this happens when the electron multiplicity reaches approximately 10^8, which now is known as a the Raether limit.

A spark will disturb the detector operation considerably since it causes the electrode of closest approach to discharge. In certain detector technologies this introduces dead times at the order of several ms, which corresponds to the time it takes to recharge the electrode. Sparks can furthermore impose irreversible detector damage. Therefore,

since the risk of spark emergence directly depends on the detector geometry and gain, the Rather criterion heavily influences the design and operation of detectors.

2.3.7 Choise of gas

The choise of gas is mainly governed by practical considerations and is a compromise between multiple factors that determine the desired operational characteristics of the detector.

Noble gases are often chosen as the detecting medium. In pure noble gases the electron energy can only be dissipated through ionization and excitation (in contrast to poly-atomic molecules that also can dissipate energy through vibrational and rotational levels). Noble gases are easy to purify and thus cheap, they are non-toxic and are chemically inert, the latter being important for maintaining stable operation and suppressing aging of the detector.

To obtain stable operation at high gain, a small amount of quencher is added. A quencher is a poly-atomic gas such as CO_2 with rotational and vibrational levels that readily absorbs stray photons [16]. During the electron avalanche, excitation of the gas atoms occurs in parallel to the ionization. When the atoms de-excite they emit photons in the visible or ultraviolet range [15]. Under proper circumstances these photons might instantiate avalanches on their own. This phenomenon is an undesired effect because it can lead to loss of proportionality, spurious signals and can cause the avalanche to spread along the anode.

Quenchers serve a second important purpose. The positive ions will at their encounter with the cathode liberate electrons[2]. These electrons can trigger avalanches and thus cause undesired signals. If a component with a high electronegativity is added to the gas these electrons will be intercepted and thus not disturb the detection. A quencher therefore often consists of two components to absorb both the stray photons and the cathode-emitted electrons.

The dependence on the electron drift velocity varies with the type of gas used. A highly preferable situation arises if the drift velocity varies little with the field gradients, on the pressure and on temperature variations of the gas, all of which are unavoidable in practice [16]. In certain gas mixtures, such as Ar/C_4H_{10}, the drift velocity saturates at sufficiently high field strengths [16]. These mixtures are preferred for applications where a constant drift velocity is needed, such as for time projection chambers.

Numerous other concerns influence the choise of gas, including safety factors related to gas flammability, cost, etc.. An extensive summary can be found in [16].

[2]This is described by Townsend's second coefficient. A review is omitted here, but can be found in [30]

Chapter 3

The MicroMegas Technology

The photolithographic technique and other methods used by the microcircuit industry enabled the development of a new breed of detectors – Micro-Pattern Gaseous Detectors (MPGDs). These detectors are mostly wire-less and exceeded the traditional MWPC in both rate capability and in spatial resolution, and are even more economically feasible. MPGDs combine attractive features like finely segmented read-out electrodes comparable to that of solid-state devices with the large-area potential of gaseous detectors. Some of the most well known MPGD technologies are the Gas Electron Multiplier (GEM) and MicroMegas.

The MicroMegas technology, a short for 'micro mesh gaseous structure', was the brainchild of Giomataris and Charpak (et al.) who invented it at Saclay in 1995 [1, 32]. It offers good energy resolution and spatial resolution down to the micrometer level, which is comparable to that provided by solid-state detectors. Furthermore, due to the very fast ion collection it possesses the ability to maintain stable and efficient operation at very high particle fluxes compared to that achievable with wire-based devices. Its mechanical characteristics such as structural robustness and high radiation tolerance furthermore make it highly practical, and since manufacturing is based on industrial techniques, large-scale production is economically feasible.

The above features make the MicroMegas technology very attractive for high-energy physics experiments. As will be explained in Chapter 4, MicroMegas has been chosen as one of the two technologies that are to be implemented in the ATLAS Muon Spectrometer during the upgrade scheduled for the year 2018. Although the technology succesfully has been used in experiments like COMPASS, NA48 and CAST [5] there was by the Summer of 2012 still some way to go in terms of R&D before the technology had been proven suitable for the LHC environment. The specific tasks needed to demonstrate the technology for the ATLAS Collaboration are also described in Chapter 4. In this section we review the basic features of the technology and its construction.

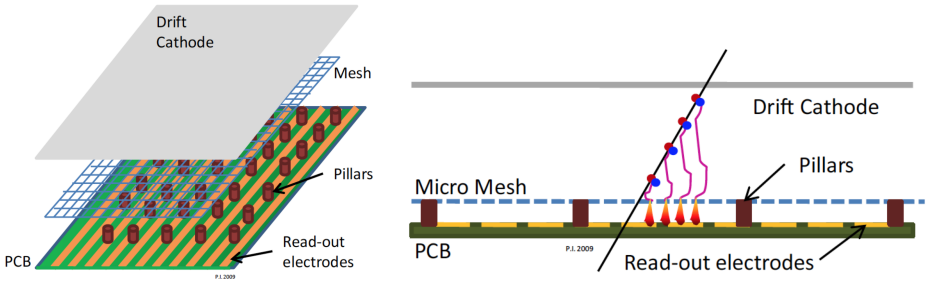

FIGURE 3.1: Left: Sketch of the baseline layout for a MicroMegas detector. The grey surface represents the drift electrode (cathode), the blue cross-hatched surface the mesh, red cylinders the pillars and the yellow/green surface the read-out plane (the resistive strip layer is not depicted here) [4]. Gas fills the drift and amplification region. Right: Depiction of the operating principle [4].

3.1 Detector layout

The layout of the MicroMegas detector is seen in Figure 3.1. It utilizes a planar geometry consisting of three parallel planes: a drift electrode, a mesh suspended on supporting pillars and a read-out plane with two layers of strips; the so-called resistive strips and the read-out strips. Note that the detector layout displayed in Figure 3.1 does not contain the resistive layer.

The region between the drift electrode and the mesh acts as a conversion and drift region, while the area between the mesh and the strips acts as the amplification region. The size of the drift region is usually a few mm, but can be chosen by the user according to the application. Correspondingly, the nominal size of the amplification region is around 128 μm depending on the type of chamber. This size is defined by the height of the pillars.

The high-voltage potentials are chosen according to the gas-mixture. For the combination of argon and CO_2 in the ratio 93/7%, which is the mixture used for all studies in this thesis, the potentials are chosen such that the applied electric field in the drift region is a few 100 V/cm and in the amplification region around 40 kV/cm. Upon the incidence of a charged particle in the drift region, the gas will be ionized. The applied electric field will cause the primary electrons to drift towards the mesh. With the electric field in the amplification region being much stronger than that in the drift region, the mesh will be transparent to more than 95% of the electrons [4]. The Townsend avalanche occurs in the amplification region immediately above the strips and has a transversal spatial extent of a few 100 μm.

The anode is segmented into resistive strips with a specified pitch and resistivity. They are placed the above the read-out strips, which they geometrically match. The

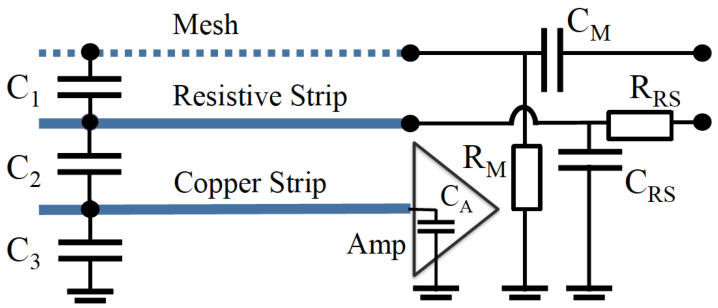

FIGURE 3.2: Equivalent electric circuit for a MicroMegas bulk. C_1, C_2 and C_3 are, respectively, the capacities from the mesh to resistive strips, from the resistive strips to read-out strips and from the read-out strips to ground. The mesh is grounded through the resistance R_M. C_M is the capacitance of the mesh to detector ground. The read-out strips are connected to ground potential through the input capacitance of the pre-amplifier. RC-filters are applied to the high-voltage lines to the resistive strips with the components R_{RS} and C_{RS}.

two strip layers are separated with < 100 μm of insulating material and are thus capacatively coupled. The signals obtained on the read-out strips have been induced by the charge from the resistive strips. The equivalent electric circuit of a MicroMegas (excluding the drift region) is seen in Figure 3.2.

The electron avalanche happens in less than one ns [4]. The ions created in the avalanche will propagate towards the mesh. Since most of the ions are produced in the last mean free path of the avalanche, they have to propagate more than 100 μm before being evacuated. This ion backflow time is at the order of 100 ns, which is considerably faster than compared to other detector technologies. The rapid evacuation of the ions is what makes the MicroMegas technology well-suited for environments with high particle fluxes.

3.2 Spark protection with resistive strips

Sparks are unavoidable and can under unfortunate circumstances cause devastating effects. Because the gain of a MicroMegas with high detection efficiency easily approaches values of 10^4, the Raether limit is reached in events producing more than 10^4 ionizations within an area comparable to the spatial extent of one avalanche. In Chapter 4 it will become apparent that high ionzation levels are present in the LHC environment. Therefore, without any protection scheme the technology would be unsuited for the LHC experiments. The concept of resistive strips was introduced to make the MicroMegas technology spark resistant [5], and it is by now implemented in all CERN-produced chambers as the default.

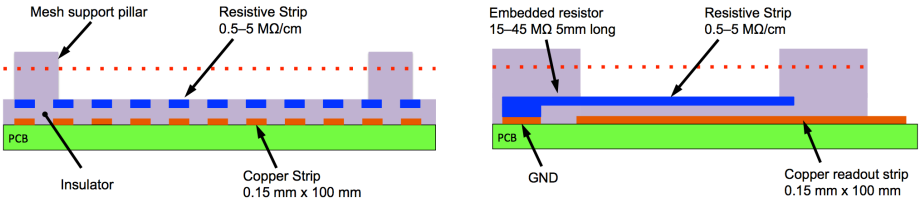

FIGURE 3.3: Sketch of the detector principle (individual parts not to scale), illustrating the resistive protection scheme. Left: view along the strips. Right: view orthogonal to strip direction [5].

A sketch of the arrangement of the strip layers is seen in Figure 3.3. The resistive strips are deposited on top of a thin insulating layer directly above the read-out electrode. The read-out electrodes will thus no longer be directly exposed to the large currents induced by a spark. By adding the resistive strips some fraction of the pulse-height is lost, which mainly depends on the thickness and dielectric properties of the insulating layer between the two strip layers. In return, the chamber can be operated with a higher gas gain [4].

The strip resistivity varies according to the application, typically in the range kΩ/□ - MΩ/□ [5]. By opting for a high resistivity the resistive strips will exert the salient feature of spark-quenching. In the event of a spark the charge Q will be transferred to the surface of a resistive strip, which will charge up in the local area around the incidence of the spark. If we attribute the capacitance C_{local} to this local region, the net voltage at this locality will be

$$V_{local} = \frac{Q}{C_{local}} \tag{3.1}$$

This means that if the local capacitance is chosen to be small, the potential difference obtained at the local point will be large. Charging up the local area with negative charges will attenuate the applied electric field, which will quench the propagation of the spark.

The time it will take to charge up the local area, τ_{local}, will be given by

$$\tau_{local} = R_{gas} C_{local} \tag{3.2}$$

where R_{gas} is the resistance in the gas during the spark, which will be minimal due to the plasma-effects occurring in the region of the discharge. From Equation 3.1 and 3.2 we see that both the speed and potency of the spark quenching depends on C_{local}, which has to be small for the effect to work. A small local capacitance is achieved by opting for a material with high resistivity[1].

The spark-quenching capabilities are shown in Figure 3.4, where sparks are shown for

[1]For details on the theory of electronics we refer to [33]

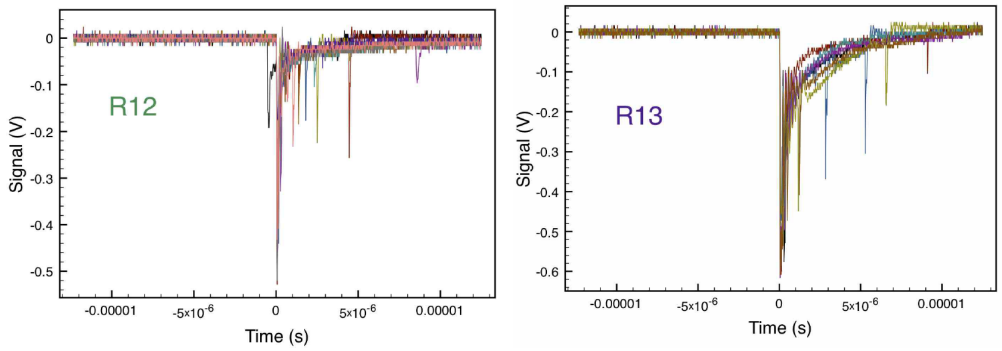

FIGURE 3.4: Typical spark signals from the read-out strips seen on an oscilloscope from the R12 and R13 MicroMegas chambers with different resistivity values on the resistive strips [5].

two MicroMegas detectors, R12 and R13, that possessed different values of resistivity [5]. The R12 chamber had an equivalent surface resistivity of 75 kΩ/□, while the corresponding value for the R13 chamber was 10 times smaller. The effect from the change in resistivity is evident: in the chamber with the highest resistivity the quenching of the spark happens around 10 times faster because of the attenuation of the applied field by the field of the local charges accumulated on the highly resistive strips.

3.3 High-voltage schemes

In the early years of MicroMegas design the bias was applied to the drift electrode and to the mesh, while the strip layers were set to ground potential. With this particular scheme the occurrence of a spark would cause the entire mesh to discharge. The time needed for the mesh to re-charge would be given by $\tau_m = R_m C_m$, with R_m being the resistance in series to the power supply and C_m the capacitance of the mesh. During τ_m the field in the amplification region would be heavily reduced and the detector would be unoperational. Depending on C_m, which is directly related to the size of the detector, τ_m could approach 10s of ms.

Instead of the above, a negative bias is applied to the drift electrode and a positive bias to the resistive strips, while the mesh is connected to ground potential. With this scheme the occurrence of a spark will only cause a few strips in its vicinity to discharge. This situation is preferred over the above since the affected area will be much smaller.

The latter high-voltage scheme is the default in our group for all newer chambers. Depending on the type of detector, around -300 V is applied to the drift electrode and 500 V to the resistive strips. A sketch of the field lines in the drift and amplification region of the MicroMegas is seen in Figure 3.5.

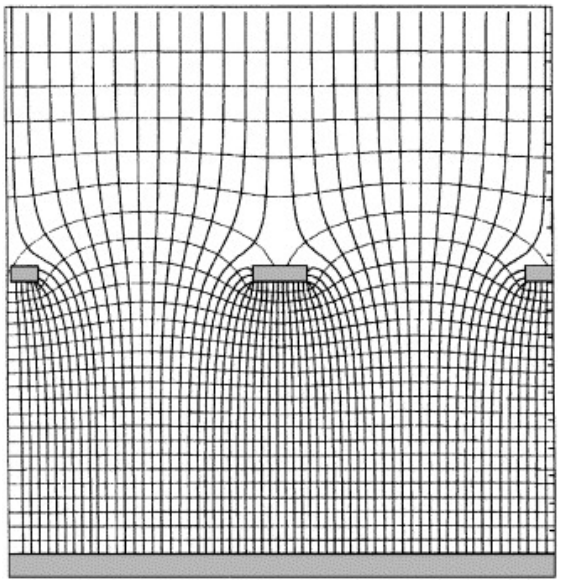

FIGURE 3.5: The electric field configuration in a MicroMegas [6]. The upper region corresponds to the drift region, the rectangles depict the mesh wires, the lower region the amplification region, and the bottom bar one resistive strip.

3.4 Fabrication process

Two types of MicroMegas detectors will be distinguished in this thesis, the so-called bulk, where the strips, pillars and mesh are produced into an un-demountable structure, and the non-bulk.

The base of each detector is a standard PCB of a material such as G10 or FR4 carrying the read-out strips. This PCB is covered with a 64 μm thick layer of photoimagible coverlay, which is hardened by UV exposure and by being cooked. A roll of coverlay in the CERN PCB workshop is shown in Figure 3.6. The resistive strips will be produced on top of this hardened layer.

One way to produce the resistive strips is to apply a copper layer onto the PCB and cut grooves into it, which will act as a mold of the resistive strips. Resistive paste, like shown in Figure 3.6, is filled into the grooves and is hardened by cooking the structure. The surplus of resistive paste is grinded away by hand, and the copper is etched away chemically. The resistive strips will with this production method obtain a very uniform shape, usually square, but the technique is rather tedious in terms of manpower.

Another way to create the resistive strips is with screen printing, which is a standard industrial process. With this technique a negative image of the resistive strips is put on a mask. The resistive paste is smeared over the mask with a machine like displayed in Figure 3.6. The paste passes through the grooves in the mask and forms the resistive strips. This method is fast and requires less manpower than the previous. However, the screen printing technique is limited by the size of the required equipment. The shape of

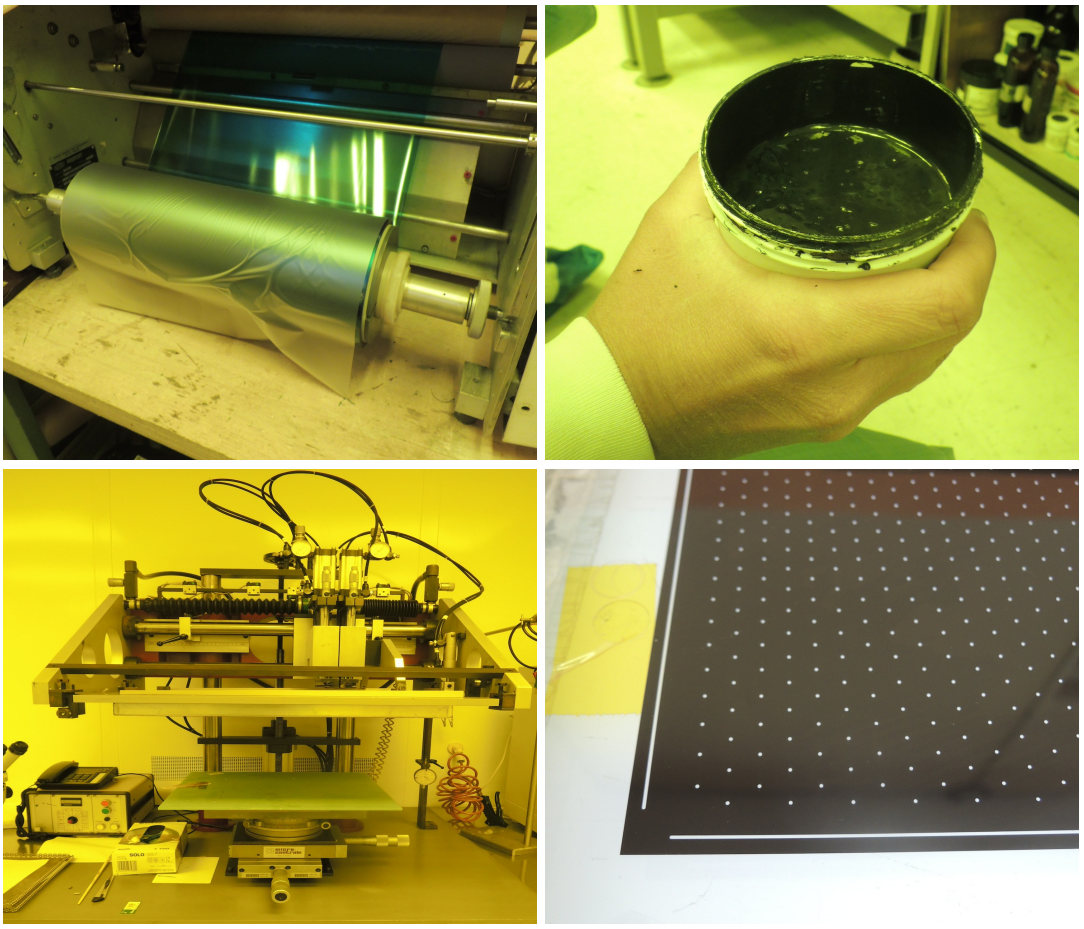

FIGURE 3.6: Top left: A roll of photoimagible coverlay mounted on a dispenser. Top right: Paste used for making the resistive strips. Bottom left: A machine used for screen printing of smaller chambers. Bottom right: A mask used for making pillars. UV light will pass through the holes in the mask and harden the exposed coverlay.

the resistive strips produced with the screen printing method will be round; this shape is advantageous since the emergence of sparks is reduced when no sharp edges are present.

The pillars are produced on top of the resistive strips with photolitography. Two layers of the 64 μm thick coverlay are applied. By exposing the coverlay to UV light through a mask like shown in Figure 3.6, the radiated areas will harden. This is enhanced by cooking it. When removing the non-hardened areas with chemical etching, the pillars are carved out. The amount of coverlay used for the pillars is what defines the size of the amplification region in a MicroMegas.

In a bulk MicroMegas the mesh and an extra sheet of coverlay is applied on top of the two sheets constituting the pillars; the mesh will hence be fastened into them during the photolithographic process. This mesh is made from a commercial sheet of woven stainless steel. Bulk chambers posses the advantage of structural robustness, but they are very vulnerable to dust caught under the immobile mesh. The CERN PCB workshop produces a series of small bulk chambers, which contain resistive strips and posses an

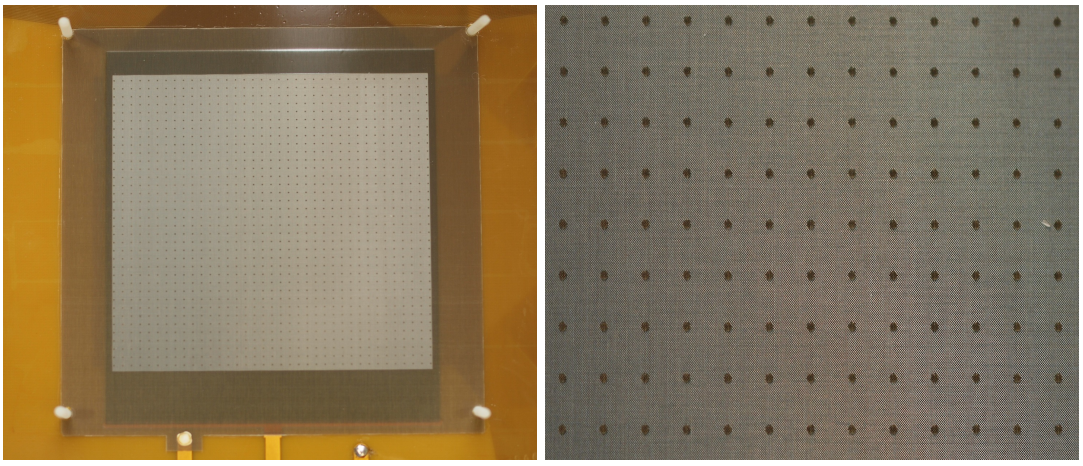

FIGURE 3.7: Left: The active area of a MicroMegas bulk with dimensions 10×10 cm^2. Right: A zoom of the active area. The dots are the pillars and the metallic surface the mesh. The pillars are arranged in a matrix with a regular distance between neighbouring pillars, usually a few mm, in x and y.

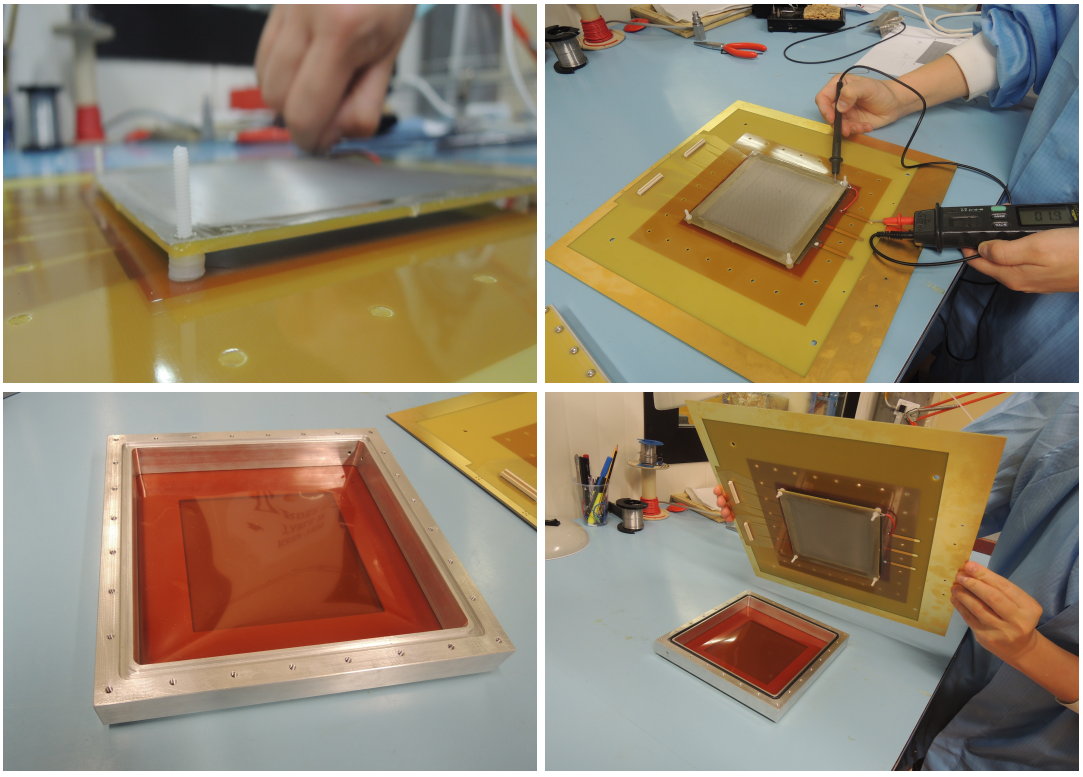

FIGURE 3.8: A bulk chamber is being assembled. All parts are cleaned with compressed air and ethanol before assembly. Top left: The drift electrode is mounted on spacers with a combined height of 5 mm. Top right: Electrical connections are checked. Bottom left: The frame to encapsulate the gas-volume. The groove is to position the gas-tightening O-ring. Bottom right: The chamber is being closed.

active area of 10×10 cm^2.

The alternative to a bulk chamber is to use a so-called floating mesh. Here the mesh

is not attached to the pillars, but instead suspended over them. Since the mesh is dismountable, the active area can be cleaned quite easily, which will prove itself highly practical when working with large-area detectors. Furthermore, with the floating mesh scheme it will be easier to delegate the construction of large-area detectors to industry – a necessity for the production of detectors for the ATLAS NSW. The implementation of a floating mesh is described in this thesis in Chapter 7 and 8.

MicroMegas detectors can be produced with multiple read-out coordinates by implementing an extra layer of read-out strips in the base PCB. The resistive strips will however only be parallel to one coordinate, which means the induced signals will spread over a larger number of strips in the second coordinate. Additionally, the charge induced in the resistive strips will be shared between all the layers of read-out strips, and the signal yield in each coordinate will as a result be lower.

The read-out strips are routed to some sort of connector, the type being specified by the user. This connector must be compatible with the intended read-out electronics. Throughout this thesis, read-out strips are routed to 130 pin Panasonic connectors; a commercial narrow-pitched board-to-board connector compatible with the SRS-based on-detector electronics (introduced in Chapter 5).

The rather straightforward assembly of a small, bulk chamber is shown in Figure 8.8. A fully assembled bulk chamber, the T7 chamber, is seen in Figure 3.9.

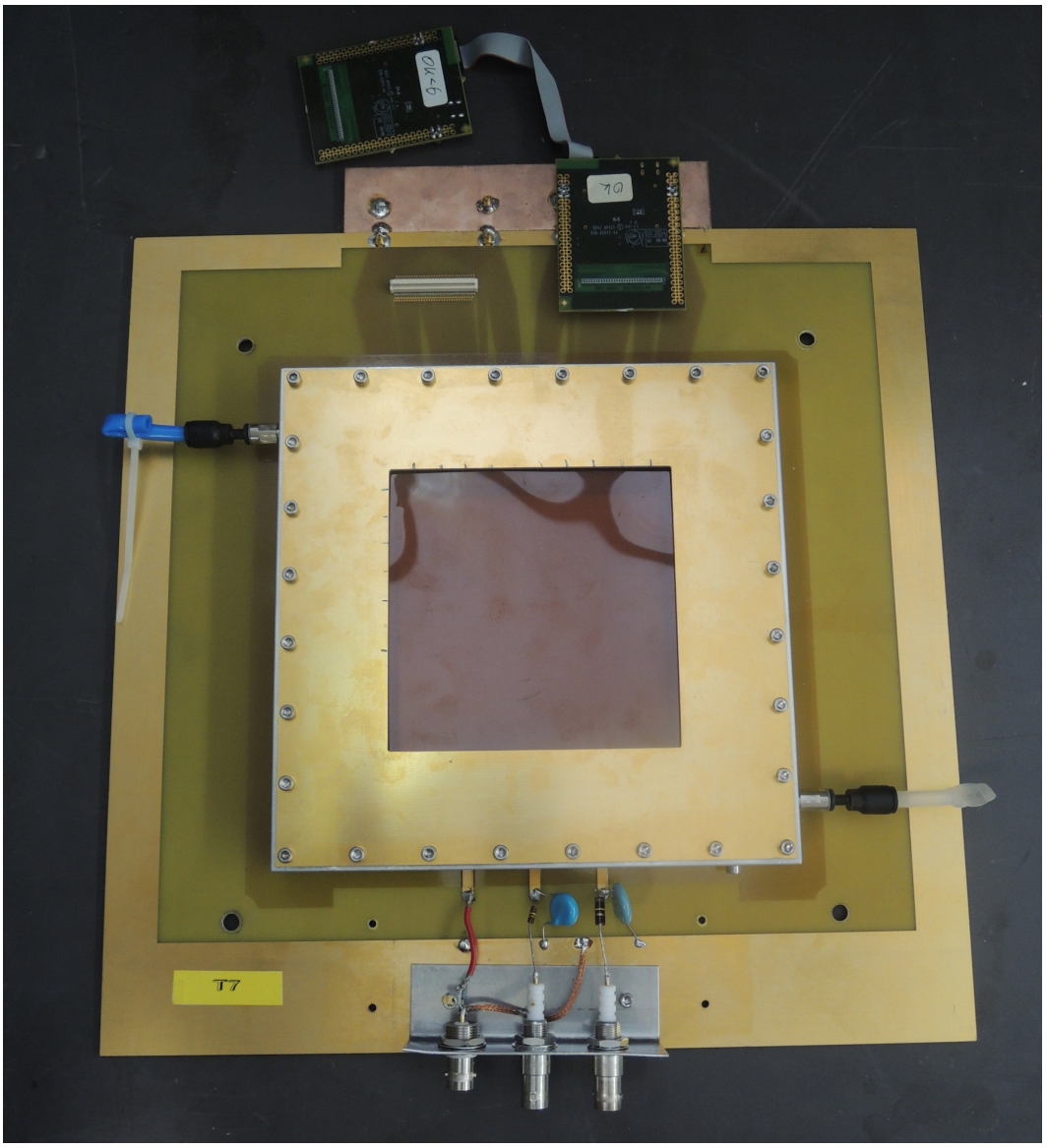

FIGURE 3.9: A fully assembled bulk chamber (the T7 chamber). The Kapton® window has the same dimensions as the active area (10×10 cm^2). The gas in- and outlet at the upper left and lower right corner are sealed. The high-voltage connections to the mesh (left connector), resistive strips (middle) and drift electrode (right) are exposed. An APV pair is mounted on the chamber.

Chapter 4

Upgrade of the ATLAS Muon Spectrometer

The Large Hadron Collider (LHC) complex will in the coming years be subject to multiple upgrades to increase both the beam energy and the instantaneous luminosity. For the experiments installed at the LHC, the increase in these parameters entails that certain parts of the experimental apparati will have to be upgraded to cope with the challenging radiation levels imposed by the new operating conditions. The ATLAS experiment is scheduled to undergo several upgrades concerning both detector systems and DAQ. Concerning the Muon Spectrometer, a rather ambitious goal was set: a complete replacement of the end-cap stations closest to the interaction point, the so-called Small Wheels (SW), during the shutdown in 2018. This is a paramount necessity for the ATLAS detector if it should continue to deliver satisfactory physics performance throughout its scheduled lifetime. One of the two detector technologies to be implemented in the New Small Wheels (NSW) is the MicroMegas technology, reviewed in Chapter 3. In this section we provide the context that legitimizes the development of the MicroMegas detectors that will be presented throughout the thesis. In order to do so, the basic principles governing the layout and instrumentation of the ATLAS Muon Spectrometer will be described among with the premises that apply to detector operation before and after the LHC upgrades.

4.1 The Large Hadron Collider

The LHC is a proton-proton collider situated at CERN, the European Organisation for Nuclear Research near Geneva, Switzerland. The LHC is installed in the underground tunnel originally constructed for the Large Electron-Positron collider (LEP), with a circumference of $\approx$ 27 km. The LHC is part of a sophisticated accelerator complex,

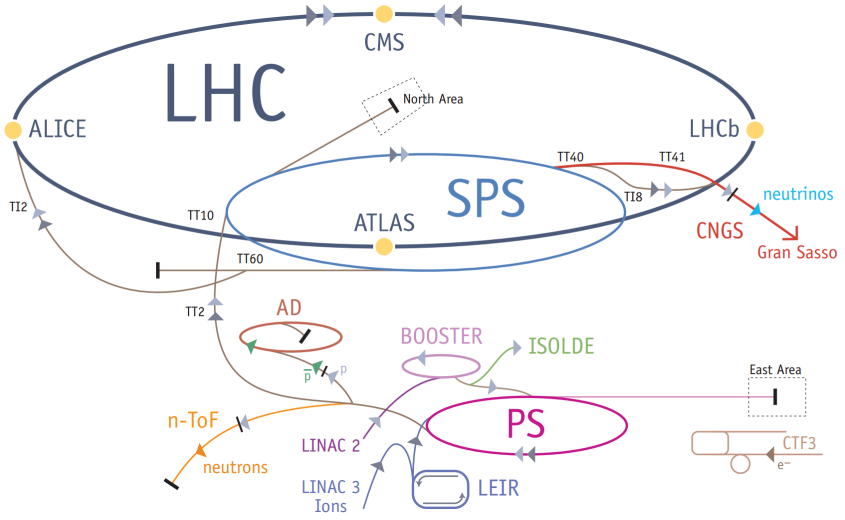

FIGURE 4.1: The accelerator complex at CERN among with its experiments [7].

which is a succession of machines with increasingly higher energies.

Immediately after the protons have been extracted from hydrogen atoms they are injected into the booster at an energy of 50 MeV. The booster accelerates them to 1.4 GeV and feeds the beam to the Proton Synchroton (PS), which accelerates it to 25 GeV. Protons are then delivered to the Super Proton Synchrotron (SPS) [7]. The SPS accelerates them to 450 GeV, which is the injection energy of the LHC. Injection into the LHC happens in both clockwise and counter-clockwise direction.

Once injected into the LHC the beams are accelerated to their nominal energy. The acceleration is provided by 8 superconducting radiofrequency (RF) cavities per beam, while the bending of the beams is provided by 1232 superconducting dipole magnets [7]. At the design luminosity each beam will consist of 2808 bunches, each containing $\approx 10^{11}$ protons, which will collide with a bunch-crossing interval of 25 ns [7].

The LHC started operation in 2008, but was subject to technical obstacles that postponed proper operation. Operation was resumed in 2010, and managed up to the end of 2011 to deliver ≈ 5 fb^{-1} at $\sqrt{s} = 7$ TeV. In 2012 the LHC started operating with $\sqrt{s} = 8$ TeV, and delivered 23.3 fb^{-1} in 2012 alone with the mean number of interaction per bunch crossing $\langle\mu\rangle$ being 20.7 [34]. The smooth operation of the LHC went beyond expectations and the data sample collected by the CMS and ATLAS experiments were sufficient to announce the discovery of a new boson the 4th of July 2012 [7, 34, 35].

4.2 The ATLAS Detector

The ATLAS (A Toroidal LHC ApparatuS) experiment, one of the four large experiments recording data from the LHC collisions, comprises an apparatus being the largest

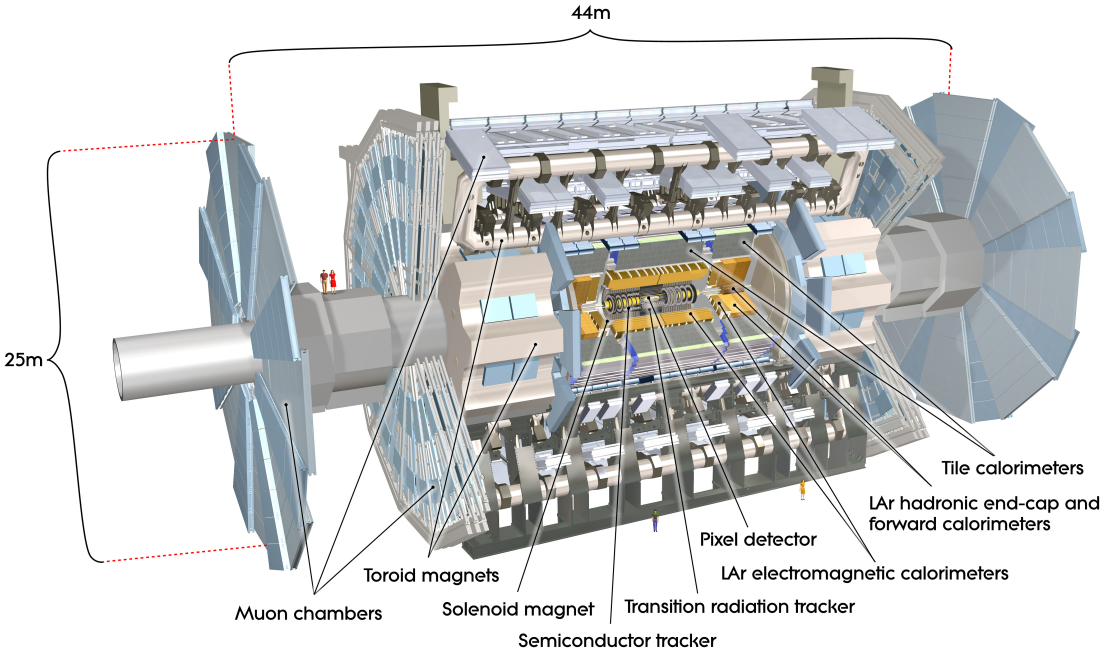

FIGURE 4.2: Illustration of the ATLAS detector with dimensions and detector systems indicated [8].

volume detector ever constructed at a collider. The ATLAS detector was built as a general purpose detector. This means it was designed to perform a broad variety of measurements, which is necessary in order to conduct a diverse physics programme. A sketch of the detector is seen in Figure 4.2. As seen, the detector instrumentation is arranged in a barrel-like shape surrounding the interaction point (IP), measuring 25 m in diameter and and 45 m in length.

4.2.1 Hadron collider nomenclature

The coordinate system of ATLAS is right-handed with z being the axis along the beam direction. The $x-y$ plane is perpendicular to z, with the x-axis pointing towards the center of the LHC ring and the y-axis pointing upwards. The y-axis is slightly tilted with respect to vertical from the general tilt of the tunnel [11]. The detector is symmetric across the $x-y$ plane at $z=0$. Side A is defined to be $z>0$, while $z<0$ is known as Side C [7].

In terms of cylindrical coordinates, R is defined as the perpendicular distance to the z-axis. The azimuthal angle around the z-axis is ϕ and θ is the polar angle away from the z-axis. The variable θ is rarely used since the variable rapidity y is preferred [17]

$$y = \frac{1}{2}\ln\left(\frac{E+p_z}{E-p_z}\right) \tag{4.1}$$

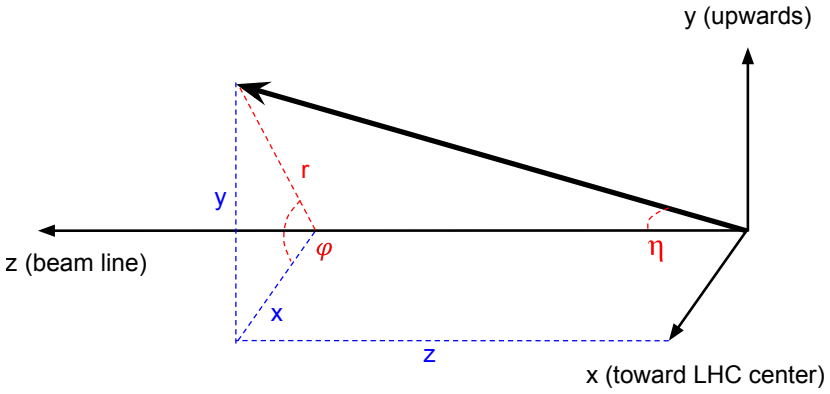

FIGURE 4.3: Illustration of the ATLAS coordinate system. Courtesy of L. Egholm.

where E is the particle energy and p_z its momentum along the z direction. For relativistic particles, that is in the limit $E \gg M$, the variable pseudorapidity η can be used instead of y [17]

$$\eta = -\ln\left[\tan\left(\frac{\theta}{2}\right)\right] \tag{4.2}$$

As pseudorapidity is defined only with respect to θ it has a well-defined and mass-independent interpretation in the lab-frame, and is commonly used when discussing detector performance [36]. The parameter η is also convenient in terms of designing detector systems, since particles are expected to be produced uniformly in rapidity [17]. For this reason detectors are often segmented into pixels in $\eta - \phi$ space. This is also the case for the ATLAS Muon Spectrometer, which has been constructed with a projective geometry.

At hadron colliders, since motion between the parton center-of-mass frame and the hadron laboratory frame is ambiguous and only variables involving the transverse components are invariant under longitudinal boosts, kinematic variables in the transverse plane are more convenient than those defined in the longitudinal direction [36]. The momentum projected onto the transverse plane is defined as [17]

$$p_T = \sqrt{p_x^2 + p_y^2} = p \sin\theta \tag{4.3}$$

We see that for a given momentum the transverse value is uniquely determined by the angle θ.

4.2.2 Detector sub-systems

The task of identifying potentially interesting physics relies on the ability to detect final state particles that have decayed from heavier particles. This boils down to measuring

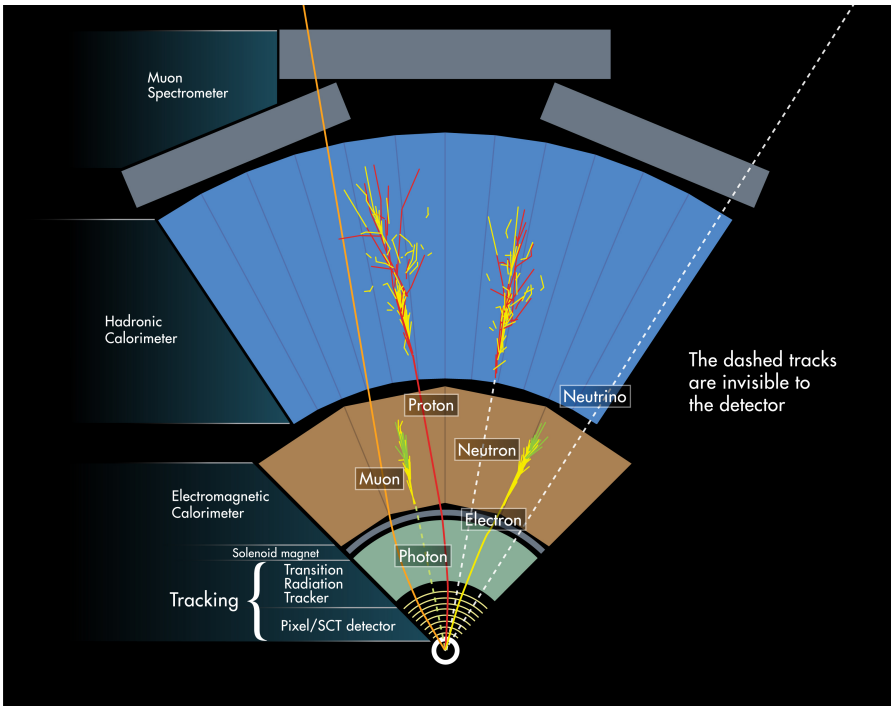

FIGURE 4.4: Illustration of the principle of particle identification with the ATLAS detector [8].

the energy, momentum and position of electrons, muons, photons, neutrinos and light hadrons. For this purpose it is customary to segment the detector into independent detector systems that each is optimized to measure either of the above. The principle of particle identification and measurement with the detector systems of ATLAS is illustrated in Figure 4.4.

The ATLAS Inner Detector (ID) is the first detector system that particles emanating from the primary collisions will encounter. It consists of three sub-detectors: the Pixel Detector (PIX), the Semi-Conductor Tracker (SCT) and the Transition Radiation Tracker (TRT). The ID provides tracking points of charged particles near the IP and measures their transverse momentum by bending them in ϕ with a 2 T solenoidal magnetic field.

Surrounding the ID are the calorimeters, which measure the energy of incident particles by absorbing them. The Liquid Argon calorimeter (LAr) acts as both electromagnetic and hadronic calorimeter, while the Tile calorimter exclusively acts as a hadronic calorimeter. Both are sampling calorimeters.

The outermost detector system is the Muon Spectrometer (MS); a composition of detectors dedicated to measurements of muons. The particles that originate from the primary collisions and impinge the Muon Spectrometer will almost exclusively be muons, since this is the most common final state particle likely to penetrate the calorimeters [1].

[1] Muons with momentum less than 3 GeV will not reach the spectrometer [4, 11, 37]

A review of this particular detector system is given in the following sections.

4.3 The ATLAS Muon Spectrometer

The Muon Spectrometer is with its volume of 16.000 m^3 and surface area of 5500 m^2 by far the largest detector system in ATLAS [4]. It was designed to provide measurements of a broad spectrum of muons, which is needed to optimize the overall discovery potential of ATLAS. The functionality and required performance of the spectrometer was defined from a series of benchmark physics processes such as $H \to ZZ^* \to 4\ell$ and the decay of new vector bosons (Z', W') to leptons, e.g. $Z' \to \mu\mu$ [37]. The spectrometer must fulfil the following [38]

- Identify and reconstruct muon trajectories and measure their momenta
- Associate each muon to its parent bunch-crossing
- Trigger on single or multi-muon event topologies
- Associate measurements to the ID

Currently, four different detector technologies are in use.

4.3.1 Layout and naming convention

An illustration of the spectrometer in the $y-z$ plane is shown in Figure 4.5. It is divided into a barrel region covering $|\eta| < 1.05$ and an end-cap region spanning $1.05 < |\eta| < 2.7$. The instrumentation in the barrel region is arranged cylindrically around the z-axis, while the end-caps are composed like disks mounted perpendicular to it. In both the barrel and end-cap the spectrometer is equipped with three layers of detectors referred to as stations. The innermost, middle and outer layers of the barrel are positioned at $R = 5$ m, 7.5 m and 10.5 m. The end-cap disks are similarly mounted in three stations at $z = 7.4$ m, 14 m and 21.5 m [11].

Each piece of the spectrometer has a code associated with it that identifies its position. The barrel region is denoted B and the end-caps E. The location of a chamber is specified by an I for an inner station, M for a middle station and O for an outer station. The spectrometer is furthermore divided into sectors, which are counted from 1-16 in the ϕ direction. Moreover, two types of sectors are distinguished: small (S) and large (L) [11].

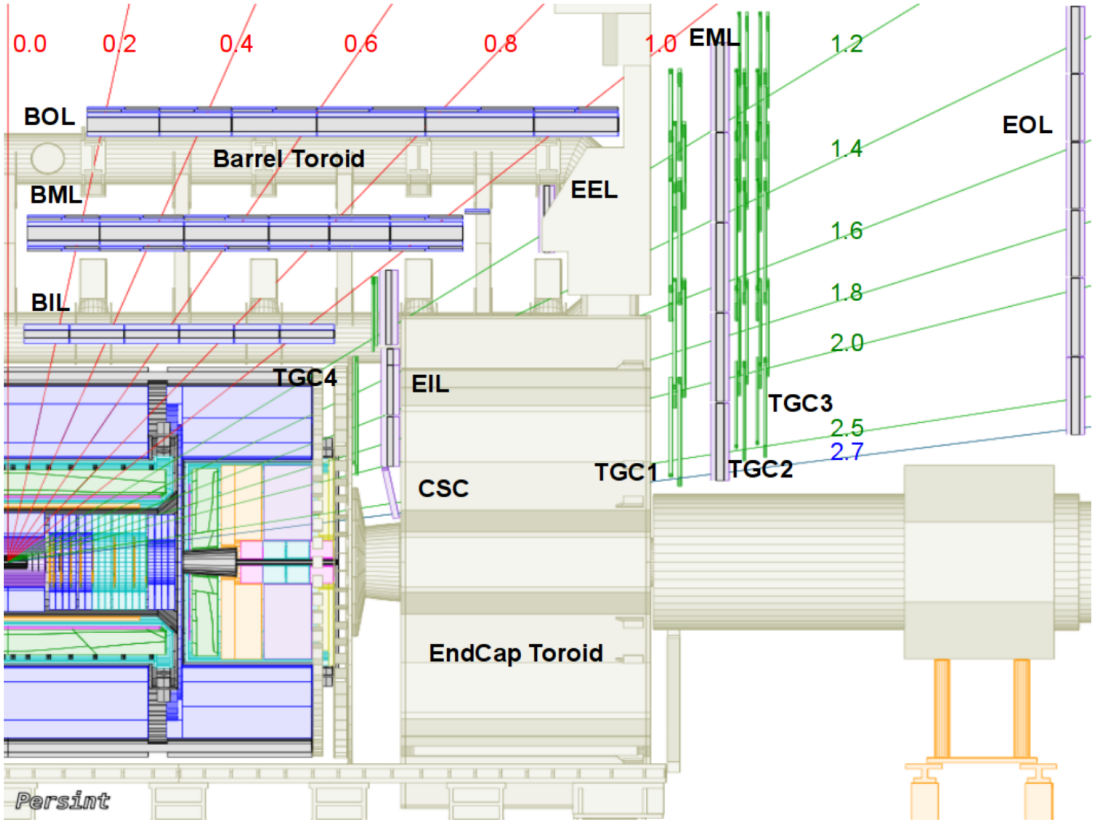

FIGURE 4.5: Illustration of the instrumentation of the Muon Spectrometer seen in the $z-y$-plane with pseudorapidity values indicated [9, 10].

4.3.2 Momentum measurement

A paramount aspect for the performance of ATLAS is the ability to deliver a precise momentum measurement over a wide kinematic spectrum. The Muon Spectrometer works as a magnetic spectrometer, meaning that it determines the momentum of incident muons by measuring the curvature in the trajectory occurring as a result of an applied magnetic field. This principle is illustrated in Figure 4.6.

In both the barrel and end-cap region muons are deflected in the η-plane by toroidal magnetic fields. The magnitude of the fields are $0.5-1$ T in the barrel region and 2 T in the end-caps [11, 37]. We stress the difference in the measurements provided by the Inner Detector and that of the Muon Spectrometer: the solenoidal field of the ID bends charged particles in the transverse plane, which enables the measurement of p_T, whereas the spectrometer directly measures p. The measurement of the latter variable is advantageous since the lever arm of the spectrometer will be longer, which improves the momentum resolution.

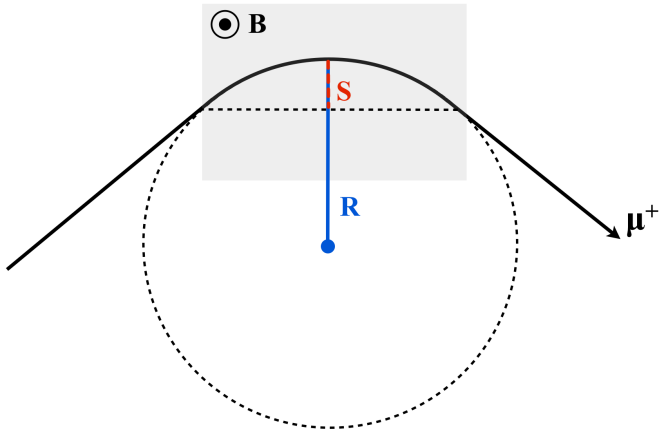

FIGURE 4.6: A charged particle will when entering a magnetic field (grey area) be deflected. The curvature of the track is determined by measuring the sagitta, the line segment marked with S in the illustration.

The momentum (measured in GeV/c) is obtainable from the relation [28]

$$p = 0.2998 B \rho \tag{4.4}$$

with B being the magnitude of the applied magnetic field (in T) and ρ the bending radius of the trajectory (in m). Given an exact mapping of the magnetic field it is possible to extrapolate the reconstructed track to the IP and derive the polar angle, which the transverse projection can be derived from. When performing the extrapolation, the track deflection probability happening as result of multiple scattering in the calorimeters (1-3 mrad [4]) among the energy loss there is taken into account.

As Equation (4.4) implies the trajectories from high-momenta muons will have a larger bending radius, i.e. a smaller curvature. Hence, the momentum resolution strongly depends on the ability to accurately resolve the sagitta of the curvature, which is directly related to the spatial resolution in the bending coordinate. For example, the trajectory from a 1 TeV muon will have a sagitta of $\approx$ 500 μm in the toroidal fields of ATLAS [38]. To resolve this the precision detectors of the Muon Spectrometer must deliver a spatial resolution in the η-coordinate around some tens of μm.

The muon momentum resolution of ATLAS is parametrized according to the following expression [13]

$$\frac{\sigma(p_T)}{p_T} = \frac{p_0}{p_T} \oplus p_1^{MS} \oplus p_2 \times p_T \tag{4.5}$$

It is the sum of three terms with three corresponding parameters: the first term is due to energy loss fluctuations in the calorimeters, the second depends on the multiple scattering and the third is related to the intrinsic hit resolution that in turn depends on alignment and calibration [13]. For $p_T < 100$ GeV multiple scattering is the dominant contributor. Above 100 GeV calibration and alignment of the spectrometer become the

TABLE 4.1: Summary of the functionality of the different technologies used in the Muon Spectrometer along with the coverage in η.

Technology	Primary purpose	$\lvert\eta\rvert$ coverage
MDT	tracking	$0.0 - 2.7$
CSC	tracking	$2.0 - 2.7$
RPC	trigger	$0.0 - 1.0$
TGC	trigger	$1.0 - 2.4$

most significant factors in the resolution [38].

In the kinematic range $5 < p_T < 50$ GeV the spectrometer provides a stand-alone momentum resolution of $2 - 3\%$ [11]. At 1 TeV the resolution approaches 10% [38]. At 3 TeV, the high end of the accessible kinematic range, the stand-alone resolution is still adequate. More details on momentum measurement with a magnetic spectrometer and associated uncertainties can be found in [28, 37].

4.3.3 Background conditions

The anticipated level of particle fluxes in the experimental area is high and this fact has had a great impact on the design of the spectrometer and the choice of instrumentation. In particular, the cavern background rate has introduced limitations on the choice of technologies. The background can broadly be divided into two categories, primary background and radiation background [37], both of which have a rate directly related to the instantaneous luminosity.

The primary background denotes collision products from the p-p interactions that penetrate the calorimeters and enter the spectrometer synchronous in time with the collisions. This often consists of leptonic decays of light hadrons (π and K) and semi-leptonic decays of heavy (c,b,t) flavours, gauge boson decays, shower muons and hadronic punch-through (i.e. particles penetrating the calorimeters) [11].

The radiation background enters the spectrometer from all directions and is not correlated in time to the primary p-p interactions. It consists mainly of photons, electrons, muons and hadrons that originates from primary hadrons that interact with the forward calorimeter, the shielding inside the end-cap toroid, the beam pipe and other machine elements [4]. This background will dominate the counting rates in most areas of the spectrometer [4, 11, 37].

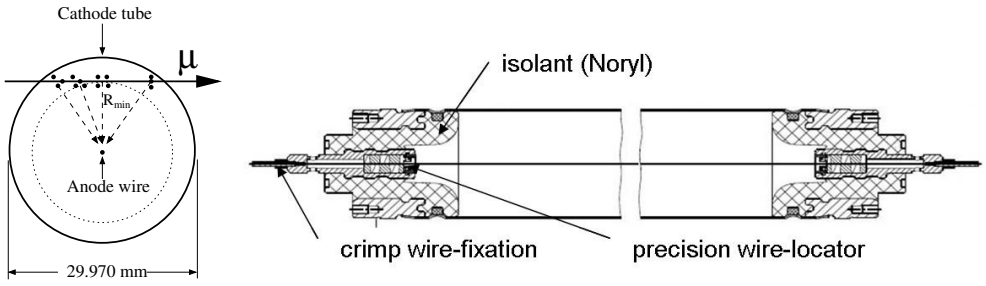

FIGURE 4.7: Left: Working principle of a single MDT (cross-section) [11]. Right: Longitudinal cut-through of a MDT [11].

4.3.4 Precision chambers

The need for excellent space-point measurements in the η-coordinate was motivated by the requirements of good momentum resolution (see Section 4.3.2). In this section we briefly review the working principle and performance of the two detector technologies that currently provide such. A more detailed review including a description of the assembly and read-out electronics can be found in [4, 37].

4.3.4.1 Monitored drift tubes (MDT)

The MDT technology is tailored to the task of precision tracking in the ATLAS Muon Spectrometer. It can at affordable cost cover most of the required area and provide space-points in the bending plane with adequate resolution. As seen in Figure 4.7, a single tube consists of a cylindrical aluminium tube of 29.970 mm in diameter, a W-Re central anode wire of 50 μm, an end-plug that holds the wire in position at the tube ends [11]. All ATLAS MDTs are operated with Ar/CO_2 in the ratio 93/7% at an over-pressure of 3 bar to reduce diffusion and ionization fluctuations. With the wire potential set to the nominal 3.08 kV, the drift speed with these values and particular gas mixture is 20 μm/ns in average which results in maximum drift times of $\approx$ 700 ns [39]. Since the MDTs only measure the bending plane coordinate, the second coordinate must be provided by the trigger chambers.

Three types of calibration are needed for the MDTs: timing offsets, space-time functions ($r - t$ relation) and drift-tube resolution functions [38, 40]. By calibrating the measured drift time with the $r - t$ relation a space-point coordinate can be obtained for each tube. The single-tube resolution depends on the drift distance and has an average value of 80 μm. The cylindrical geometry is highly advantageous, since its measurement accuracy only weakly depends on the trajectory angle [11].

Each MDT chamber in ATLAS is composed of three to eight layers of drift tubes, which when combined provide a resolution of 35 μm [11]. A salient feature of this composition is the high level of operational reliability: the loss of a single tube does not

FIGURE 4.8: A MDT multi-layer under construction [8].

degrade the operation of others. The layout of the MDTs is projective, meaning that the layer dimensions and the chamber sizes increases in proportion to their distance from the IP. 1088 MDT chambers are used to cover the majority of the spectrometer [38]. A picture of a MDT multi-layer before installation in the experimental cavern is seen in Figure 4.8.

Because of the large tube diameter and the high operating pressure, the performance suffers under high counting rates: space-charge effects degrade the spatial resolution and the efficiency of the tubes. The quoted limit for safe operation of the MDTs used in ATLAS is at a counting rate of ≈ 200 kHz/tube [4].

4.3.4.2 Cathode strip chambers (CSC)

Since the limit for safe MDT operation is violated by the harsh background environment in parts of the inner end-cap stations, the CSC technology is used in the range $2.0 < \eta < 2.7$. This technology offers excellent spatial and time resolution exceeding that of the MDT, double track resolution, and safe operation at high counting rates [12].

The CSC is a MWPC with the wires oriented along the η-direction. Its anode-cathode spacing d is equal to the anode wire pitch S, which has been fixed at 2.54 mm in view of the required performance. A sketch of this is shown in Figure 4.9. The cathodes on both sides of the gas gap have been segmented by lithographic etching: one side with the strips perpendicular to the wires and the other parallel to the wires. With this configuration the CSC delivers measurements in both η and ϕ. The signals from the anode wires are in fact not used directly. The CSC is operated with a Ar/CO_2 mixture in the ratio 80/20% with the anode potential kept at 1.9 kV [11].

Under optimal signal-to-noise conditions the CSC provides a resolution of 60 μm per plane in the η-coordinate and 5 mm in the second coordinate. The particles encountering the CSC are measured in four consecutive planes. Since a measurement of the drift time

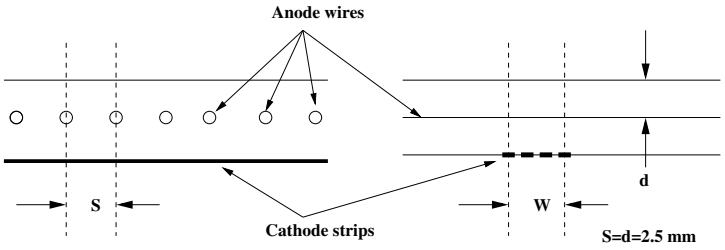

FIGURE 4.9: Structure of the CSC cells looking down the wires. The wire pitch s is equal to the anode-cathode spacing $d = 2.5$ mm [12]

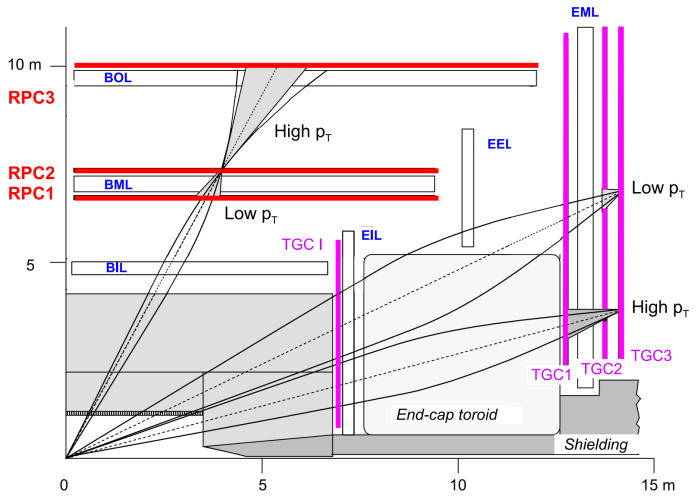

FIGURE 4.10: Illustration of the arrangement of the trigger chambers in the ATLAS Muon Spectrometer [13].

is not involved the CSC is immune to temperature and pressure fluctuations that affect the drift properties. Because the spatial resolution provided by the CSC is sensitive to the angle of the trajectory the CSC chambers are tilted by an angle of 11.59° such that the particles originating from the IP on average are normal to the chamber surfaces [11].

4.3.5 Trigger chambers

The task of the trigger chambers in the spectrometer is to provide fast information about the traversing muons, which allows for a L1 trigger decision based on a coarse measurement of the p_T and multiplicity. The system must futhermore deliver bunch crossing identification and second coordinate measurement to complement the MDT measurement. Two technologies are currently in use.

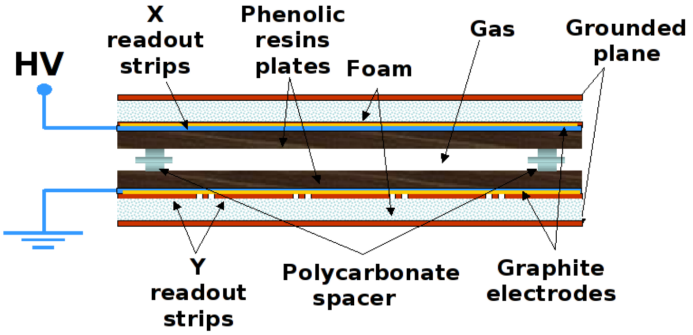

FIGURE 4.11: Schematic of the structure of an ATLAS RPC [14].

4.3.5.1 Resistive plate chambers (RPC)

RPCs are wireless, parallel-plate detectors made with the highly resistive Bakelite[2] as electrodes. A schematic of the technology is shown in Figure 4.11. The electrodes are kept at a fixed distance parallel to each other by the use of insulating spacers with a height of 2 mm, which define the size of the gas gap. A signal is obtained via an AC coupling to metallic strips mounted on the outer faces of the Bakelite plates. The strips are oriented orthogonal to each other in both η and ϕ. In ATLAS each RPC consists of two independent gas gaps, each with its own set of read-out strips. The obtainable spatial resolution is mainly determined by the read-out channel granularity.

The RPCs in ATLAS are operated in so-called saturated proportional mode with a gas mixture consisting of $C_2H_2F_4$/Iso-C_4H_{10}/SF_6 in the ratio 94.7/5/0.3% and a nominal voltage of 9.8 kV. This operation enables the RPCs to deliver an extremely rapid signal with a rise time of $\approx$ 5 ns, with small time jitter and small probability for transition into streamer mode.

In ATLAS the RPCs are exclusively used for triggering in the barrel region. They are assembled together with MDT chambers of equal dimensions and integrated into the same mechanical structure. The trigger system in the barrel consists of three stations, two sandwiched around the MDTs in the BM station and one mounted on the BO station. The large lever arm between inner and outer RPCs permits the trigger to select high momentum tracks in the range 9 - 35 GeV, while the two inner chambers provide the low-p_T trigger in the range 6 - 9 GeV. The two p_T regimes are selected with appropriate tuning of the coincidences [14].

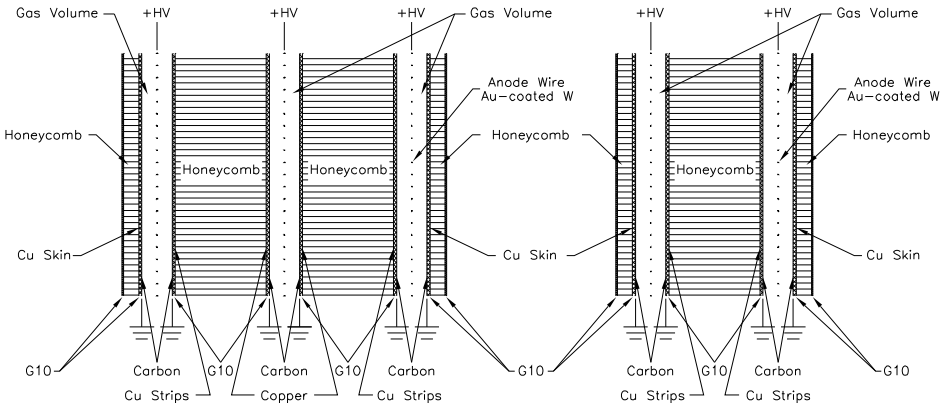

FIGURE 4.12: Cross-section of a TGC triplet and doublet module. The triplet has three wire layers but only two strip layers. The dimensions of the gas gaps are enlargened with respect to the other elements [14]

4.3.5.2 Thin gap chambers (TGC)

The TGCs are similarly to the CSCs based on the classic MWPC. However, they possess the unique characteristic that the wire-to-cathode distance of 1.4 mm is smaller than the wire-to-wire distance of 1.8 mm [11]. The cathode planes consists of 1.6 mm G10 plates, graphite coated on the side facing the wires, with copper cladding on the other side. One of the copper layers is segmented into strips to read out the azimuthal coordinate. Thus, the bending coordinate is measured by groups of the activated TGC wires, while the second coordinate is measured by the strips. By using the highly quenching gas mixture CO_2 and n-C_5H_{12} this particular cell-geometry allows for operation in a quasi-saturated mode, i.e. with a gas gain of $\approx 3 \times 10^5$. TGCs are operated with a nominal voltage of $\approx$ 2.9 kV, which results in a high electric field. The combination of this and the small wire-to-wire distance lead to very good time resolution for the large majority of tracks [11]. A schematic of TGC modules is seen in Figure 4.12.

The Muon Spectrometer is instrumented with TGCs in the end-caps, where they provide trigger and second coordinate measurement. In the EM stations the MDT chambers are complemented by seven layers of TGCs: three in the front of the MDT chambers and four on the backside. The TGC chambers in the EM station measure the slope of the muon tracks with a precision of 2-3 mrad as to only select trajectories pointing to the primary vertex for the L1 trigger (taking the bending from the toroidal field into consideration). In the EI station only two layers of TGCs are used. These do not provide a trigger, only a second-coordinate measurement. Triggering capabilities will be introduced in the EI stations with the NSW.

[2] Also known as phenolic resin [14]

TABLE 4.2: Overview of the LHC running periods with beam parameter specifications and the scheduled upgrades.

Period	Year	$\mathcal{L}$ [cm^{-2} s^{-1}]	$\sqrt{s}$ [TeV]	Bunch spacing [ns]	$\int \mathcal{L}$ [fb^{-1}]
Run I	2010 - 2013	$3.5 - 7 \times 10^{33}$	7 - 8	50	25
		Phase-0 upgrade			
Run II	2014 - 2018	1×10^{34}	13 - 14	25	50
		Phase-1 upgrade			
Run III	2019 - 2022	$2 - 3 \times 10^{34}$	14	25	300
		Phase-2 upgrade			
Run IV	2022 - 2030	5×10^{34}	14	25	3000

4.4 Upgrading the Muon Spectrometer with New Small Wheels

During the first long shutdown (LS1) in 2013-2014 the Phase-0 upgrade will allow for the accelerator energy to be increased to close the design value of 7 TeV per beam. Meanwhile, the luminosity will be increased from $3.5 - 7 \times 10^{33}$ cm^{-2} s^{-1}, which was the quoted value just before LS1, to at least 1×10^{34} cm^{-2} s^{-1}. LHC operation under these conditions, known as Run II, will last until the second long shutdown (LS2), which is to occur in 2018. At this point the Phase-1 upgrade will be initiated, which will increase the luminosity to $2 - 3 \times 10^{34}$ cm^{-2} s^{-1}. This will allow ATLAS to collect approximately 100 fb^{-1} per year. It is in this period that the NSW will be installed. The running period after the Phase-1 upgrade is referred to as Run III. A subsequent upgrade, the Phase-2 upgrade, is planned in 2022, which will make significant changes to the IP region in addition to improvements to other parts of the accelerator complex. These improvements will result in the luminosity increasing to 5×10^{34} cm^{-2} s^{-1}. The integrated luminosity with this ultimate upgrade will be 3000 fb^{-1} after about 10 years of operation. The LHC upgrade plans are summarized in Table 4.2.

Like was emphasized in Section 4.3.4 the rate capability of the MDT technology is strongly limited by the slow collection of the ions. In Figure 4.13 the single tube efficiency and the segment finding efficiency for the ATLAS MDTs is shown versus hit rate. The single-tube efficiency decreases linearly with the rate; at 300 kHz/tube the inefficiency is 35%. The segment finding efficiency remains higher since only a subset of the available hits is needed, however, at a few 100 kHz/tube it becomes degraded.

In Figure 4.14 the hit rate expected in the Small Wheel region is presented as function of the radial distance to the beam-pipe at the beam conditions anticipated after the Phase-1 upgrade. This rate includes both cavern background and primary collision products. The full spectrometer will be subject to a baseline hit rate of some kHz/cm^2

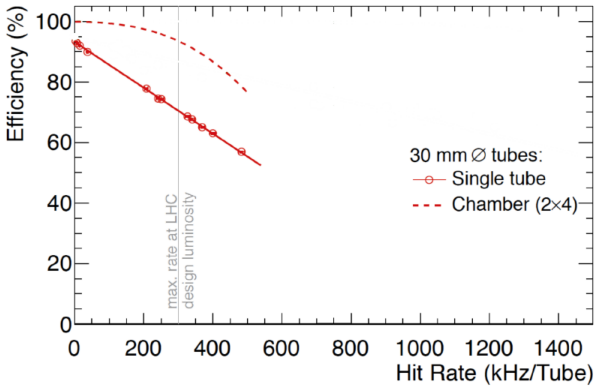

FIGURE 4.13: MDT tube hit (solid line) and track segment efficiency (dashed line, referring to a MDT chamber with 2×4 tube layers) as a function of tube rate estimated with test-beam data. Design luminosity indicates 1×10^{34} cm^{-2} s^{-1}. [4]

with the hottest regions being immersed in fluxes reaching 5 kHz/cm^2. A rate of 0.5 kHz/cm^2 corresponds to a few 100 kHz/MDT tube. Like was explained in Section 4.3.4 this rate is beyond the safe limit for the MDT technology. An alternative technology must therefore replace it.

The high rate is not only going to be a problem for the precision chambers, but will in addition be challenging for the L1 trigger. To keep the L1 acceptance rate at a tolerable level, a stronger suppression of sub-threshold muons in the high-p_T trigger as well as better rejection of tracks not originating from the primary IP is needed [4]. This can only be achieved if trigger capabilities are added to the Small Wheels. We will not go into details with the triggering-aspect in this thesis, but instead refer to [4].

In summary, the ATLAS Muon Spectrometer must be upgraded in order to fulfil its required tasks after 2018. The precision chambers in the Small Wheels must be replaced with instruments that are better suited for the increased particle rate, and trigger chambers must be added as well to keep the L1 acceptance rate at a tolerable level.

4.4.1 Detector technologies for the NSW

The performance of the new detectors should as least be as good at high luminosities as the present are at low luminosities, and they must provide all functions mentioned in the previous sections. Several combinations of multiple technologies were proposed for the NSW instrumentation, including modified versions of the already-existing MDT, RPC and TGC technologies. The final decision fell on a combination of the sTGC technology and the MicroMegas technology.

MicroMegas was chosen because of its excellent tolerance of high rate and good spatial resolution, a unique combination of properties that enable it to operate over the

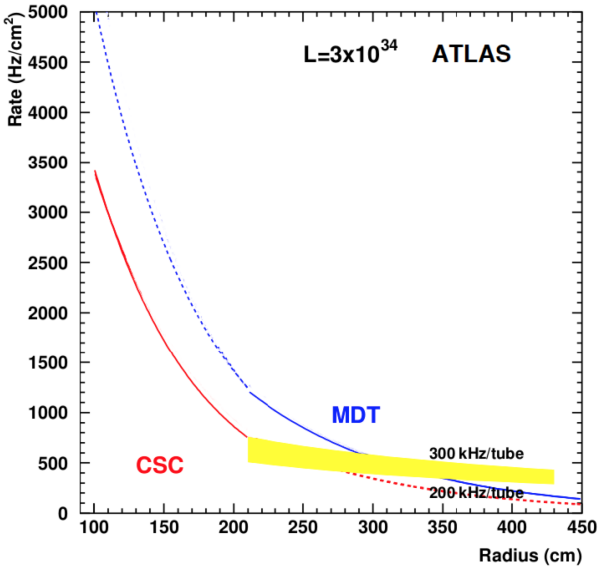

FIGURE 4.14: Extrapolated hit-rate in the CSC and MDT chambers at luminosity 3×10^{34} cm^{-2} s^{-1} at $\sqrt{s} = 7$ TeV as a function of the radial distance from the beam-pipe. The yellow band indicates the radii where the MDTs will reach the rate 300 kHz/tube [4].

full η-coverage of the NSW. It was mainly selected for the purpose of precision tracking. For triggering, sTGC detectors were chosen. This technology consists of TGC detectors with a strip pitch much decreased from the present, hence the name Small (s) sTGC. We will not treat the sTGC technology in this thesis, but refer to [4] for an in-depth treatment.

The two NSW technologies are able to complement each other for their corresponding primary functions. sTGC may contribute to offline precision tracking because they are able to measure track hits with a resolution better than 150 μm (depending on the track angle). The MicroMegas detectors will as well possess the ability to trigger due to its good time resolution and it will be deployed to supplement the sTGCs, increasing redundancy and robustness of the forward trigger [4].

Each NSW will be composed of 16 detector planes contained in two multilayers. A multilayer will comprise four sTGC and four MicroMegas detector planes. The MicroMegas planes will contain both η-segmented strips and stereo-angle strips (inclined $\pm 1.5^\circ$ with respect to η). The choise of eight planes per technology was dictated by the need for a robust detector system; tracks will be reconstructed reliably and with high precision despite the challenging radiation levels, even if some planes fail to work properly. It will further ensure an overall efficiency close to 100% both for online and offline track reconstruction [4]. Both technologies will cover up to $|\eta| = 2.7$.

The NSW will be composed of 16 sectors, 8 large and 8 small, which be assembled to constitute a disk. This scheme is adapted from the present layout and is visible in

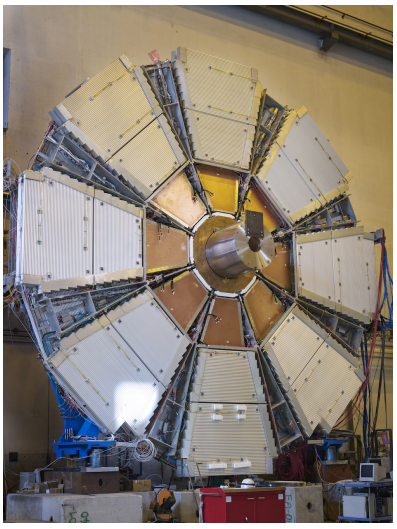

FIGURE 4.15: A fully assembled Small Wheel. Each Small Wheel is approximately 9.3 m in diameter and weighs 10 tons [12].

Figure 4.15. The final layout of both large and small MicroMegas sectors is shown in Figure 4.16. Each sector will be covered by a single MicroMegas detector, which will be over 3.5 m long and up to 2.2 m wide.

4.4.2 Milestones of the MAMMA Collaboration

The size of the MicroMegas detectors needed for the NSW is unprecedented. Therefore, a set of properties had to be demonstrated by the MAMMA Collaboration before the technology was accepted by the ATLAS community. This concerned a list of milestones that would demonstrate detector performance, aging properties and in particular the large-scale feasibility of the technology. The list of milestones included

- Demonstrate that a single-plane spatial resolution < 100 μm is obtainable for inclined tracks
- Demonstrate that detectors with dimensions similar to those in the NSW could be constructed with adequate mechanical precision. A functional prototype with dimensions of at least 1×2 m^2 had to be constructed before the end of 2012
- Demonstrate that sparks do not damage the detectors permanently
- Demonstrate that detector operation in a magnetic field can provide the required spatial resolution

All points had been demonstrated in the beginning of 2013 via the combined efforts of the MAMMA Collaboration. This thesis will describe the work towards the fulfilment

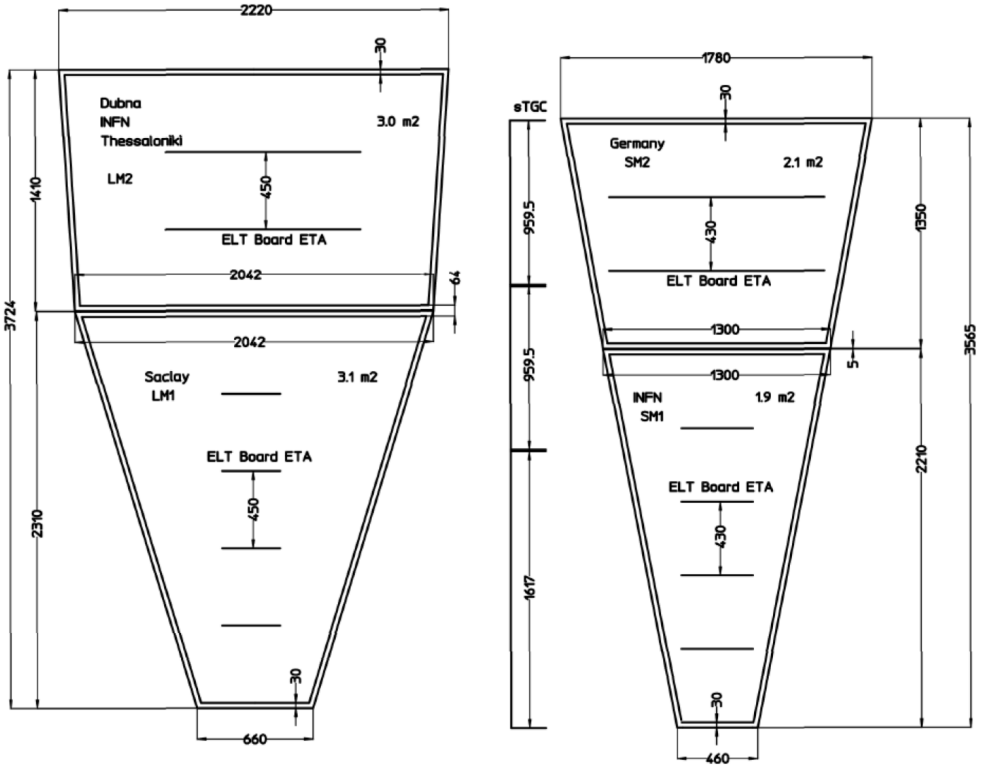

FIGURE 4.16: Layout of the large (left) and small (right) MicroMegas sectors needed for the NSW. All distances are in mm. Courtesy of the MAMMA Collaboration.

of the first two points, which mainly took place at CERN. The latter two points are treated in [4].

Part II

Experimental Work

Chapter 5

Test-Beam and Basic Setup

An extensive test-beam campaign was conducted by the MAMMA Collaboration during the summer and fall of 2012. It was dedicated to the performance studies of a large quantity of MicroMegas detectors, which was needed to fulfil the ATLAS-contextualized milestones mentioned in Chapter 4. The studies presented in the forthcoming chapters will either rely on the data recorded at this occasion or on the experimental equipment. A review of the campaign and its setup therefore follows in this chapter.

5.1 Experimental setup

The test-beam activities took place at the Super Proton Synchrotron (SPS) H6 beam line between the dates 27/7/2012 - 2/11/2012. A schematic overview of the configuration of the MicroMegas detectors in the setup is shown in Figure 5.2. The maximum number of detectors simultaneously installed was 25. The MAMMA Collaboration was the main user of the H6 beam line for most of the period; in the few weeks where this was not the case, data taking was done parasitically (i.e. the setup was moved downstream to allow the main users to install their equipment). The line was tuned to deliver a 120 GeV π^- beam with an intensity ranging between 5 and 30 kHz over an area of approximately 2 cm^2.

The T series comprises 8 single-coordinate bulk chambers produced in the CERN PCB workshop. These chambers are spark-protected with resistive strips and carry the specifications listed in Table 5.1. All T chambers were installed in so-called Freiburg frame[1]; a schematic side-view and pictures of this configuration are shown in Figure 5.3 and 5.4. This frame contained four planes separated by $\approx$ 190 mm that were rotatable about a horizontal axis perpendicular to the beam direction. The T chambers were mounted on these planes pairwise back-to-back. By rotating the planes, the track impact

[1] A frame donated by the Freiburg group

FIGURE 5.1: The pit at the H6 beam line where the MicroMegas test-beam campaign was conducted.

TABLE 5.1: Characteristics of the chambers installed in the test-beam.

Chamber(s)	Strip pitch [μm]	Strip width [μm]	Active area [cm^2]
T	400	300	10×10
L1	450	300	100×100

angle was specified. The chambers installed at the ends of the Freiburg frame, the Tmm chambers, will not be used in this thesis and a description is hence omitted.

In front of the Freiburg frame was the L1 chamber installed. With an active area of 1×1 m^2 this was the largest MicroMegas chamber constructed at the time. Its specifications are summarized in Table 5.1. A detailed description of this chamber is deferred to Chapter 7 where its basic performance is studied. L1 was installed on a table that was movable in both x and y direction. It was hence possible to scan the chamber with the beam and to radiate specific parts.

5.2 Detector operation

High-voltage to L1 and the T chambers were supplied with coaxial cables from a CAEN SY2527 mainframe onto which two high-voltage modules were connected: one A1821N module with 12 channels of negative polarity, and a A1821P module with 12 channels of

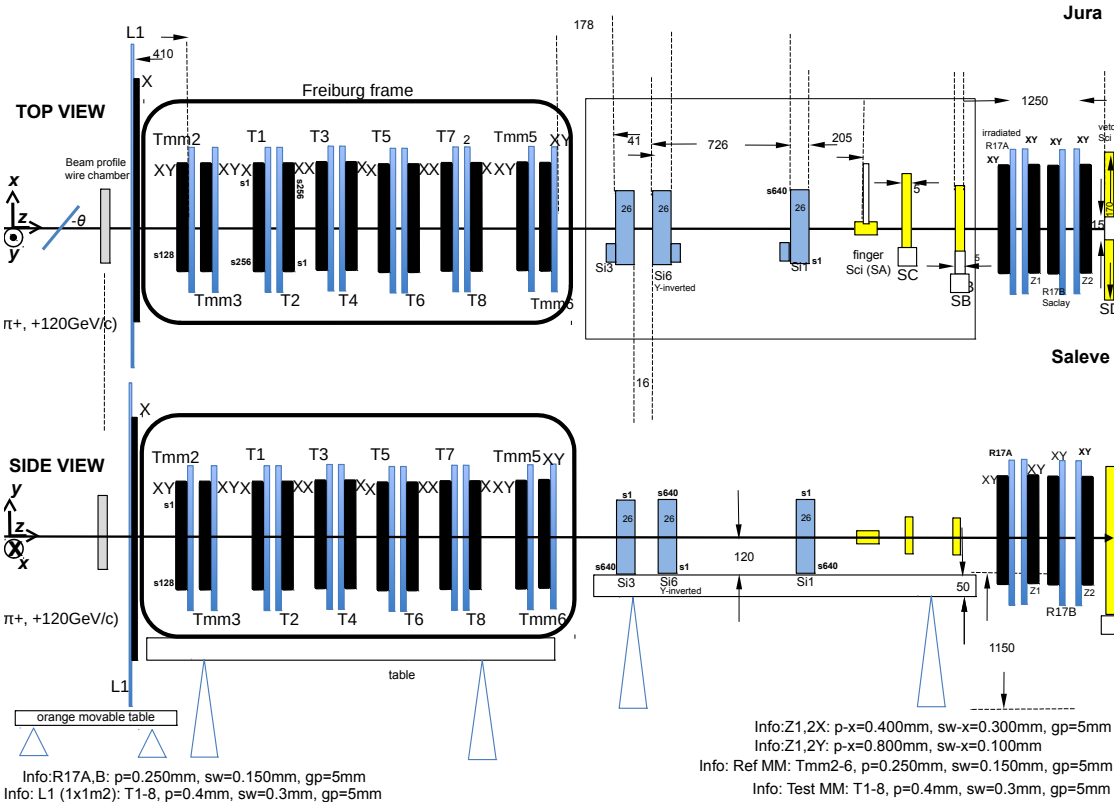

FIGURE 5.2: Drawing of the arrangement and the position of the detectors installed in the test-beam setup as seen from the top and the side. Courtesy of T. Alexopoulos.

positive polarity. Unless otherwise specified, the T chambers were operated with -300 V applied to the drift electrode and 500 V to the resistive strips. RC-filters were applied to all high-voltage lines. The chambers were connected in series to the same gas line and were operated with a gas mixture of Ar/CO_2 93/7% at a flow of ≈ 5 L/hour.

5.3 Trigger and data-acquisition

A global trigger was used for the full setup. It was provided by a coincidence of three scintillators (labelled SA, SB and SC in Figure 5.2) in conjunction with an anti-veto from a scintillator containing a $\varnothing$ 20 mm hole. The scintillators were placed behind the frame with the T chambers in order to limit the amount of material upstream of the detectors. The trigger logic was implemented with modular electronics.

The data acquisition was based on the so-called Scalable Read-out System (SRS); a multi-channel read-out system usable for a broad variety of detector technologies. Owing to its modular architecture the system is scalable and can be accustomed to smaller laboratory setups as well as larger LHC-like systems. In its simplest configuration it consists of on-detector electronics and an adapter card plus front-end (FEC) card housed

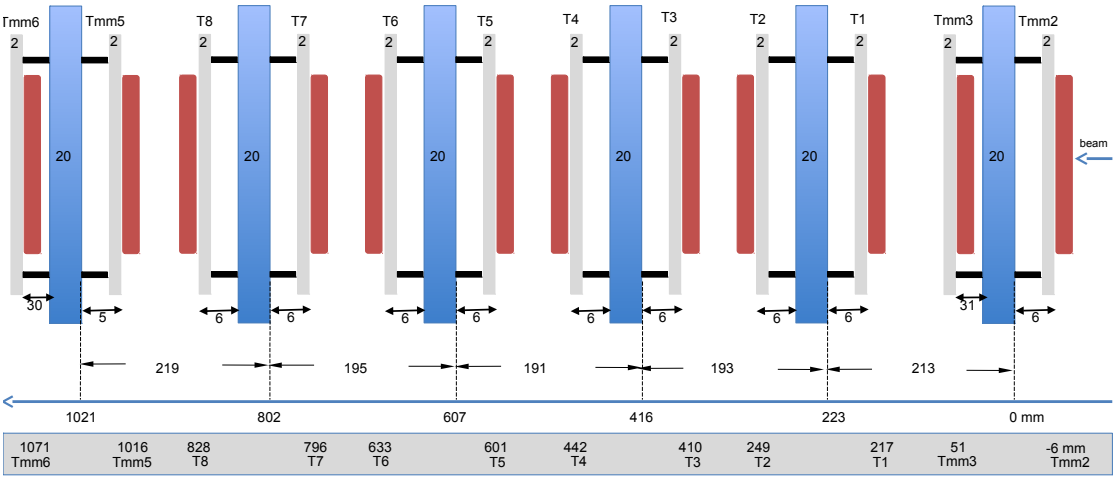

FIGURE 5.3: Drawing of the installation of the T chambers on the Freiburg frame. The blue areas represent the rotatable planes onto which the T chambers were installed. Courtesy of T. Alexopoulos.

in a 3U minicrate [41].

The on-detector electronics used in the campaign was the APV25 hybrid. One hybrid contains 128 channels, which each are AC coupled to one read-out strip of the detector. Each channel contains a pre-amplifier, CR-RC shaper with adjustable shaping time and has a spark protection system implemented. The hybrid records the value of the shaped signal every 25 ns and stores it in an analog memory consisting of a 192 celled pipe-line. The signal is read out upon a trigger signal. The number of samples in one acquisition window is user defined, and the trigger time delay must hence be adjusted by the user to synchronize the trigger with the acquisition window.

The APV hybrids are connected to the adapter boards using commercial HDMI cables. One cable can serve two APV hybrids (a master and a slave card) that can be connected through a 16-lead flat cable. The hybrid cards are connected to the detector ground through two low-ohmic low-profile RF coaxial connectors, which also serve to fix the hybrid card mechanically.

The adapter board contains the analog-to-digital converter (ADC) and links to the back-end of the system. The FPGA-based FEC boards contain most of the complex circuits of the DAQ. The FEC board receives the trigger signal as a NIM or LVDS signal, and sends the data to a computer via an ethernet-link. The adapter and FEC are installed either in a 3U minicrate or a standard 6U eurocrate containing also power supply. Each SRS adapter/FEC card can receive up to eight HDMI cables and handles up to 2048 channels. A minicrate can house two adapter/FEC cards, a 6U eurocrate up to eight [41].

All data-taking was monitored and controlled by the MMDAQ software, a dedicated

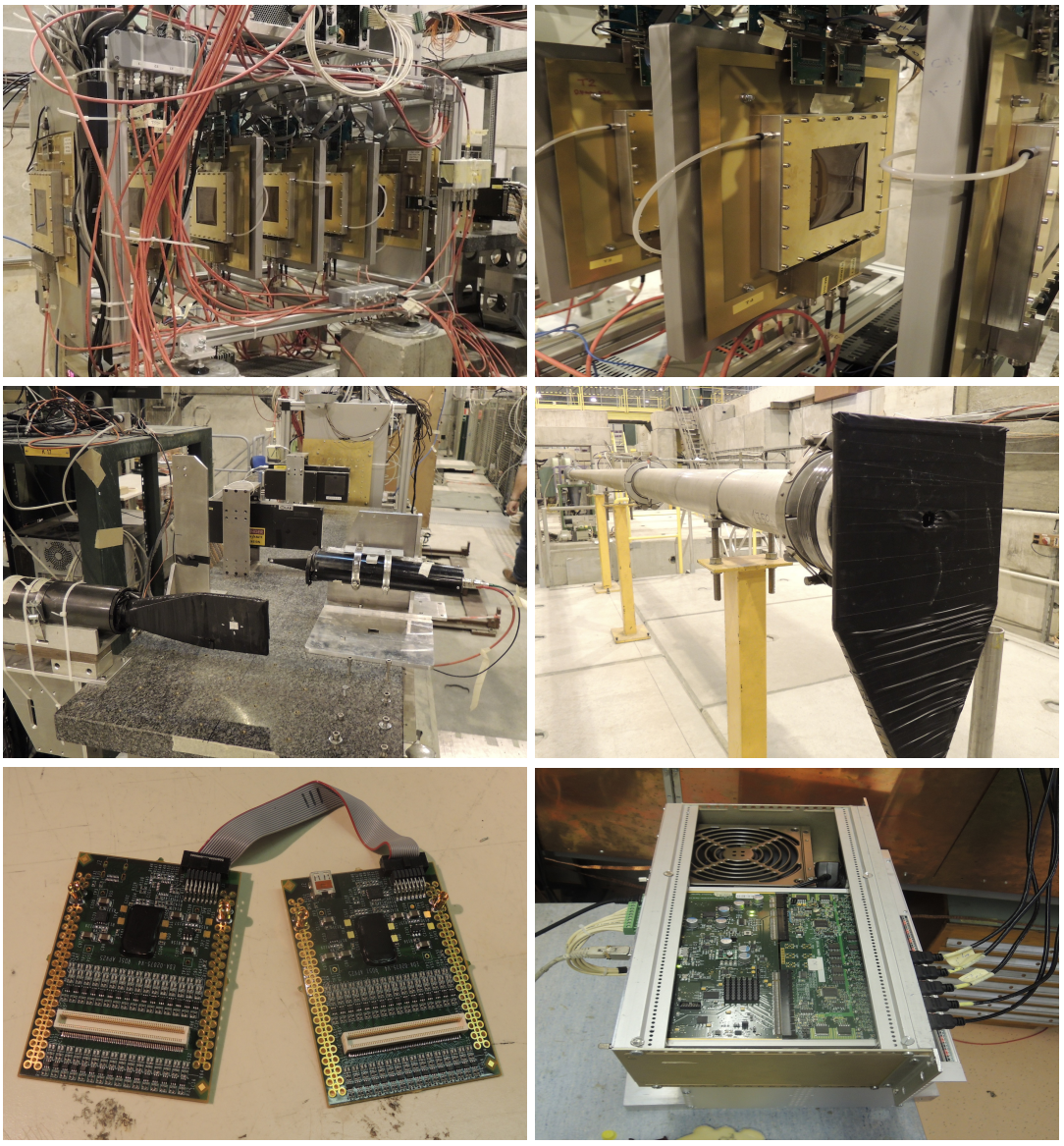

FIGURE 5.4: Top left and right: The T (and Tmm) chambers installed in the Freiburg frame. Middle left: The two scintillators in the foreground (among one more) provided the trigger signal. Middle right: The veto scintillator. Lower left: An APV master-slave pair. Lower right: The adapter and FEC boards mounted in the SRS minicrate.

software system developed within the MAMMA Collaboration.

The MMDAQ application determines the pedestals with a standard procedure. Before physics runs are initiated, a pedestal file is measured with an internal trigger with a user specified frequency. The charge in all time samples of these events is evaluated and the average and standard deviation is found. During physics data taking, in each event the average pedestal value is subtracted from the time samples. The remaining charge values (both positive and negative) are summed and compared to the pedestal standard deviation multiplied with a user specified number n. Events containing an amount of charge greater than the latter are stored with the pedestal subtracted. By varying n,

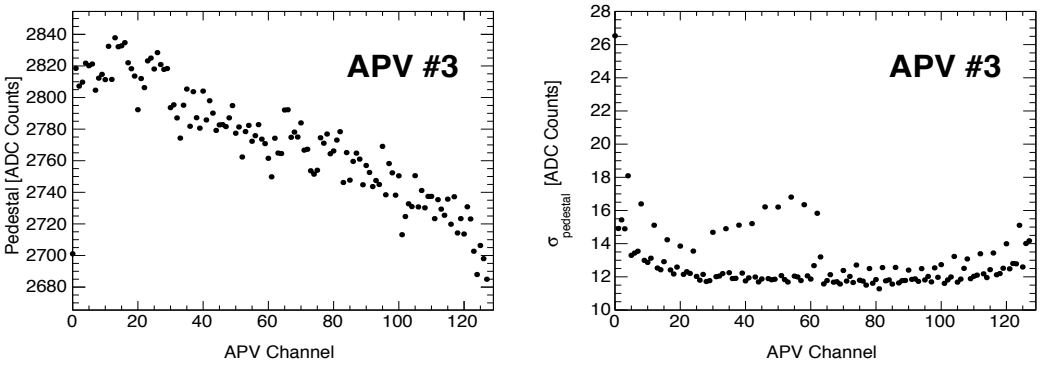

FIGURE 5.5: Distribution of pedestals (left) and pedestal standard deviation (right) as a function of channel number measured with a T chamber in the test-beam campaign.

the user can suppress noise.

An example of pedestals from one APV mounted on a T chamber during the test-beam campaign is shown in Figure 5.5. As seen, the pedestal value for the 128 channels is not constant, but decreases with channel number. The pedestal standard deviation also follows a certain trend, being larger in the channels closer to the edges. These trends occur because each channel is characterized by its own electrical conditions, governed by factors such as grounding, stray capacities from external sources in the setup and the layout of the APV hybrid. The latter factor makes some channels more susceptible to noise, which explains why the pedestals from a certain group of channels are characterized by a higher standard deviation.

In each beam spill, which lasted 10 s, 1000 events could be recorded, limited by the capacity of the DAQ system. Usually 20k events were recorded per run.

Chapter 6

Spatial Resolution

The technology chosen for precision measurements in the NSW will have to provide a single-plane resolution of maximum 100 μm over its full coverage, which is needed to obtain adequate muon momentum resolution [4]. One of the tasks required of the MAMMA Collaboration therefore concerned demonstrating this capability with the MicroMegas technology. The test-beam campaign described in Chapter 5 was, among other tasks, dedicated to demonstrating this feature.

Space-point reconstruction with strip detectors often relies on the traditional cluster charge centroid method. With this method the spatial resolution of a strip detector with sub-mm pitch and analog read-out can easily go below 100 μm [4]. The precision of the charge centroid method is however strongly dependent on the inclination of the particle track, being less favorable with increasing angle. Therefore, to maintain adequate performance, the so-called μTPC method was developed and refined to complement the charge centroid method. With this technique, the drift region of the MicroMegas is exploited as a drift chamber operated in TPC mode. This allows for reconstructing a track segment and thereby determining both space-point of the cluster and the angle of incidence. The μTPC technique is in contrast to the charge-centroid method expected to gain precision as the inclination of the incoming track increases and the two methods are thus able to compliment each other.

We here demonstrate the two methods, compare them and afterwards combine them to prove that a spatial resolution close to the desired is obtainable for inclined tracks up to 40°. Our analysis procedure will be based on that presented in [42, 43]. This study will not involve optimization of the analysis, but will merely act a as a proof of concept of the measurement techniques. Our results will be compared to those of the MAMMA Collaboration, which are summarized in the NSW TDR [4].

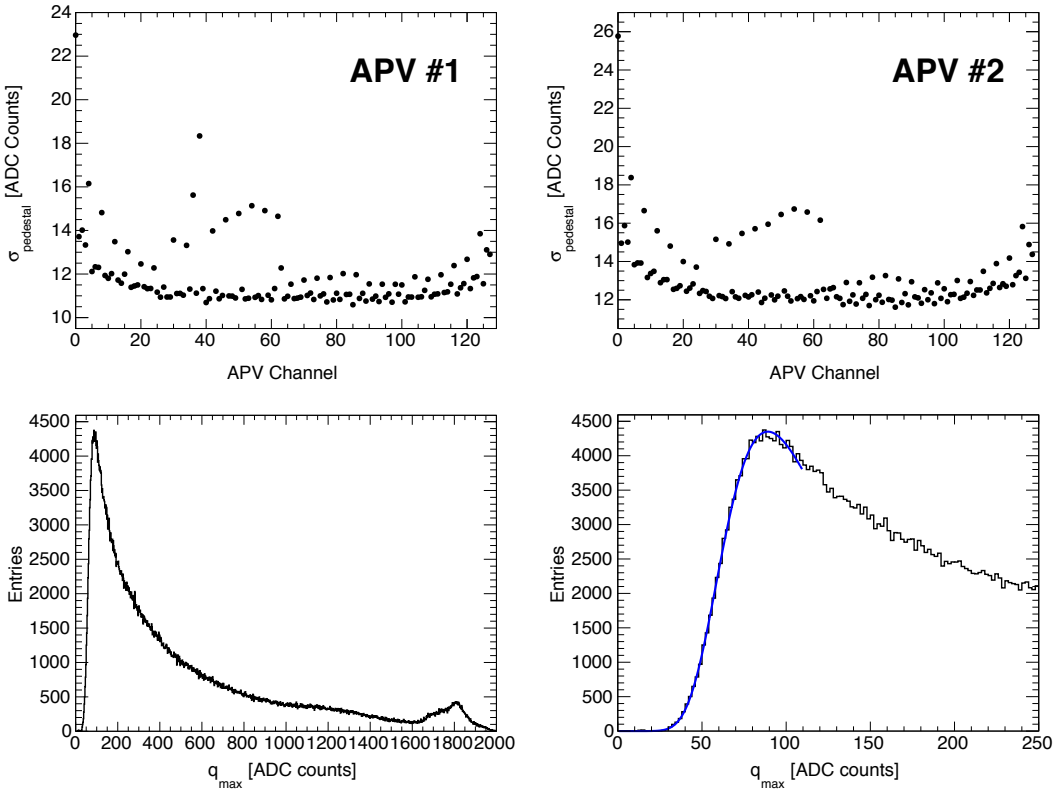

FIGURE 6.1: Top plots: The pedestal standard deviation per channel from the first four APVs installed on the T chambers. Bottom plots: The pulse-height distribution measured with all strips in the T1 chamber.

6.1 Experimental setup

This analysis is performed with data measured with the T chambers in the test-beam campaign. The setup, detector operation and DAQ system follow that described in Chapter 5. Four specific runs recorded at 10°, 20°, 30° and 40° are selected for the analysis. The T chambers were in these runs operated with 500 V.

6.2 Clusterization algorithm

As a first step an algorithm must be implemented that appropriately selects clusters, which involves associating groups of activated strips per event. Slightly different algorithms have been used by the community and we therefore explain our algorithm here in detail.

Our algorithm is initiated with a scan over all strips in the given detector. A strip is selected if it contains a signal with a pulse-height that passes a predefined threshold. Neighboring selected strips are merged into a cluster until a strip fails the selection. Our

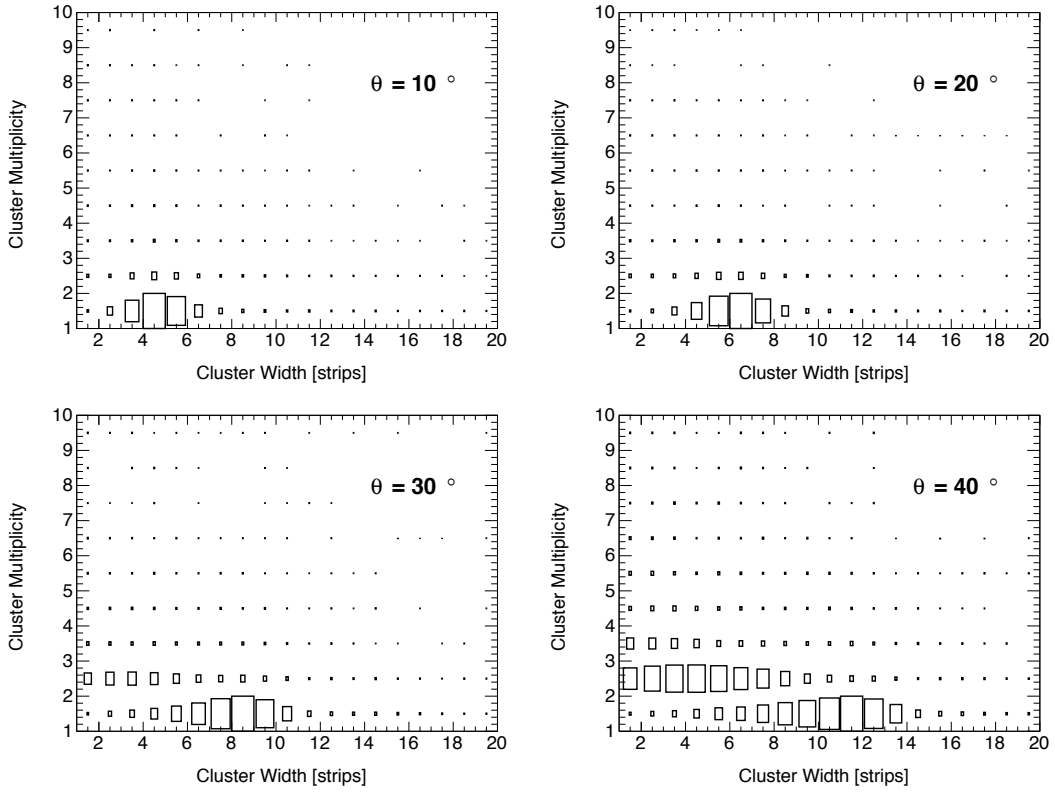

FIGURE 6.2: The cluster multiplicity vs. the cluster width measured with T1 at the four chamber rotations.

algorithm hence selects clusters without any holes and allows for multiple clusters per event.

6.2.1 Strip selection

A strip is selected if the pulse-height of its signal exceeds a predefined threshold. This threshold must suppress noise in the form of random pedestal fluctuations, but must allow selection of signals with small pulse-heights. The algorithm should also reject strips going into overflow.

Although the pedestals are subtracted during data-taking, baseline fluctuations may propagate to the physical signals. The minimum charge threshold is therefore chosen by examining the spread of the pedestals. In Figure 6.1 the standard deviation of the pedestals is shown for each of the 128 channels from two APV hybrids, which in the test-beam campaign were installed on the T1 and T3 chamber. The fluctuations vary within the range 10-20 ADC counts.

If the threshold is too high the clusterization algorithm will reject physical signals with modest pulse-heights. In Figure 6.1 the spectrum of pulse-heights from all strips measured with the T1 chamber is shown in two different ranges. We notice that the

TABLE 6.1: Required cluster width for different chamber rotations.

Angle	Cluster width [strips]
10°	2-7
20°	4-11
30°	4-11
40°	5-15

shape of the low pulse-height tail, beginning from 30 ADC counts, is smooth and looks physical and that it is well described by the Landau fit that is imposed to it[1].

The value for the minimum charge threshold is set to 50 ADC counts. This value corresponds to twice the maximum pedestal fluctuation and only rejects a negligible fraction of physical signals. Since the distribution goes into overflow around $\approx$ 1600 ADC counts[2] (observed as the bump in the distribution in Figure 6.1) the pulse-height at each strip is required to be below this value to avoid including saturated events.

6.2.2 Cluster selection

A cut is imposed to the cluster width. This cut is chosen according to the rotation of the chamber in the given run. In Figure 6.2 the relation between the cluster multiplicity and width is depicted for the four selected chamber rotations measured with the T1 chamber. At 10° the majority of events contain one cluster with a width of 4-5 strips. As the rotation increases the clusters spread out, which results in both larger clusters and increased multiplicity. The latter feature is caused by the large clusters occasionally breaking up into smaller ones, and is directly related to the allowed number of holes in the cluster. Our allowed cluster sizes are listed in Table 6.1; these follow the selection from [42, 43].

Since a tracking algorithm is not implemented, only single-cluster events containing no holes (i.e. strips that do not pass the charge threshold) are selected. Since the probability of holes in a cluster increases with the track inclination we expect our sample size to be smaller for the runs recorded at the largest chamber rotations. We asses that this is tolerable due to the reasonably large data sets.

[1] Parameters from this fit have deliberately been excluded since we merely intend to illustrate the approximate shape of the distribution

[2] This varies from channel to channel and depends on the shaping time

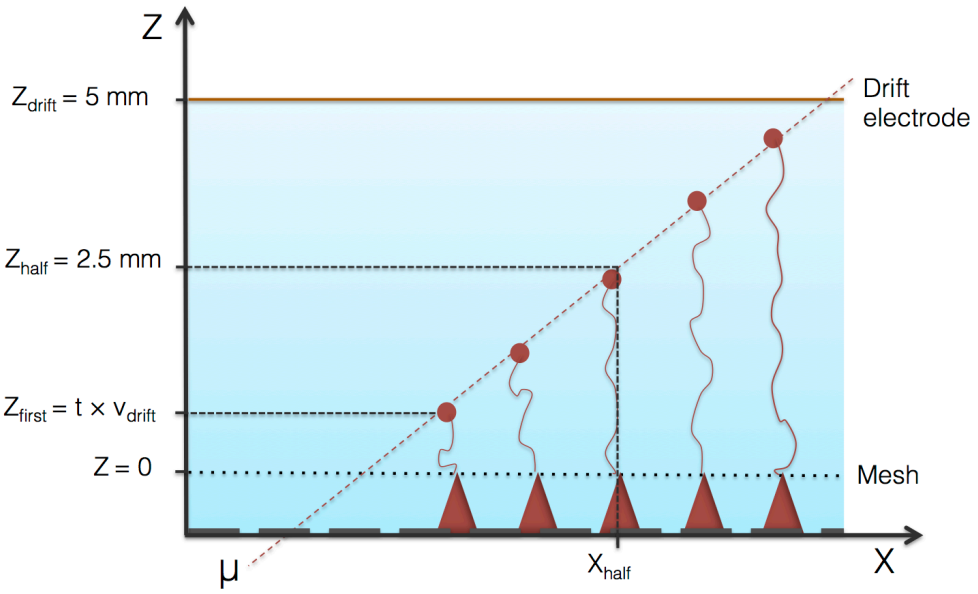

FIGURE 6.3: Illustration of the μTPC principle with a MicroMegas detector (individual parts not to scale). The region under the mesh represents the amplification region with the red cones being electron avalanches.

6.3 The μTPC method

With the μTPC method the few-mm conversion gap of a MicroMegas detector is used as a drift chamber. This means that the space-points of origin for the primary electrons in the cluster are reconstructed by measuring their drift time to the amplification region. This principle is illustrated in Figure 6.3. In the following t_i will denote the drift time of the hit at the ith strip, which is located at the coordinate x_i. When operating in μTPC mode the timing resolution of the detector and its associated electronics must be excellent; otherwise, the relative drift speeds will not be distinguishable[3].

6.3.1 Measuring the drift time

The drift distance of each hit, z_i, is determined by measuring the the drift time t_i and calibrating with the $z - t$ relation. To measure t_i, the detected pulse in the ith strip, i.e. the shaped output of the charge integrating pre-amplifier, is reconstructed. The parameter t_i can hereafter be extracted from the pulse by fitting its rising edge. In principle the time-bin for the occurrence of the maximum pulse-height could be used. This would however yield a rather imprecise measurement since the pulse is only measured every 25 ns with the APV hybrid.

[3]Studies assessing the timing of the MicroMegas detectors in test-beam are presented in [4]

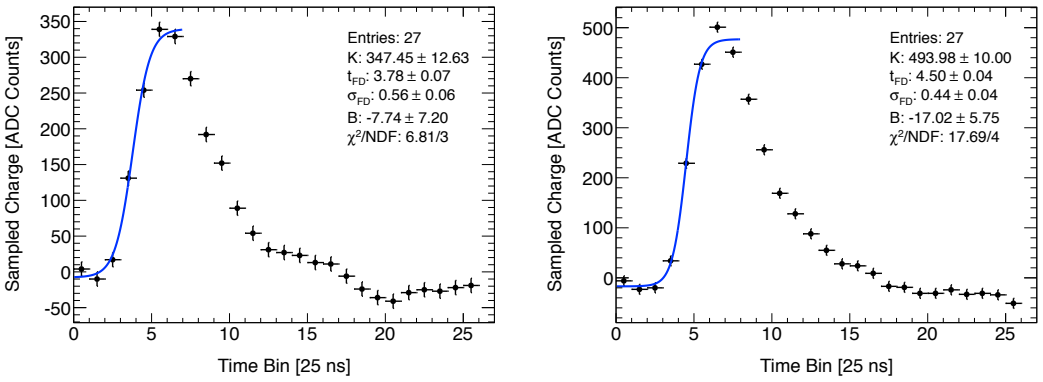

FIGURE 6.4: Pulses from the T1 chamber. The Fermi-Dirac fit is imposed to the pulse to measure the drift time t_i.

Several fitting functions have been tested by the community [44]. In the following we exclusively use the Fermi-Dirac (FD) function [42, 43, 45]

$$FD(t) = K\frac{1}{1+\exp(-\frac{x-t_{FD}}{\sigma_{FD}})} + B \tag{6.1}$$

Here K models the height of the function, t_{FD} provides the time at half of the height and σ_{FD} denotes the slope of the function. The parameter B is added to account for baseline shifts. The parameter t_{FD} extracted from the fit of each strip will in the following be used for the measurement of t_i.

Examples of reconstructed pulses with FD fits are displayed in Figure 6.4. A systematic error of 12 ADC counts is attributed to the charge, which corresponds to the average pedestal fluctuation seen in Figure 6.1. As seen from Figure 6.4 the FD fit behaves quite nicely; the level of the baseline is rather accurate and the function describes the rise of the pulse well. Moreover, based on the χ^2/NDF, the quality of the fits are reasonable. No quality cuts based on the FD fit are applied – for a treatment we refer to [43].

6.3.2 Measuring the drift velocity

In order to perform the μTPC the drift velocity has to be known. This can be estimated with simulation tools like Garfield++, but it can also be measured directly from the data. By assuming that the largest obtained t_i corresponds to the longest possible drift distance (5 mm) and the smallest t_i to the shortest possible (0 mm), the width of the t_i spectrum provides an estimate of the drift time over 5 mm.

In Figure 6.5 the spectra of drift times measured at all four angles are presented. At all angles the rising edge is steeper than the falling. The cause of this is not known, but it is likely to be because the electrons traveling a longer distance will be subject to more diffusion.

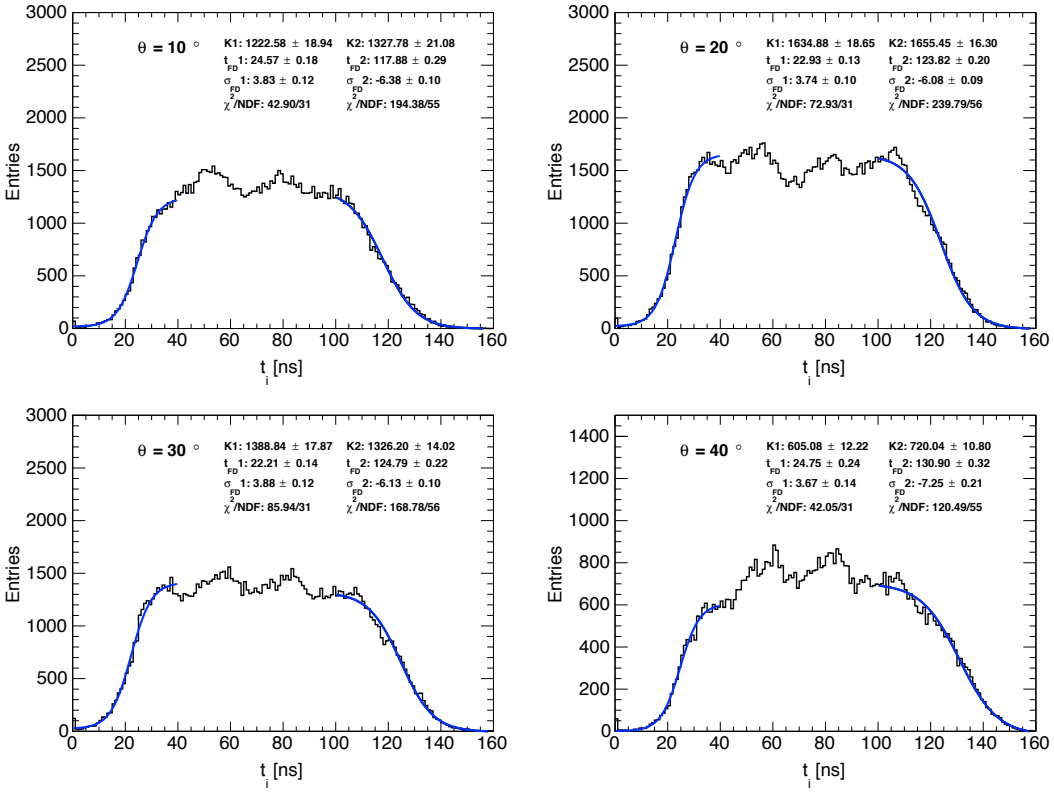

FIGURE 6.5: Drift time spectra measured with T1 at four different angles. A Fermi-Dirac fit is imposed to both the raising and falling edge of the distribution in order to extract the drift velocity.

To extract the drift time a FD fit is imposed to both the leading and falling edge of the distributions in Figure 6.5. The width of each distribution is defined as the difference in the extracted time parameters, Δt_{FD}. This is converted to drift velocity by assuming the maximum drift distance is 5 mm. The obtained drift velocities are summarized in Table 6.2. The error on Δt_{FD} is obtained by folding the error on the rising and falling t_{FD} in quadrature. The uncertainty in the drift distance is ignored in this calculation.

We see that the obtained drift velocity has an angular dependence, decreasing with increasing angle. A possible explanation for this is that the last arriving electrons are more likely to go undetected in smaller clusters, since it will overlap in time with the previous on the same strip. As a result is a fraction of the last arriving electrons lost and the drift velocity appears larger. For inclined tracks the cluster spreads over more strips, and the overlap in time is thus less likely to occur. Therefore, the drift velocity measured at the largest inclination is in principle the best measurement.

The drift velocity was simulated with Garfield++ in [42] and was found to be 4.7 cm/μs. This value is in good agreement with our measurement at 40°, and we will thus continue with the value $v_{drift} = 4.71 \pm 0.08$ cm/μs in the following analysis.

TABLE 6.2: Summary of drift times measured with T1 and the obtained drift velocities at the four chamber rotations.

Angle [°]	Rising t_{FD} [ns]	Falling t_{FD} [ns]	Δt_{FD} [ns]	v_{drift} [cm/μs]
10	24.57 ± 0.18	117.88 ± 0.29	93.31 ± 0.34	5.36 ± 0.07
20	22.93 ± 0.13	123.82 ± 0.20	100.89 ± 0.23	4.96 ± 0.05
30	22.21 ± 0.14	124.79 ± 0.22	102.58 ± 0.26	4.87 ± 0.05
40	24.75 ± 0.24	130.90 ± 0.32	106.15 ± 0.40	4.71 ± 0.08

6.3.3 Reconstructing the tracklet with the μTPC fit

The essence of the μTPC technique lies in the following step. By knowing t_i and v_{drift} the coordinate transverse to the strip plane of each hit, corresponding to the drift distance, can be obtained with the $z - t$ calibration given by

$$z_i = t_i \times v_{drift} \tag{6.2}$$

The particle track can be reconstructed by fitting the distribution of the obtained drift distances z_i as a function of their respective strip positions, x_i, with a straight line. An example of such a distribution is shown in Figure 6.9. A local track reconstructed with this method will in the following be referred to as a tracklet.

The errors on z_i will be given by [42, 43]

$$\sigma_{z_i} = \sigma_{t_i} \times v_{drift} \tag{6.3}$$

where σ_{t_i} is the error on t_i obtained from the fit. The error on x_i is defined as [42, 43]

$$\sigma_{x_i} = \sqrt{(\sigma_x^{pitch})^2 + \left(\sigma_x^{pitch} \times \frac{\Sigma_i(q_i)}{q_i \times N}\right)^2} \tag{6.4}$$

where N is the number of strips in a cluster, q_i is the pulse-height measured at the ith strip and $\sigma_x^{pitch} = \text{pitch}/\sqrt{12}$.

The expression for σ_x^{pitch} is a commonly used expression describing the resolution of strip detectors. For tracks randomly aligned with respect to a strip, the difference between the measured and the true positions has a Gaussian distribution with a standard deviation given by [46]

$$\sigma^2 = \int_{-p/2}^{p/2} \frac{x^2}{p} dx = \frac{p^2}{12} \tag{6.5}$$

where p is the strip pitch. From this expression the RMS resolution will be given by the strip pitch divided by $\sqrt{12}$ [46]. Since the pitch of the T chambers is 400 μm we obtain $\sigma_x^{pitch} \approx 115$ μm.

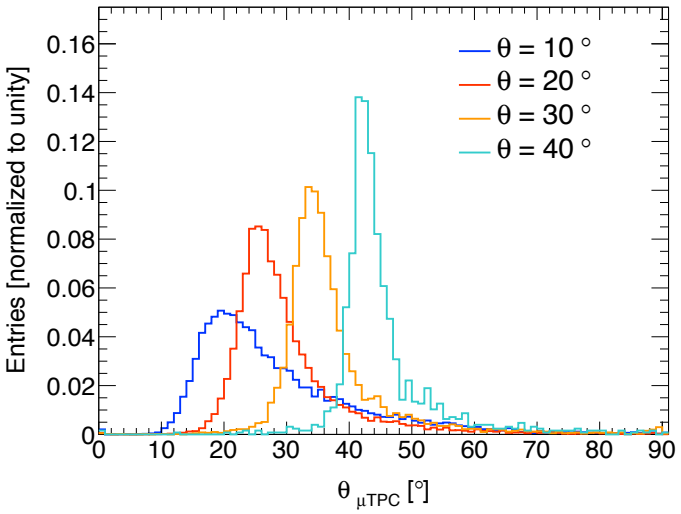

FIGURE 6.6: The angles reconstructed with the μTPC method in the T1 chamber for track inclinations at 10, 20, 30 and 40°.

6.3.4 Extracting spatial parameters

Given that a tracklet successfully has been reconstructed, the angle of incidence and position of the cluster can be calculated rather simply.

The reconstructed angle of the tracklet, $\theta_{\mu\text{TPC}}$, can be obtained with the relation [42–44],

$$\theta_{\mu\text{TPC}} = \arctan(1/\alpha) \tag{6.6}$$

where α is the slope of the μTPC fit. The distribution of reconstructed angles are shown in Figure 6.6. When examining the $\theta_{\mu\text{TPC}}$ distributions it becomes quite evident that the μTPC becomes more precise with larger track inclinations[4]. The explanation for this is in the following.

Consider the situation where a single electron is liberated in the drift gap. During its drift towards the mesh it will be subject to some diffusion in the plane perpendicular to the drift. Its position in x after the drift will therefore be displaced. Furthermore, because of the finite strip pitch, its position in x will be attributed to the position of the geometrical strip centre instead of its initial position.

If we apply this systematic effect to the case where multiple electrons are liberated in the drift gap by an incident particle, the lateral diffusion and the reality of a finite pitch will increase the likelihood of the electrons to be more spread out in x when they are detected. As a result, the slope of α will decrease when the μTPC fit is performed, and correspondingly will the reconstructed angle be larger. This systematic effect will

[4]The angular resolution obtainable with the μTPC and the associated uncertainties is an extensively studied subject, see [4, 47]

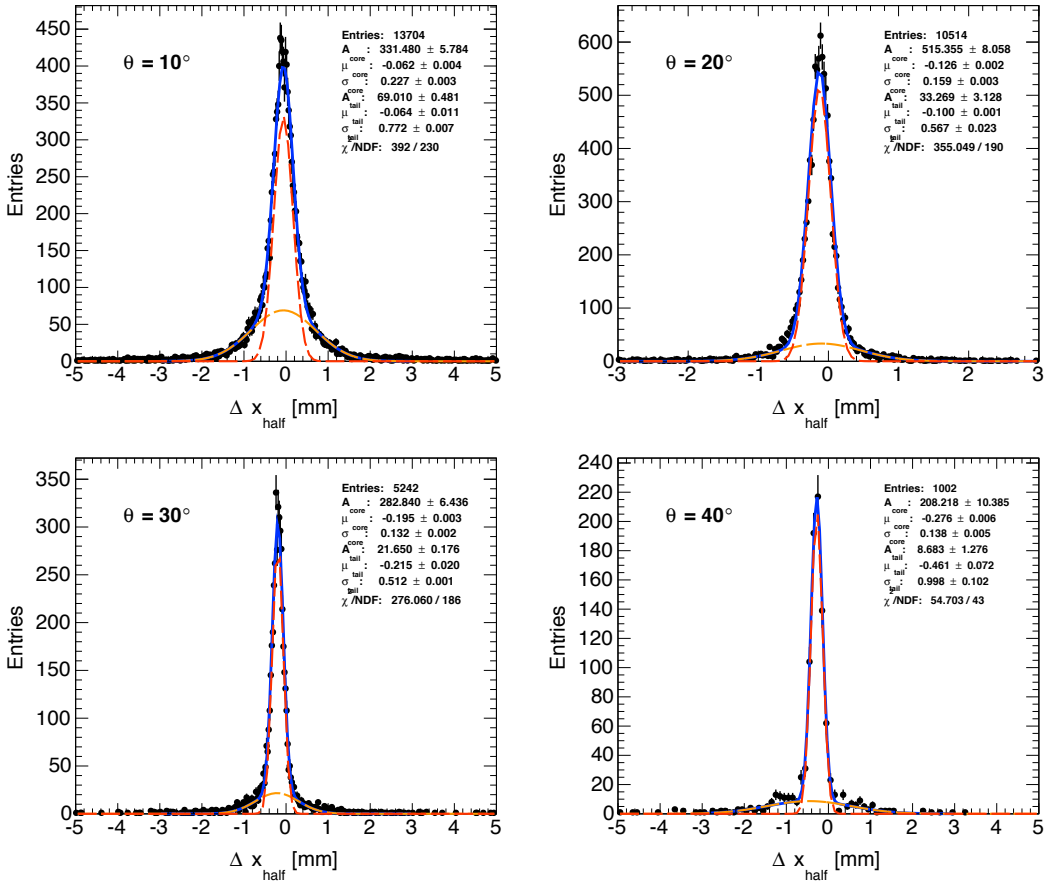

FIGURE 6.7: The residuals of the the cluster position measured with the μTPC method obtained with the T1 and T3 chamber for track inclinations at 10, 20, 30 and 40°.

be more pronounced at lower angles because the clusters will be smaller, meaning that the relative displacement in x is larger. This effect is expected to cancel out when several layers are used in a back-to-back configuration because the bias would happen in opposite directions.

For the position of the cluster the so-called x-half value, x_{half}, is used. This is defined as [42–44]

$$x_{half} = \frac{z_{half} - t_0 \times v_{drift}}{\alpha} + x_{first} \tag{6.7}$$

Here t_0 is the drift time measured for the first arriving hit, x_{first} is the position of the first strip in the cluster and z_{half} is half of the maximum drift path. The latter is set equal to 2.5 mm in the following.

6.3.5 Single-plane resolution

We now evaluate the spatial resolution obtainable with the μTPC technique. No attempt is done to do a full tracking with all the T chambers; instead the x_{half} residuals

TABLE 6.3: Summary of the single-plane spatial resolutions obtained with the μTPC method with the core Gaussian exclusively (x_{half} core) and with the weight of the core and tail Gaussians (x_{half} weight).

σ [μm]	10°	20°	30°	40°
x_{half} core	160 ± 2	112 ± 2	93.3 ± 1.4	97 ± 4
x_{half} weight	229 ± 5	144 ± 16	159.0 ± 1.5	121 ± 70

between two chambers facing the same direction are considered. This will in the following be presented with the T1 and T3 chamber, which were installed in the Freiburg frame facing the same direction (see Figure 5.3).

The obtained residuals will contain the convoluted resolutions of both of the chambers. If d denotes the distance between T1 and T3 and α denotes the beam divergence, the following relation will hold [42]

$$\sigma^2(X_1 - X_3) = \sigma^2(X_1) + \sigma^2(X_3) + d^2\sigma^2(\alpha) \tag{6.8}$$

Since $d \approx 20$ cm and $\sigma(\alpha) \approx 120$ μrad the beam diverges $d\sigma(\alpha) \approx 24$ μm, which we consider to be negligible since it is well below the pitch of the chambers. The last term in the above equation can therefore be ignored. Assuming that the T1 and T3 chambers have the same resolution, i.e. $\sigma^2(X_1) + \sigma^2(X_3) = 2\sigma^2(X)$, we obtain a single chamber spatial resolution of [42]

$$\sigma(X) = \frac{\sigma(X_1 - X_3)}{\sqrt{2}} \tag{6.9}$$

The obtained residual distributions for all four chambers rotations are presented in Figure 6.7. A very obvious characteristic of all the distributions is the bi-Gaussian line-shape containing both a core and tail, each represented by a single Gaussian. We attributed the tails to the bias related to the finite pitch mentioned in Section 6.3.4.

The single-plane resolution is determined by extracting the width of each distribution with a bi-Gaussian fit and dividing by $\sqrt{2}$. To account for the bi-Gaussian behaviour, the resolution is determined with two different approaches; 1) by considering the core Gaussian only and 2) by combining the width of the core and tail Gaussian by weighting with the height of each distribution. The results are summarized in Table 6.3. Like expected the method delivers the best resolution at the higher track inclinations.

6.4 The centroid method

We now turn to the charge centroid method. This technique is commonly used when determining the position of a cluster with a strip detector and is conceptually simpler than the μTPC method.

TABLE 6.4: Summary of the single-plane spatial resolution obtained with the charge centroid method.

σ [μm]	10°	20°	30°	40°
x_{cent}	148 ± 1	264 ± 2	412 ± 0	574 ± 20

As described in Chapter 2, the signals induced in the strips during the electron avalanche will be greatest in the strips of the closest approach. The pulse-heights will diminish proportionally with distance to the point of the avalanche. Therefore, if we again consider a single-coordinate detector where x_i and q_i denotes the position and pulse-height of the ith strip, the position of the cluster, x_{cent}, can be estimated by calculating the charge centroid of the cluster with the relation [15]

$$x_{cent} = \frac{\sum_i q_i x_i}{\sum_i q_i} \tag{6.10}$$

That is, x_{cent} is a space-point weighted with the measured pulse-heights. The resolution is to first order determined by the pitch of the strips and is given by Equation 6.5. This method is expected to loose precision with increasing cluster size since the charge spreads out over more strips and the position becomes less pinpointed. An example of a cluster having its position calculated with the centroid method is shown in Figure 6.9.

6.4.1 Single-plane resolution

To asses the spatial resolution obtainable with one detector plane the residuals between T1 and T3 are considered again. The residuals for the four angles are presented in Figure 6.8. We note that, as anticipated, the distributions have a smaller width at smaller track inclinations. We notice that the distributions obtained with the centroid follows the line-shape of a Gaussian nicely, which suggests that this method is less affected by systematic effects.

The procedure for obtaining the spatial resolution follows that described in Section 6.3.5. Only the core Gaussian is however used to extract the width of the distribution. The obtained results are summarized in Table 6.4. At 10° the resolution is comparable to that provided by the μTPC. As expected it deteriorates drastically with increasing track inclination.

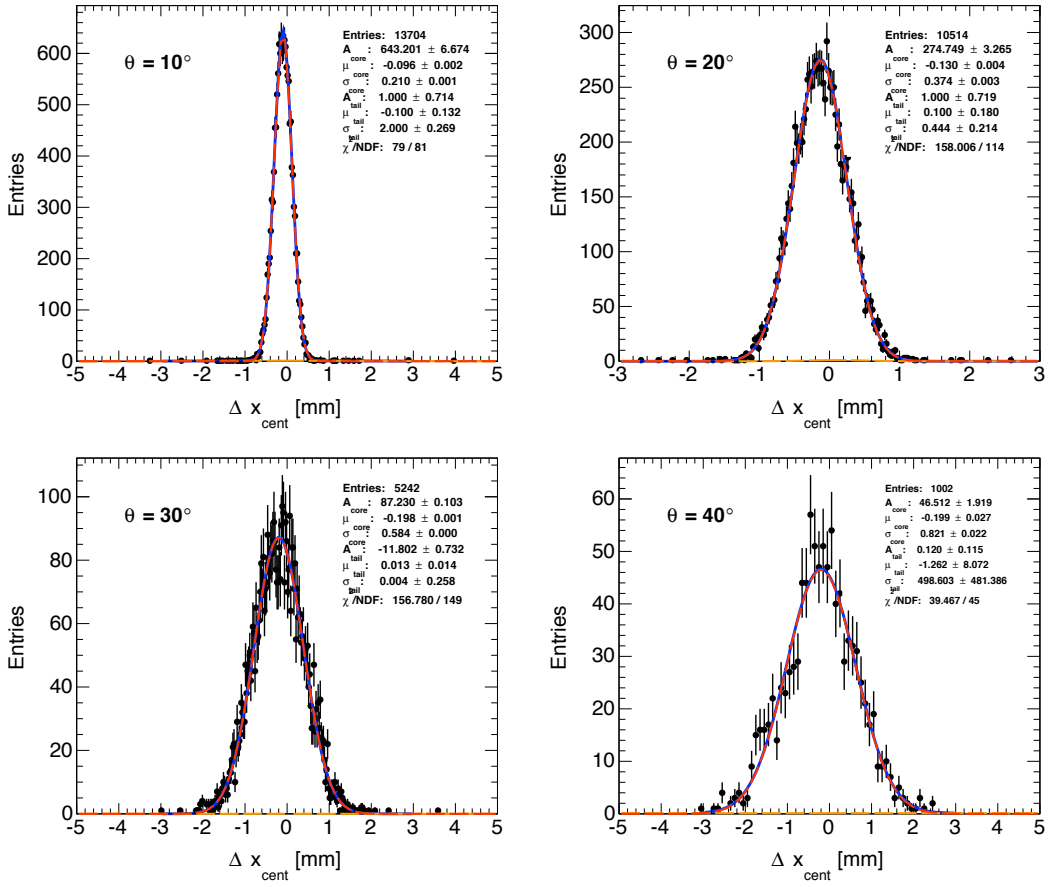

FIGURE 6.8: The residuals of the the cluster position measured with the charge-centroid obtained with the T1 and T3 chamber for track inclinations at 10, 20, 30 and 40°.

6.5 Combined spatial measurement

As just demonstrated, the μTPC technique provides exact measurements at higher track angles. Meanwhile, the charge centroid method performs slightly better at low angles. The anti-correlation between the two methods has been verified by several others [4, 42]. A weigthed average can therefore improve the resolution further [4].

A combination method was developed by the MAMMA community. The method contains a set of weights that favor the charge centroid in smaller clusters and the μTPC method in larger. The combined space-point x_{comb} is defined as [42]

$$x_{comb} = \frac{w_{half} x_{half} + w_{cent} x_{cent}}{w_{half} + w_{cent}} \tag{6.11}$$

where the weights w_{half} and w_{cent} are defined as [42]

$$w_{half} = \left(\frac{N}{N_{cut}} \right)^2 \tag{6.12}$$

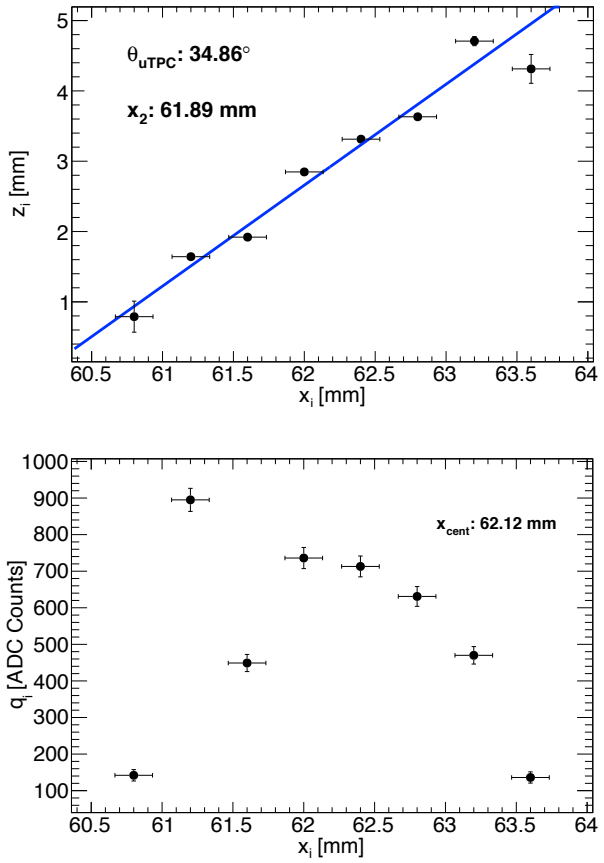

FIGURE 6.9: An example of a cluster recorded with a chamber inclination of 30°. In the top plot the cluster position and the angle of the track are reconstructed with the μTPC method. Note that the position x_{half} in this plot is named x_2. In the bottom plot the cluster position is calculated with the charge centroid.

$$w_{cent} = \left(\frac{N_{cut}}{N}\right)^2 \tag{6.13}$$

Here N is the number of strips in the cluster and N_{cut} is a cut value that must be specified. With the above weights the centroid will contribute the most for clusters with strips less than N_{cut} and vice versa. With the optimal value the resolution would be minimized over the full angular range. We will not treat the optimization of N_{cut}, but merely rely on the value used by the other groups in the community; $N_{cut} = 4$ [42].

6.5.1 Single-plane resolution

In order to asses the single-plane resolution obtained with the combination method, the residuals between the T1 and T3 chambers are considered again. The residuals are shown in Figure 6.10. Since the tails from the μTPC method propagate to the combined

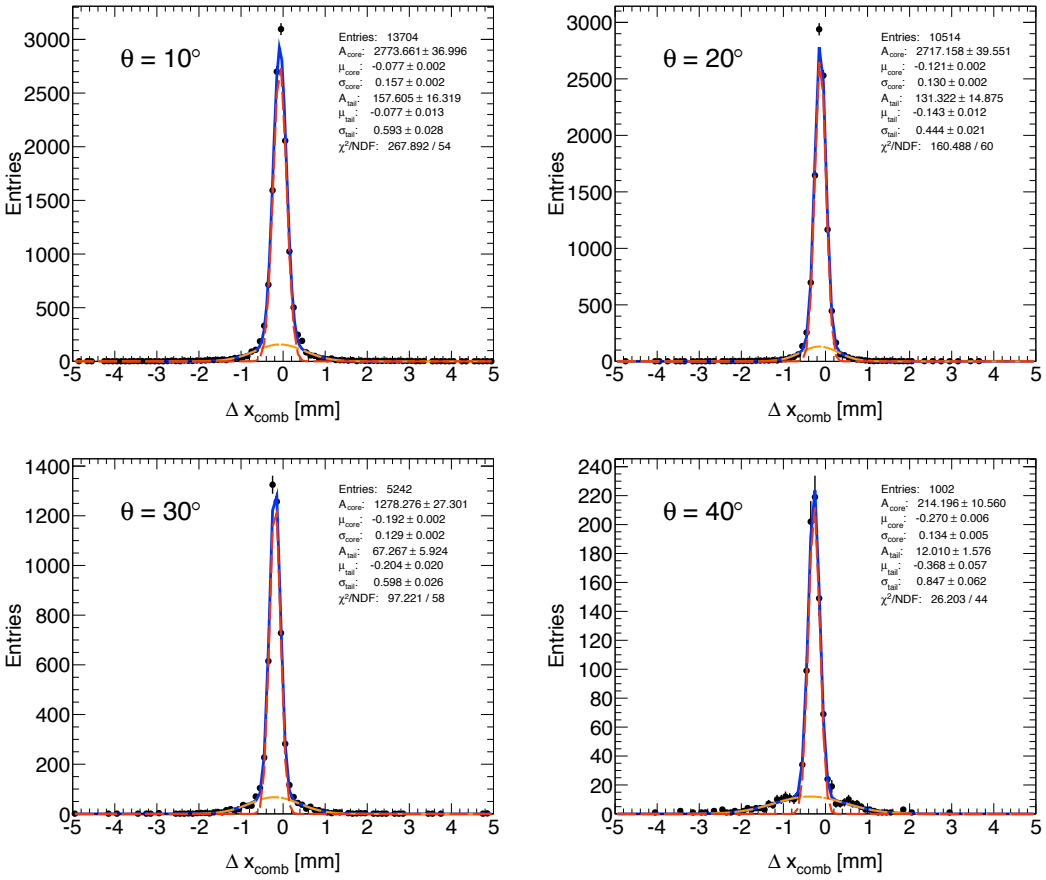

FIGURE 6.10: The residuals obtained with x_{comb} for track inclinations at 10, 20, 30 and 40°.

TABLE 6.5: Summary of the single-plane spatial resolutions obtained with the combined μTPC and charge centroid method.

σ [μm]	10°	20°	30°	40°
x_{comb}	111 ± 11	92 ± 1	91 ± 1	95 ± 4

measurement, the resolutions are extracted with a bi-Gaussian fit. The results obtained with the combination method are summarized in Table 6.5. These results are calculated with the core Gaussian only, since we assess that the tails have been broadened artificially by the finite-pitch bias mentioned in Section 6.3.4. We see that there is no longer any strong angular dependence on the resolution. Furthermore, the obtained single-plane resolution in the full angular range is very close to or below 100 μm.

6.6 Discussion

Certain factors in our selection have undoubtedly biased our results. For example, the bias mentioned in Section 6.3.4 related to the finite pitch is expected to be more significant for smaller clusters. Two aspects in our selection limit the cluster size; the rejection of clusters with holes and the suppression of strips with small pulse-heights. Both requirements are anticipated to affect the clusters at larger track inclinations the most. Because of this, the events measured at the largest inclinations are likely to have been affected more by the finite-pitch bias. This can explain why the tails in the μTPC residuals do not decrease with track inclination, which otherwise was expected.

Chambers facing the same direction were used in the analysis that produced the official results for the NSW technical design report [42, 43]. Since we (shortly) will compare our results with these, we decided to use the same chamber configuration. We will in this comparison ignore the contribution from the tails and only consider the resolution extracted with the core Gaussian.

One may be concerned whether the finite-pitch bias will limit the usability of the μTPC method. We again underline that the tails in the residuals, caused by this bias, occur because we consider chambers facing the same direction. The individual MicroMegas detector planes in the NSW will be installed back-to-back; the finite-pitch bias will thus cancel out and should hence not be a source of concern.

Instead of the method outlined above, the single-plane spatial resolution can be determined by reconstructing a full track with the reference chambers (a subset of the T chambers), and evaluating the residuals between the track and the reconstructed position of the cluster. This method would account for the beam divergence. However, like explained in Section 6.3.5, this is assumed to be negligible. The tracking method would also account for the beam deflection caused by multiple scattering in the detector material. Since the material between T1 and T3 reduces to three PCBs that each have a thickness of < 500 μm and the radiation length of the FR4 is relatively high[5], we assume that this contribution is small as well. Therefore, we assess that the benefits of the tracking method are limited and that our procedure provides comparable results.

6.7 Conclusion

The single-plane resolution obtained with the μTPC, the charge centroid and the combination methods are summarized in Table 6.6 and visualized in Figure 6.11. In Figure 6.12 the combined results of the MAMMA Collaboration (presented in the NSW technical design report) are shown. The agreement between the two sets of results is very

[5]The radiation length of FR4 is often approximated with that of carbon, which is 42.70 g cm^{-2} [1]

TABLE 6.6: Summary of the single-plane spatial resolutions obtained with the μTPC method (both with core Gaussian exclusively and the weight of the core and tail), the charge centroid method and the combined method.

σ [μm]	10°	20°	30°	40°
x_{half} core	160 ± 2	112 ± 2	93.3 ± 1.4	97 ± 4
x_{half} weight	229 ± 5	144 ± 16	159.0 ± 1.5	121 ± 70
x_{cent}	148 ± 1	264 ± 2	412 ± 0	574 ± 20
x_{comb}	111 ± 11	92 ± 1	91 ± 1	95 ± 4

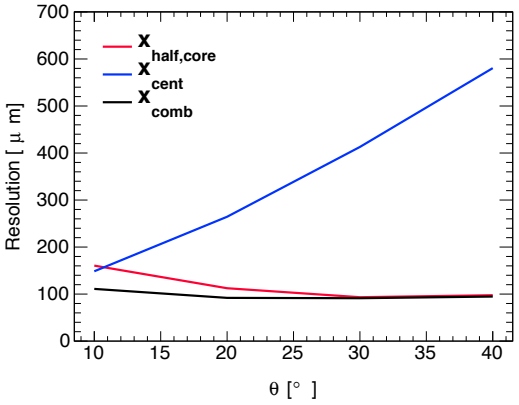

FIGURE 6.11: Single-plane spatial resolution obtained with the μTPC method (with the core Gaussian exclusively) the centroid method and the combined measurement.

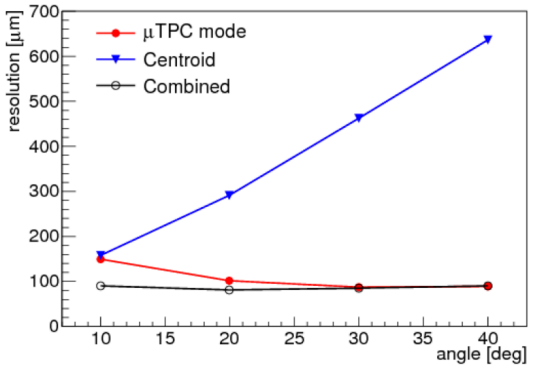

FIGURE 6.12: Single-plane spatial resolution presented by the MAMMA Collaboration in the NSW TDR [4].

good. With the novel combination technique the single-plane resolution is below, or very close to, 100 μm in the full angular range.

From the above results we conclude that the MicroMegas technology with a combination of the μTPC technique and the centroid method is able to deliver a spatial resolution that is adequate for the NSW. By optimizing the combination technique the

resolution could possibly be improved further. With this confirmation one item in the list of milestones of the MAMMA Collaboration is fulfilled.

Chapter 7

The 1 x 1.2 m^2 Chamber

As a step towards developing the full-sized MicroMegas prototype requested in the milestones, a chamber with the dimensions 1×1.2 m^2 was constructed. The primary purposes of constructing this intermediate-sized Large 1 (L1) chamber were to probe and develop production techniques for large-area detectors, to implement and asses the functionality of a floating mesh and to examine the response of 1 m long strips, which was untested at the time. The early completion date enabled it to be installed in the test-beam campaign, which provided a convenient opportunity to directly compare its behaviour to that of bulk chambers. The work with the L1 chamber constitutes the very first experience obtained with large-area MicroMegas detectors.

In this chapter an extract of functionality and performance aspects that are directly related to the design differences of bulk and non-bulk chambers are investigated. In Section 7.1 the layout of the L1 chamber will be reviewed briefly. Details on the detector mechanics and the production will be deferred to Chapter 8 since these aspects will be more interesting and relevant in the context of the full-sized prototype. In Section 7.3 and 7.4 the dependence of the gain on the applied high-voltage and the efficiency is studied and compared to that from the bulk chambers. The latter comparison is particularly important for understanding the behaviour of large-area detectors. Furthermore, the experience obtained from these studies will be used in the operation and design of the full-sized prototype presented in Chapter 8.

7.1 Detector layout and production

L1 was designed to contain 2048 strips in x with a pitch and width of 450 μm and 300 μm, respectively. It was composed of two panels: a so-called drift panel, which carried the drift electrode and the mesh, and a read-out panel onto which the pillars and strips were mounted. The base of each panel was a stiffening structure made from

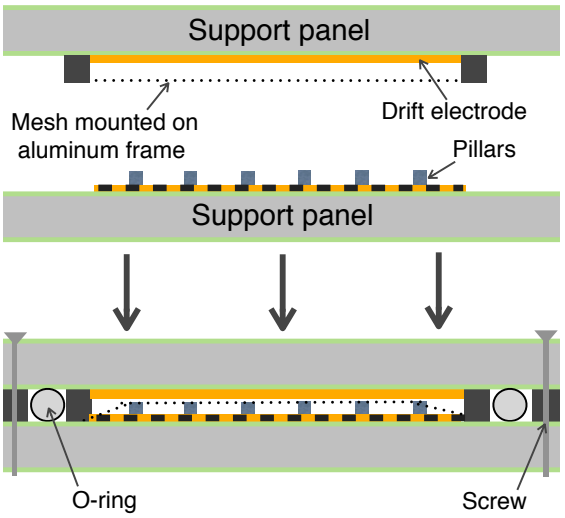

FIGURE 7.1: Illustration of the principle of the floating mesh (not to scale). In the top drawing (above the arrows) the chamber is open. In the bottom the chamber is closed and the floating mesh is stretched over the pillars.

an aluminum frame filled with aluminum honeycomb. The surfaces of the panels were covered with 0.5 mm thick FR4 skin, the outer surfaces being copper clad to provide RF shielding [48]. Details on the mechanical accuracy will be given in the context of the full-sized prototype.

The construction of L1 involved the first implementation of a floating mesh in a large-area detector. The decision to develop this technique relied more on practical considerations rather than aspects related to physics performance. Firstly, standard equipment for PCB manufacturing is not tailored for the production of very large bulks and it would hence be cumbersome to delegate the production of major quantities to industrial partners. Additionally, large-area detectors face a high risk of being contaminated by dust from external sources. A floating mesh offers the convenient feature of the ability to remove it and clean the underlying surface.

The principle of the floating mesh is illustrated in Figure 7.1. A woven inox mesh with a wire diameter and density of 30 μm and 325 wires/inch, respectively, was stretched over aluminum bars mounted at the periphery of the drift electrode. The height of these bars defined the size of the drift region; the nominal 5 mm were chosen. When closing the chamber by joining the two panels together, the floating mesh was suspended over the pillars in the active area. Proper and uniform attachment was expected to happen automatically when applying high-voltage; the electrostatic force created in the amplification region was anticipated to be powerful enough to pull it towards the pillars.

The drift electrode and read-out surface were both composed from a set of PCBs. These were separated electrically and thus operated independently. All four PCBs were

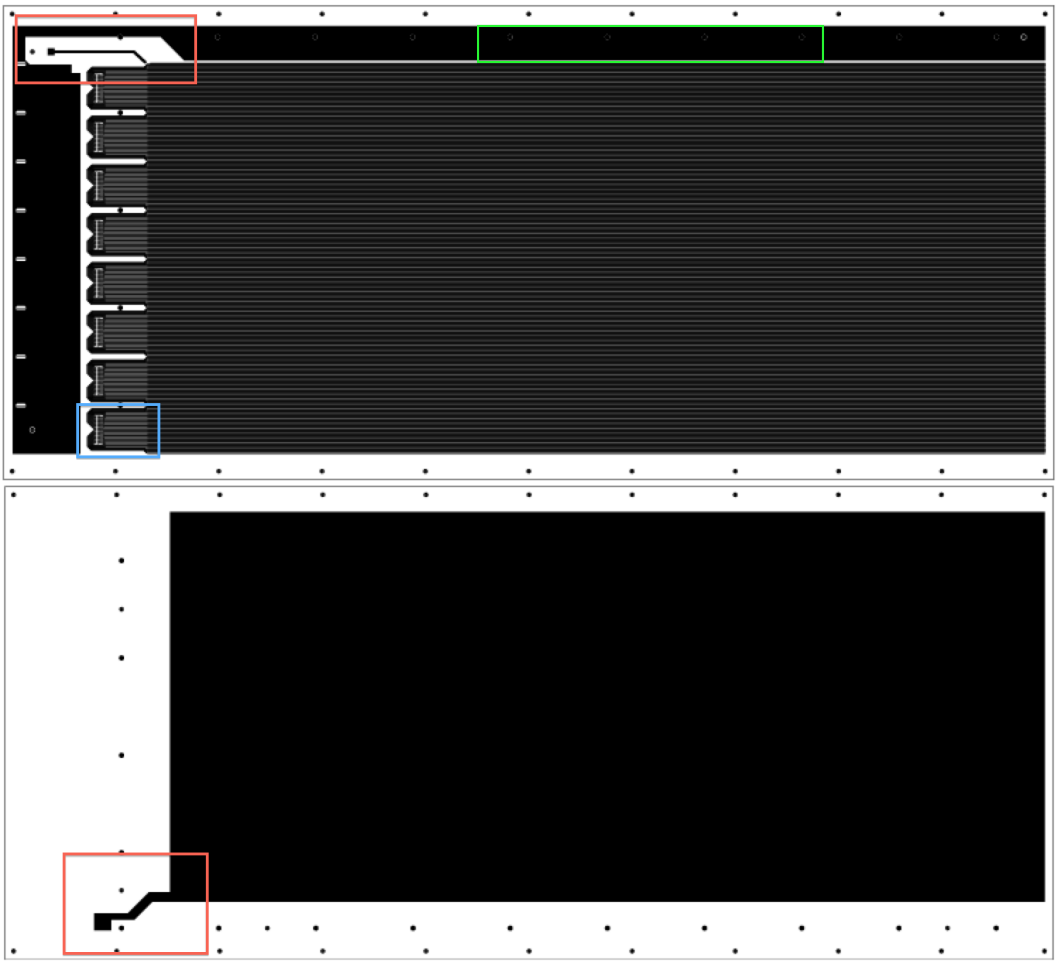

FIGURE 7.2: Drawings of the read-out (top) and drift (bottom) PCBs used to construct L1. The black areas represent a copper surface.

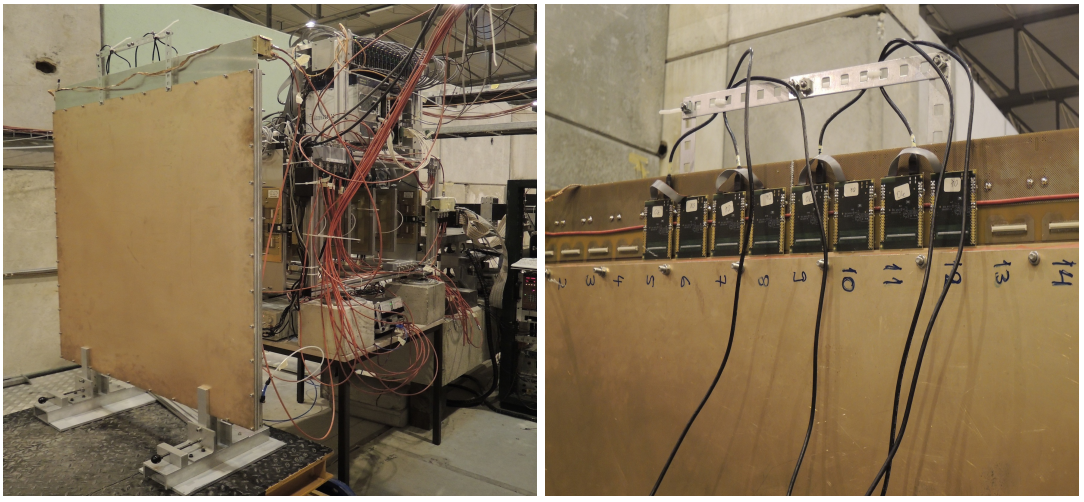

FIGURE 7.3: Left: The L1 chamber installed in the test-beam setup in front of the Freiburg frame. Right: 8 APVs are installed on the central part of L1.

0.5×0.6 m^2 and produced by the CERN PCB-workshop, the resistive strips made with deposition of resistive paste.

The two PCBs needed for each electrode were mirrored with respect to each other. A continuous surface for each electrode was made by joining them together. The layout of a drift and read-out PCB is shown in Figure 7.2. Black surfaces represent copper-clad areas. The area on the read-out PCB marked with blue designates the routing of the read-out strips to the Panasonic connectors where the on-detector electronics was mounted. The electrical connections to the electrodes, both the resistive strips and the drift electrode, are marked with red frames. High-voltage filters and SHV connectors were mounted onto these. The dots at the edges were used for aligning the PCBs in the construction process.

Detector ground was defined as the outer surface of L1. The two detector panels were held together by conducting $\varnothing$ 6 mm screws penetrating the edge of the PCBs designated with the green frame in Figure 7.2. This edge was set to ground potential via the contact to the screws, and the mesh was set to ground potential through direct contact with this edge after the assembly. All on-detector electronics (APV hybrids) was correspondingly set to ground potential by being mounted on this edge.

High-voltage RC-filters were applied to the electrodes after the assembly. To the drift electrode a 1 MΩ resistor in serial and a 4.7 nF capacitor in parallel. The filters at the resistive strips were the same, but a smaller resistor of 100 kΩ was used instead to minimize the charging-up time in the occurrence of a discharge. Gas was supplied through an inlet in one corner of the chamber and outlet in the diagonal corner. To ensure gas-tightness, the chamber was sealed with a 6 mm O-ring.

7.2 Experimental setup

After having performed tests in the laboratory and assured the basic functionality, L1 was installed in the test-beam setup $\approx$ 40 cm upstream of the Freiburg frame. It was equipped with 8 APVs at a time, which were moved around according to which area on L1 that was being radiated. A hit profile measured with L1 operated at 580 V for one test-beam run is shown in Figure 7.4. The profile has an extent of $\approx$ 1 cm, which corresponds to the width of the scintillator finger.

In the following sections the clusterization algorithm from Chapter 6 is used. Since we exclusively consider perpendicular tracks, the cluster position is calculated with the centroid method only.

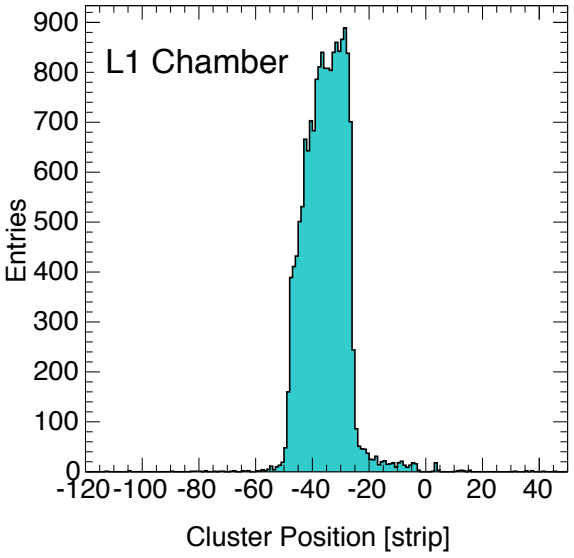

FIGURE 7.4: The hit profile measured with L1 in test-beam. The profile of the beam is evident.

7.3 Gain dependence on applied voltage

A set of test-beam runs were identified in which a high-voltage scan was performed with L1 in the range 530 - 580 V in steps of 10 V. In these runs the position of the beam was close to the edge of L1 at the opposite end of the read-out. To compare the response to that from a bulk chamber, a set of test-beam runs recorded with the T2 chamber operated at 480 - 510 V were identified as well.

The spectra of integrated cluster charge for single-cluster events measured with L1 and T2 are shown in Figure 7.5 and 7.6. The distributions obtained at all high-voltage values resemble the Landau function, which was expected from the theory discussed in Chapter 2. To evaluate the line-shape and extract the MPV of the distributions, a Landau fit is imposed. Although we do not expect the shape of the Landau function to mimic the spectra perfectly it is sufficient for the present purpose; the obtained MPV-values will in the following be used as an estimator of the gain.

The MPV distributions obtained from the L1 and T2 spectra are presented in Figure 7.7. Errors are reported as the MPV uncertainty extracted from the fits. The curve representing the T2 chamber is consistent with a straight line. For L1 the curve behaves diffrently; all data points are consistent with a linear trend, but the slope of this differs from the first three data points and the remaining. This feature is suspected to be a result of a truncation of the charge spectra measured at the lower high-voltage values. This is discussed in Section 7.3.1.

The curve representing T2 suggests that the gain is exponentially dependent on the

applied high-voltage. An exponential trend is likewise present in the L1 data points that are not expected to be biased by truncation. Thus, Figure 7.5 indicates that the gain in both chambers depends exponentially on the electric field strength. This is in agreement with the predictions from the Diethorn approximation (mentioned in Chapter 2) and substantiates the assumption that L1 obeys the physical principles governing the proportional counter.

An essential point concerning non-bulk MicroMegas detectors is implied by the fairly obvious discrepancy in the response from the T2 and L1 chamber; the charge yield from L1 is considerably lower than from T2, having a constant offset of ≈ 60 V. This feature is related to their different construction. The size of the amplification region in bulks is smaller than the nominal height of the pillars because the mesh is slightly embedded in them. Conversely, a floating mesh rests directly on the pillars, and the amplification region is hence larger. Therefore, the magnitude of the electric field in amplification region for a given high-voltage value is greater in a bulk chamber and likewise the gain.

The size of the amplification region in the two chamber types can be estimated with the above knowledge and Figure 7.7. The charge yield of T2 at 510 V corresponds to that of L1 operated at 570 V. Assuming the amplification region of L1 is 128 μm, the electric field strength at 570 V is ≈ 45 kV/cm. This particular field strength can only be obtained at 510 V if the amplification region in the bulk has the specific size $\approx$113 μm.

7.3.1 Discussion

The curves presented in Figure 7.7 should be interpreted with some caution. In the charge spectra measured with L1 the distributions obtained at the lowest high-voltage values are rather narrow. It is likely that this is not a physical feature, but is a result of the capacity of the experimental equipment and the cluster selection.

The dynamic range of the APV hybrid is limited; events containing a high number of ionizations may saturate it. Because our cluster selection rejects all clusters with just a single strip going into overflow, the obtained charge distributions may have been shifted towards the lower end of the spectrum. This effect is in particular expected to influence the distributions measured at the largest high-voltage values.

The same limitations apply to the low end of the charge spectrum. The smallest detectable signal is constrained by the pedestal threshold and by the cluster selection, the latter by requiring a minimum charge value in each strip of a cluster. Such constraints would truncate the distributions at the low end of the spectra and shift the distributions toward higher values.

The above constraints can explain the two-tiered behaviour of the L1 curve observed in Figure 7.7. At the lowest high-voltage values the charge yield is modest; as a result the

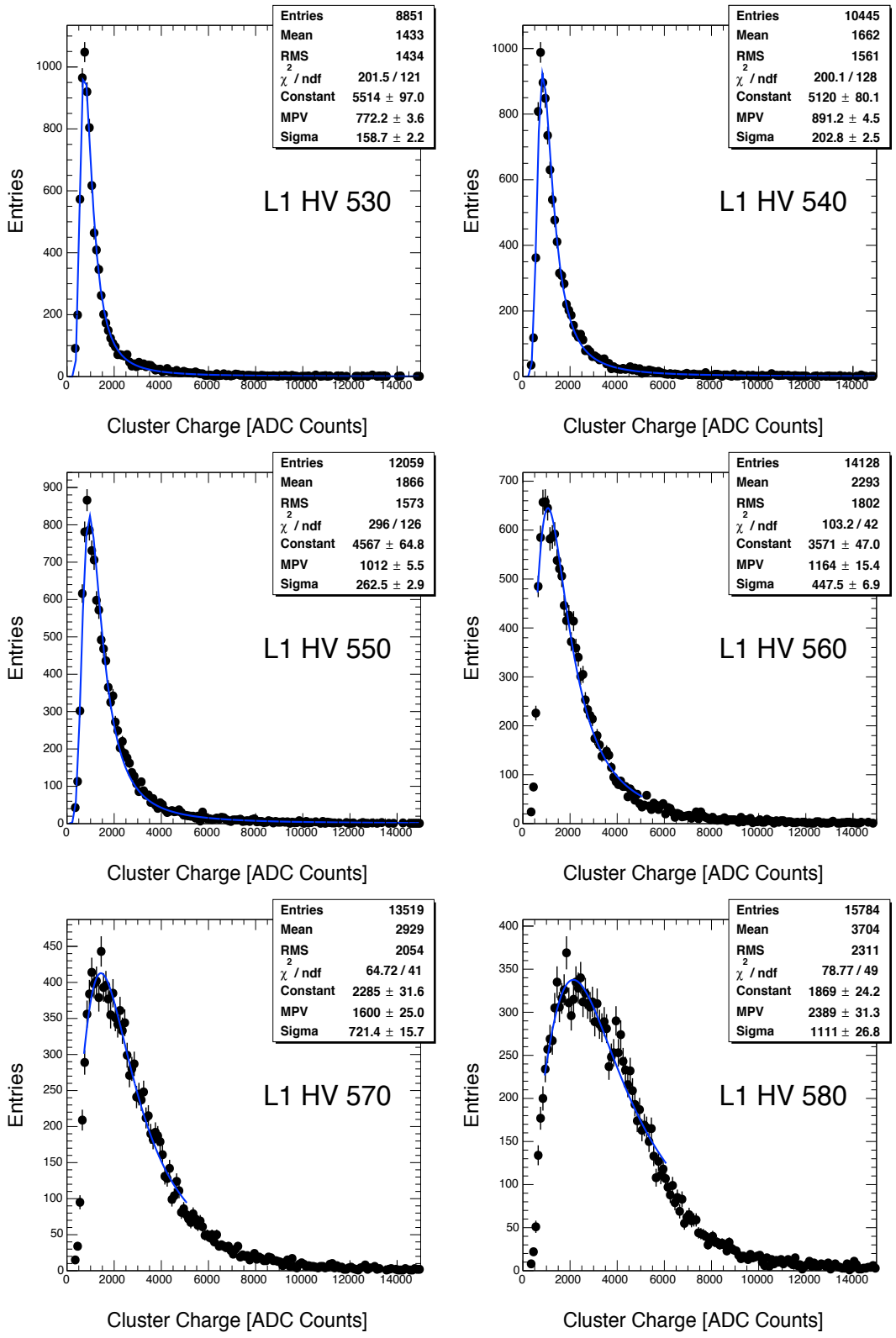

FIGURE 7.5: The distributions of integrated cluster charge for single-cluster events measured with L1 at six high-voltage values.

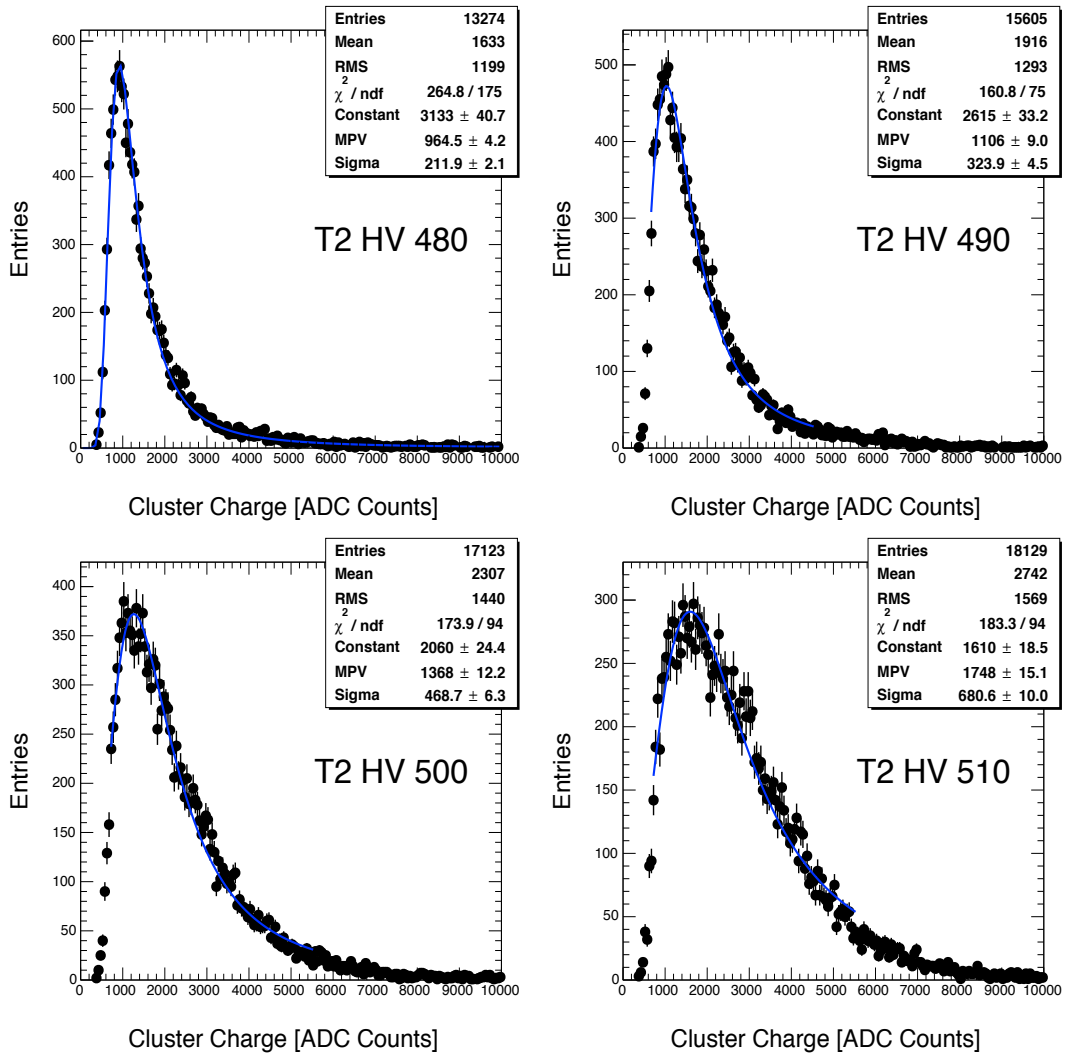

FIGURE 7.6: The distributions of integrated cluster charge for single-cluster events measured with the T2 chamber in the high-voltage scan.

charge spectra are truncated and the obtained MPV-values shifted upwards. The charge threshold in the strip selection could in principle be lowered, however, as seen in Figure 7.10 this would allow noise to propagate to the L1 data. Hence, the limited capacity of the test-beam setup and sample selection does not allow for an optimal treatment of all L1 runs. Work needs to be done in order to better select the low pulse-heights.

7.4 Efficiency

The detection efficiency is the probability for the detector to provide a signal upon the incidence of radiation, i.e. the fraction of registered events n to the total number of impinging events n_{total} [15]

$$\mathcal{E} = \frac{n}{n_{total}} \tag{7.1}$$

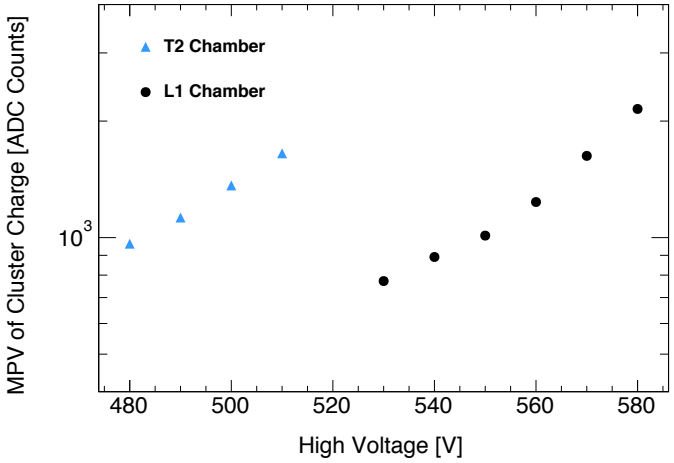

FIGURE 7.7: The MPV of the Landau fit imposed to the distributions of integrated cluster charge measured with the T2 and L1 chambers in high-voltage scans.

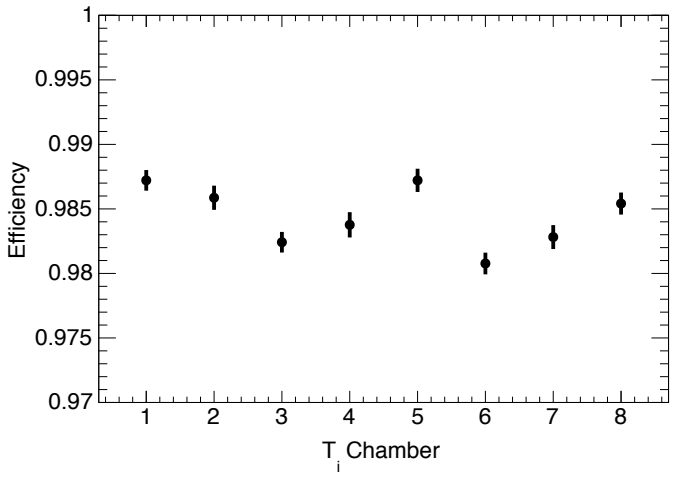

FIGURE 7.8: The efficiency of the T chambers measured with test-beam data.

The error on the detection efficiency will in the following be given as binomial errors [49]

$$\sigma_{\mathcal{E}} = \sqrt{\frac{\mathcal{E}(1-\mathcal{E})}{n}} \tag{7.2}$$

To measure the efficiency of the T chambers, a test-beam run was selected where the incidence of the beam was perpendicular to the chambers. All chambers were operated with 500 V. In the following n_{total} is defined as the fraction of events where a single cluster was measured in 7 of the T chambers. The efficiency of the 8th chamber (T_i) is measured with respect to that. All 7 T chambers are used as reference to reduce the risk of counting fake events.

The T chamber efficiencies are summarized in Figure 7.8. In all chambers the inefficiency is less than 2%. Part of this inefficiency can be attributed to the fraction

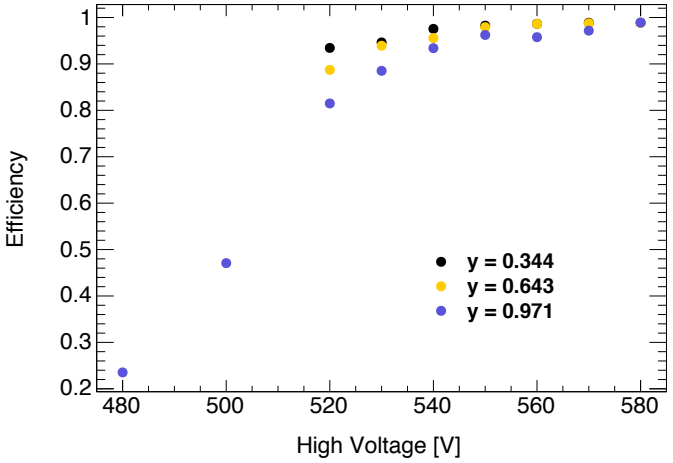

FIGURE 7.9: The efficiency of the L1 chamber measured with test-beam data at three different positions on the chamber.

of the active area covered by pillars; given their diameter and spacing of 300 μm and 5 mm, respectively, the dead area is $\approx 1.1\%$.

The efficiency of the L1 chamber is measured with respect to the first four T chambers, defined as the fraction of events where one cluster is measured. The choise of exactly four reference chambers is based on a compromise between avoiding counting fake events and maintaining sample size. For this measurement three test-beam runs were selected. In each run the position of the beam was changed along the strip direction. A high-voltage scan was performed at each of these positions.

The efficiency of L1 as a function of the applied high-voltage is presented in Figure 7.9. The y-direction is defined to be along the strips, $y = 0.344$ m being close to the edge of L1 in the opposite end of the read-out electronics and $y = 0.971$ m being approximately at the middle of the chamber. The curves corresponding to the positions closest to edge are only available from 520 V and up. At these two positions the efficiency behaves similarly; a 98% efficiency, comparable to that from the T chambers, is achieved at 550 V. This is consistent with the experience from Section 7.3 where a $\approx$ 60 V offset was found.

The efficiency measured at the middle of the chamber is overall lower than compared to at the edge. The reason for this was not fully comprehended until the full-sized prototype was constructed and a similar (but more pronounced) effect was observed. The combination of over-pressure in the chamber (a few mbar) and the large surface area caused the outer surfaces of L1 to bulge outwards slightly. It is probable that the floating mesh failed to conform to the curvature of the read-out panel, in which case the amplification region could have failed to establish properly, the net effect being a reduction in gain. At 580 V the efficiency at the central part of L1 becomes comparable

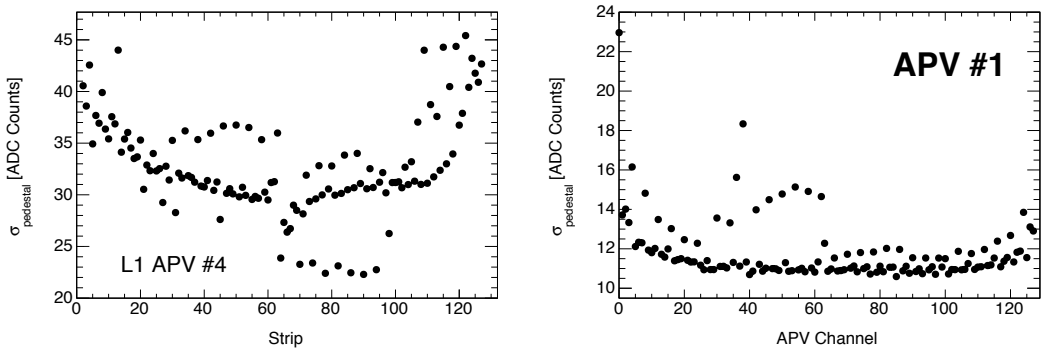

FIGURE 7.10: The pedestal standard deviation obtained from the APV hybrids mounted on L1 (left) (at the strips corresponding to the area being radiated by the beam) and on the T1 chamber (right). Distributions for the remaining T chambers can be found in Appendix B.

to the two other positions.

7.4.1 Discussion

Related to the discussion in Section 7.3; the efficiency measurements may have been influenced by the cluster selection and experimental equipment by suppressing events collected at either low or high voltages. Furthermore, the efficiency could have been increased artificially by counting fake events caused by noise. This could be avoided by reconstructing a full track from the reference chambers, extrapolating it to the chamber in question and confirm that the event was physical by comparing the position of the track to the reconstructed cluster. However, the benefits from this method are assessed to be minimal in our setup; with the given charge threshold for each strip the amount of noise propagating to the data will be negligible. Examples of the pedestal standard deviations are shown in Figure 7.10 (similar plots for remaining T chambers are in Appendix B).

7.5 Conclusion

The test-beam campaign allowed for a direct comparison of the performance of the L1 chamber to that of the bulk T chambers. These studies constituted the very first experience with large-area MicroMegas detectors and highlighted essential characteristics: the gas gain and efficiency at a given high-voltage value is substantially lower in a floating mesh detector than in a bulk chamber. This knowledge will be used extensively in the

future operation of floating mesh detectors. The experience with L1 furthermore provided valuable information about the detector layout and construction, which will lay the ground for the production of its successor, the full-sized prototype L2.

Chapter 8

The 1 x 2.4 m^2 Chamber

One of the primary milestones of the MAMMA Collaboration was to demonstrate that a full-sized prototype with at least the dimensions 1×2 m^2 could be made with adequate mechanical precision. This particular size was motivated by the layout of the large sectors in the NSW (shown in Figure 4.16), which will carry MicroMegas detectors that are up to 2.2 m wide.

The basic performance of a large-area detector carrying a floating mesh was compared to bulk chambers with L1 in test-beam. In this chapter the focus is on another aspect; the impact of the mechanical precision and the layout on the response of the detector. In Section 8.1 the layout, production and assembly of L2 is reviewed. In Section 8.4 the uniformity of L2 is tested. In Section 8.5 we probe whether the floating mesh works when part of the detector is switched off. The study of the dependence of the gain on the field strength is described in Section 8.6. All these studies constitute important steps towards understanding the behaviour of the detectors that ultimately will be implemented in the NSW.

8.1 Detector production

8.1.1 Layout

A 3D sketch of the complete L2 chamber is shown in Figure 8.1. It had the outer dimensions 1×2.4 m^2. Like L1 it consisted of two panels; a drift panel carrying the drift electrode and the floating mesh, and a read-out panel onto which the read-out structure (pillars and strips) were mounted. The base of each panel was a stiffening structure consisting of an aluminum frame filled with honeycomb and spacers. The surfaces were clad with FR4. A gas distribution system was incorporated into the cavities of the aluminum bars in the drift panel. A sketch of a slice through the panels is shown in

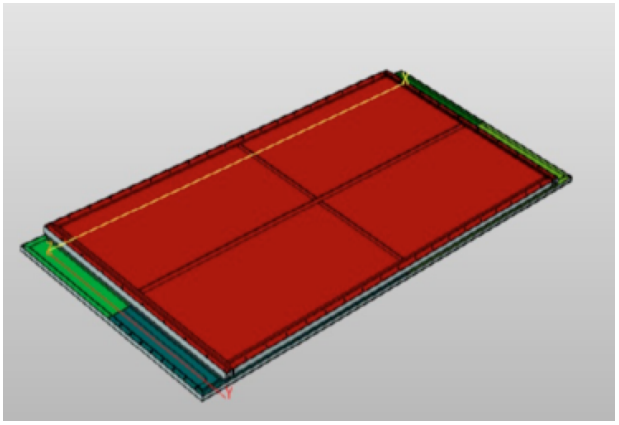

FIGURE 8.1: 3D view of the assembled L2. The drift panel carrying the floating mesh (red) is mounted on top of the read-out panel (green)

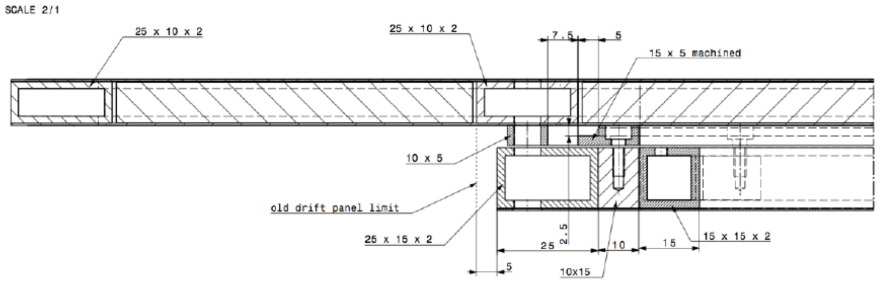

FIGURE 8.2: Cross-sectional view of the frames of the read-out panels. The profiles along the read-out side is shown with the gas channel. The mesh frame is also shown [4].

Figure 8.2.

Each electrode was made from four PCBs similar to those used for L1. To create a continuous surface they were glued onto their respective panel adjacently. L2 was hence electrically segmented into quarters that had to be operated independently. A naming convention was made such that the detector in longitudinal direction was separated into a side A and B, both with a left (L) and right (R) side. Side A and B each carried 2048 strips with a pitch of 450 μm in the longitudinal direction.

8.1.2 Production

The 8 PCBs needed for the two electrodes were produced by the CERN PCB workshop. The resistive strips were made with the screen printing technique by at an external partner[1].

All construction involving the detector mechanics was conducted on a granite table. This facility was needed to obtain the required precision in the planarity of the individual

[1]Charbonney: `http://www.charbonney.ch/`

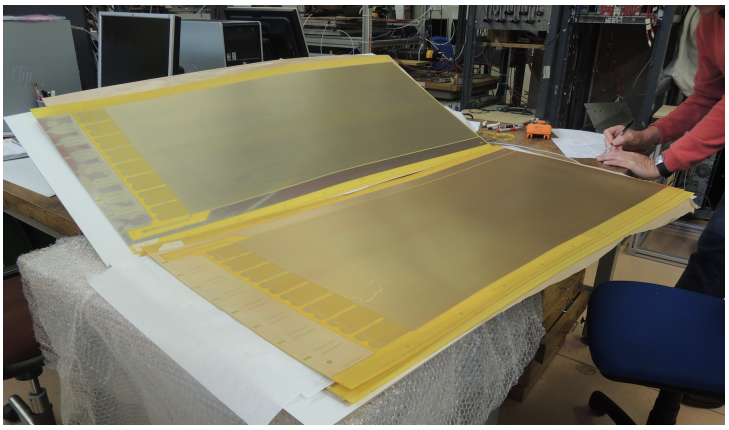

FIGURE 8.3: Two of the read-out PCBs before screenprinting of the resistive strips and the construction of the pillars.

detector parts. A novel vacuum sucking system was developed to optimize the planarity of the surfaces being glued. This system consisted of a thin mesh fabric covered by a 175 μm thick mylar foil stretched over the table with pump connectors inserted. The volume under the foil was sealed by taping its edges to the table. Striations were cut in the foil to serve as suction windows. The sheet to be glued was placed on the foil. When switching on the pump it was kept in place and conformed to the flatness of the table.

The procedures used to construct the stiffening panels are displayed in Figure 8.4. At first the 0.5 mm thick FR4 skin constituting the panel surface was placed on the granite table. A frame consisting of machined aluminium bars was glued close to the edges of the skin with Araldite®. The cavity spanned by the frame was filled with 9 mm cell sized aluminium honeycomb, which was glued to the FR4 skin. Plastic spacers were distributed evenly in the honeycomb and also placed external to the aluminum frame in order to fix the thickness of the panel. A panel was closed by gluing an identical sheet of FR4 onto the open surface. Loads were placed on the panel while the adhesive was drying; this extra force caused the downward facing panel to conform to the flatness of the table. A panel was left to dry in this configuration for 24 hours.

The PCB quartets were now glued onto their respective panel. The PCBs were places in the correct configuration with the active side facing downwards and were retained in the correct configuration with the vacuum sucking system. Glue was distributed on the backside of the PCBs, and the support panel was placed on top. The structure was left to dry under vacuum for 24 hours. The complete drift and read-out panels are displayed in Figure 8.5.

Any mechanical deformation of either of the panels was expected to influence the performance of the detector. Deformations in the read-out surface would however be more severe since this directly could disturb the field in the amplification region. The

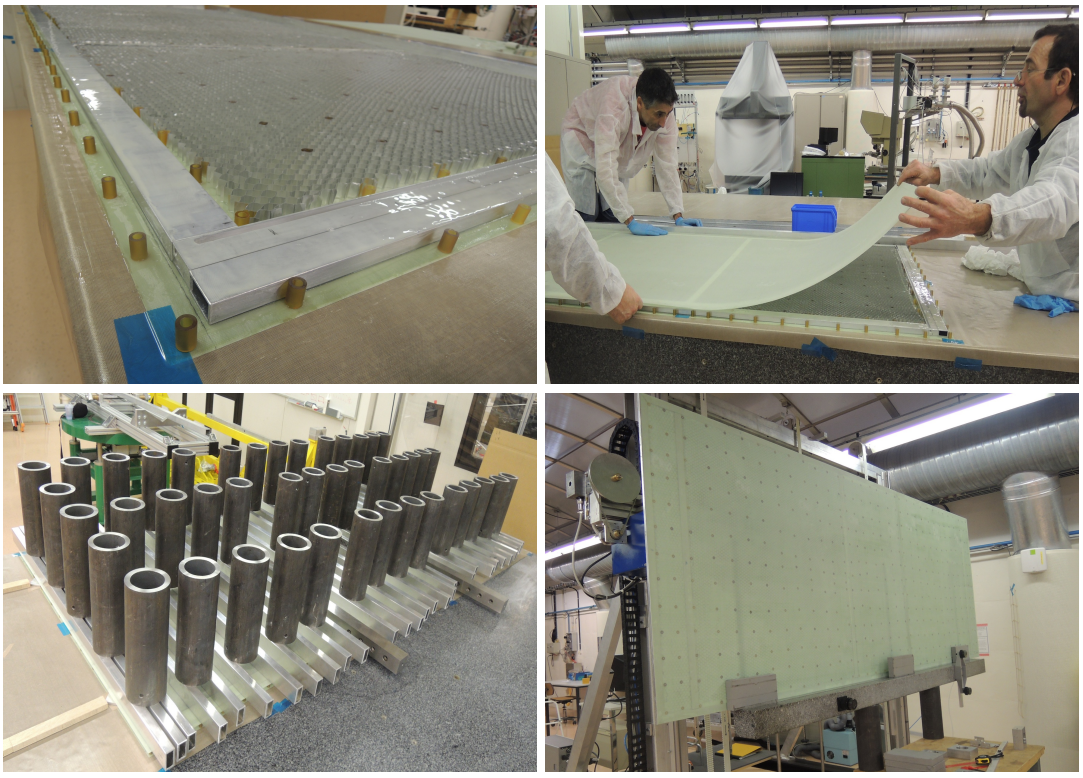

FIGURE 8.4: Top left: The aluminum frame, honeycomb and spacers are glued to the FR4 skin. Top right: The open panel surface is closed with another FR4 skin. Bottom left: A panel is left to dry under loads such that the downward surface conforms to the flatness of the granite table. Bottom right: The planarity of a complete panel is measured with the laser interferometer.

planarity of the two complete panels was therefore measured with a laser interferometer from the NA62 laboratory. This device provided distance measurements with a resolution of a few μm after having been calibrated with a measurement from a granite bar with a well-known and good planarity.

Scans of both stiffening panels were performed in the longitudinal direction at five different positions in the transverse direction. The measurements from the read-out panel, which are of most interest, are shown in Figure 8.6. In most scans the maximum deviation was < 200 μm. However, a rather large bump with a spread of ≈ 550 μm was observed in the range $x = 100 - 400$ mm at the transverse coordinate $z = 450$ mm. It was suggested that this was caused by a deformation present in the PCBs before the gluing. However, given that the thickness of the PCB is comparable to the deformation itself we consider it unlikely that this alone was responsible for the feature. It is possible that non-optimal gluing caused it; the deformation could occur if the glue was not distributed uniformly and the vacuum system failed to rectify this. The speculations about this feature are ongoing. Although imperfections were present in the planarity, the outcome was satisfactory given that this was a first attempt to construct a panel this large.

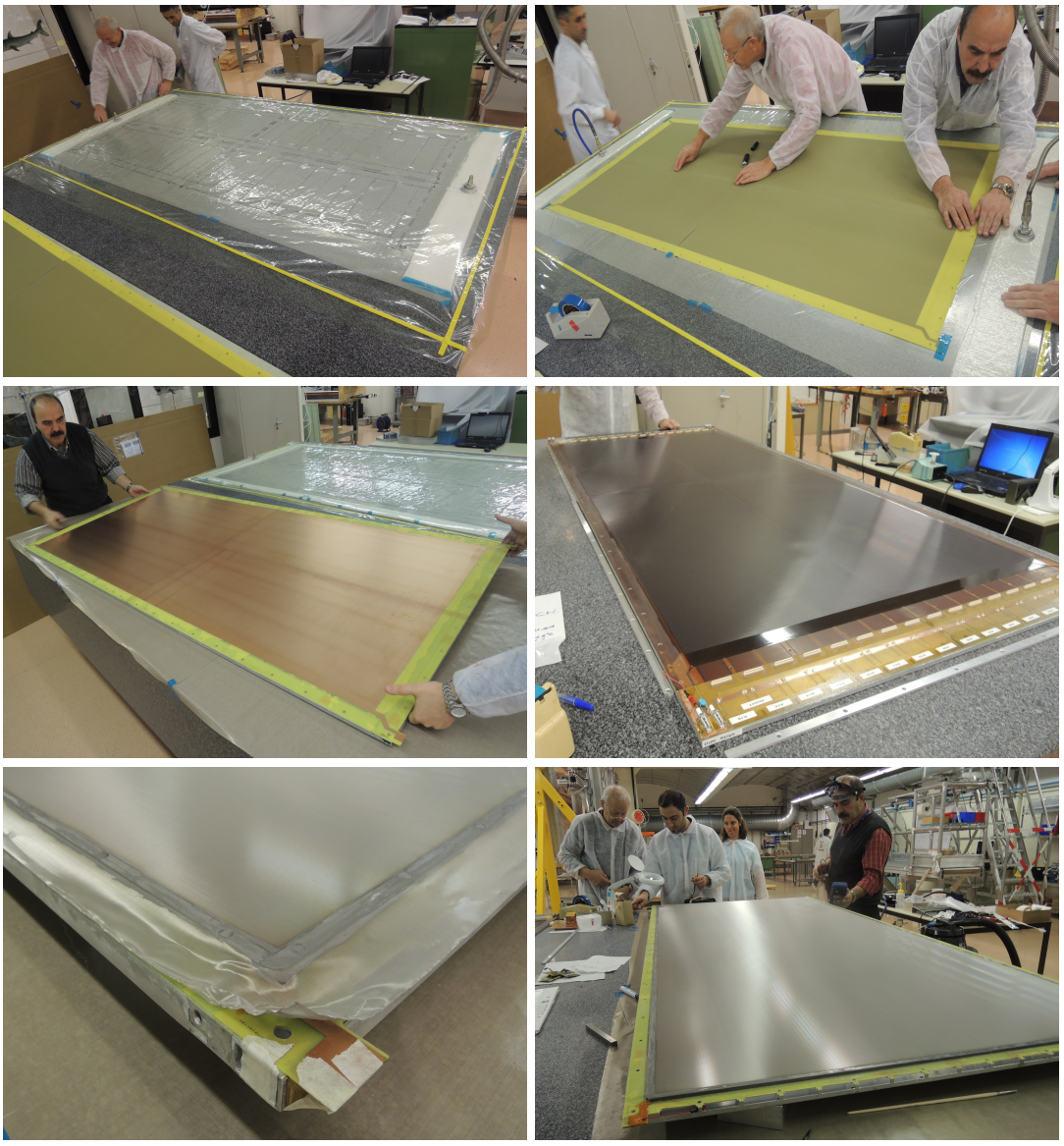

FIGURE 8.5: Top left: The mylar foil streched over the granite table. Top right: The four PCBs for the drift electrode are being prepared for being glued to the panel. Middle left: The drift panel before mounting the floating mesh. Middle right: The read-out panel. Bottom left: The floating mesh is fastened to the aluminium bars enclosing the drift electrode. The mesh is yet to be cropped. Bottom right: The final drift panel is being inspected by the MicroMegas-team

L2 was produced with a floating mesh mounted on the drift panel. A frame consisting of aluminium bars was attached at the periphery of the drift electrode. Onto this the mesh was stretched and fastened. The height of the bars defined the size of the drift region; 4.85 mm was chosen. For the mesh a cloth of woven inox with a thread diameter and density of 30 μm and 325 wires pr. inch was selected. Since special instruments are required to keep the mesh suspended during the gluing, the attachment of the mesh was done by an external partner[2]. The surfaces of the bars had to be roughened with

[2]Seritec: `http://www.seritec.ch`

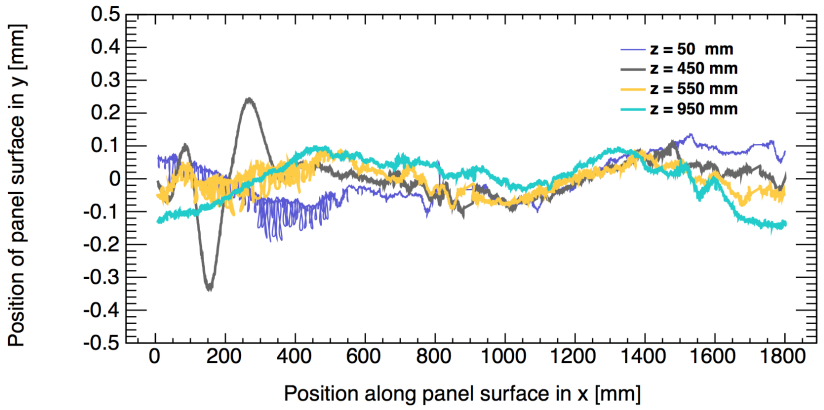

FIGURE 8.6: Planarity of the stiffening panel used for the read-out plane measured with the laser-interferometer.

sandpaper for the glue to fasten properly. The final drift panel is shown in Figure 8.5.

8.1.3 High-voltage test

A high-voltage test had to be performed before closing L2. This involved placing a copper plate directly on the pillars of the read-out structure and measuring the impedance between the plate and the resistive strips when applying high-voltage to the latter. Since air has a rather high ionization energy, the applied high-voltage had a magnitude close to 1 kV. In the ideal situation (with no electrical contact) the impedance was expected to yield some GΩ.

The copper plate was used to scan the entire active surface of the read-out panel. Several weak spots with short circuits were localized. Many of these were caused by dust; this underlined the importance of thorough cleaning of the read-out surface.

Electrical contacts occurred in some areas because of dry spots of glue. These were most likely accidentally deposited during the PCB gluing procedure. The glue itself is non-conducting, but any dust trapped in it will carbonize during exposure to high-voltage and thus create a permanent contact. To block this contact, the affected areas were covered with a layer of Kapton® tape; this remedied the issue, but all affected areas were left non-functioning. An affected area is shown in Figure 8.7.

8.1.4 Assembly

Before closing L2, SHV connectors and RC-filters were mounted at the corners of the panels like was done with L1 (see Chapter 7).

The read-out surface and the mesh were cleaned carefully with an electrostatic roller as shown in Figure 8.8. The read-out panel was placed on a table with the active surface

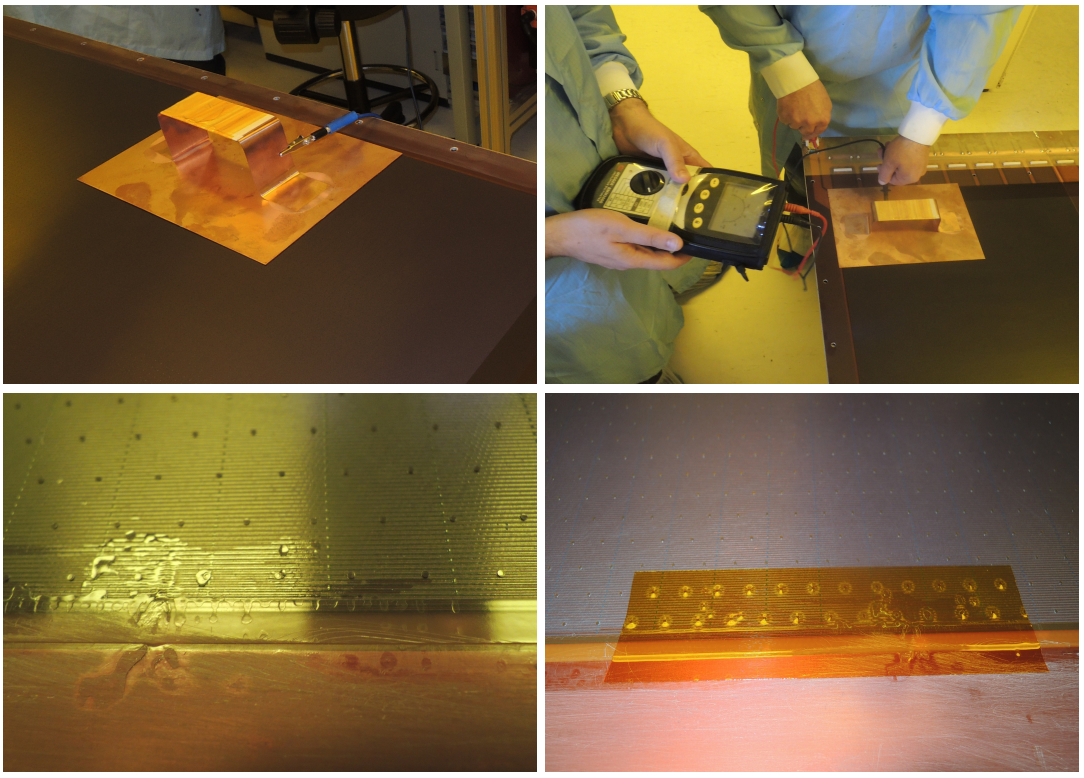

FIGURE 8.7: Top: A high-voltage test is performed in air with a copper plate. Bottom: A spot of dry glue at the edge of the active area of the read-out panel causing a short circuit. The affected area was covered with Kapton® tape to block the contact.

facing upwards and the chamber was closed by placing the drift panel on top of it. To make the chamber gas-tight, a 6 mm diameter ribbon O-ring was positioned externally of the mesh-frame. 5 mm aluminium bars were inserted in the open gap between the two panels. The whole L2 structure was sealed with ⌀ 6 mm screws. The completed L2 chamber had a weight of 32 kg.

8.2 Experimental setup and detector operation

At the point of finishing L2 the only means of testing it at CERN was with cosmic data. A dedicated cosmic stand was installed in the RD51 laboratory for this purpose. The stand consisted of three planar scintillators positioned 30 cm, 50 cm and 65 cm above L2. The top and middle scintillators had the dimensions 0.24×2 m^2 while the bottom measured 0.24×1.5 m^2. Each of the three scintillators covered one full side of L2 in the longitudinal direction and they were aligned by eye in the transverse direction. A sketch of the setup is shown in Figure 8.9.

Each scintillator was equipped with a trapezoidal light guide and a PMT. The analog signals from the PMTs were connected to a LRS 621AL discriminator. The discriminator output signals were connected to a LRS 465 coincidence unit, which on a three-fold

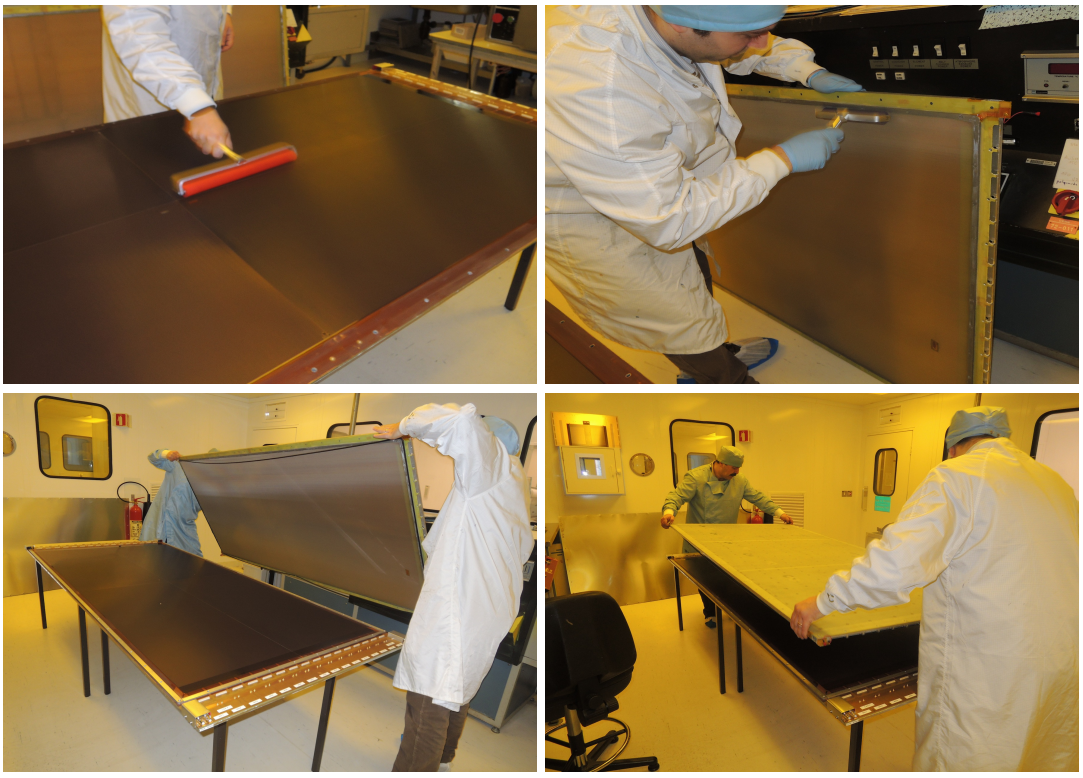

FIGURE 8.8: Top left and right: The active surface of the read-out panel and the floating mesh is cleaned with a static roller. Bottom left and right: The L2 chamber is closed by joining the two panels together.

coincidence provided a (NIM) signal being used for the trigger and for counting the rate with a CAEN N145 quad scaler.

High-voltage to L2 was provided by the CAEN mainframe described in Chapter 5. The quarters of the drift electrode were connected to the same high-voltage line by the use of a splitter. Each quarter of the read-out plane was connected to an individual high-voltage line such that the quarters of L2 could be operated independently. This was particularly useful for monitoring and localizing leakage currents and for performing the studies in Section 8.5.

L2 was operated with the standard Ar/CO_2 93/7% gas mixture supplied with a flow of $\approx$ 10 L/hour. Based on the experience obtained in Chapter 7, the L2 chamber was expected to obtain efficient operation around 560 V.

The data acquisition relied on the SRS system described in Chapter 5. Each side of L2 was equipped with 16 APV hybrids. The trigger rate was monitored with both the scaler and the data-taking software. Given that the flux of cosmic rays at ground level is $\approx$ 100 Hz/m^2 [1], with the geometry of the stand (the area of the smallest scintillator being $\approx 1/3$ m^2) and the solid angle of the cosmics, we expected the rate to be around 5 Hz. The obtained rate was slightly lower, around 3-4 Hz. We attribute this to imperfections in the setup such as misalignment and inefficiency of the scintillators.

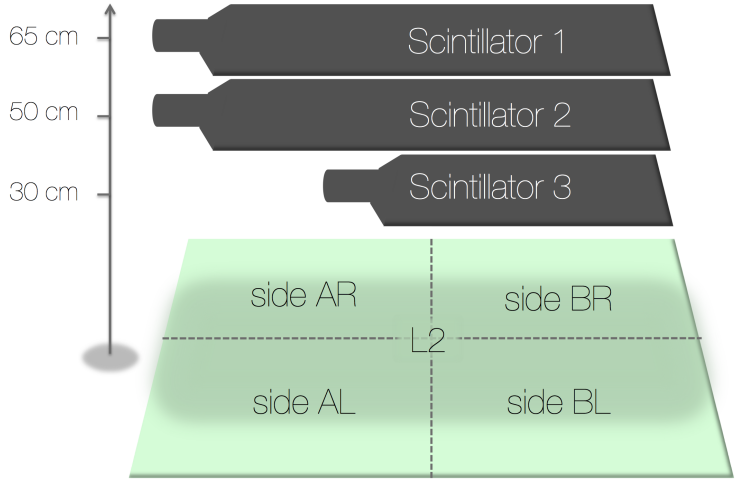

FIGURE 8.9: Schematic of the cosmic stand used for testing L2.

8.3 First switching on

In the first attempts to switch on L2, leakage currents at the order of 60 nA were observed in the AL quarter. The chamber therefore several times had to be brought back to the clean room for inspection. It was initially suspected that overlooked gluing defects caused this behavior. However, by performing high-voltage tests like described in Section 8.1.4 it became apparent that the cause was dust trapped on the read-out surface. Thorough cleaning remedied the issue. The importance of excruciatingly clean conditions when working with large-area detectors was underlined again. Furthermore, it was found that less dust was trapped when the chamber was closed by joining the two panels vertically rather than horizontally.

Another behaviour related to the size of L2 was experienced soon after operation was initiated. Like was the case with L1, the combination of a slight over-pressure in the chamber and the large surface area made the surfaces bulge. This deformation was merely a matter of a few mm, but the effect was significant enough to lower the efficiency of the chamber. To overcome the problem, machined bars of aluminum were clamped onto the surface of L2 (shown in Figure 8.10) to maintain its planarity. This recovered the issue. As a direct result of this experience, all future large-area MicroMegas detectors will be constructed with an internal system to prevent the bulging.

After having complied with the above issues L2 was switched on with minimum leakage currents and a satisfactory trigger rate. One of the first signals provided by L2 observed with the online monitoring tool is shown in Figure 8.10.

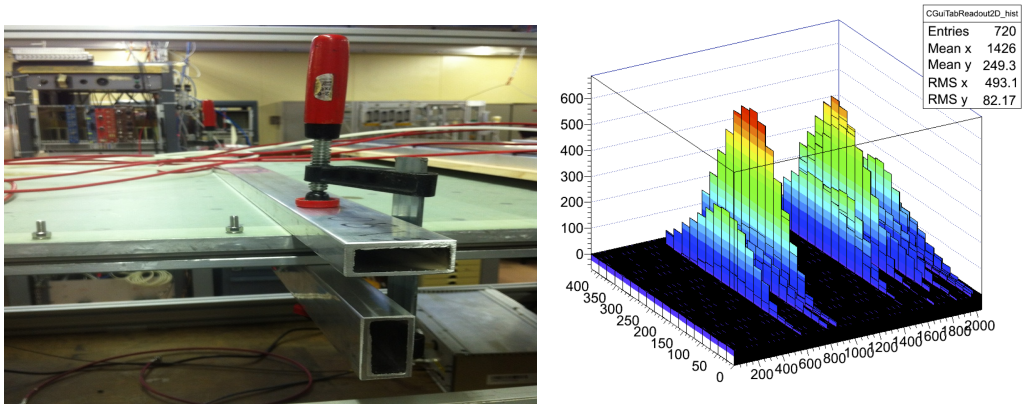

FIGURE 8.10: Left: Aluminum bars were clamped to the surface of L2 to maintain planarity. Right: One of the first online events, a cosmic shower, measured with L2.

8.4 Uniformity of response

The uniformity of L2 was of particular interest because mechanical defects were expected to propagate to its response and hence be directly visible. To assess the uniformity, a long run was recorded separately with side A and B. The trigger configuration was like shown in Figure 8.9, however, the bottom scintillator had been shifted in the longitudinal direction to maximized the coverage over either of the sides. L2 was operated with a high-voltage of 580 V.

The distribution of clusters as a function of strip position is presented in Figure 8.11 for both side A and B[3]. In side A the negative strip numbers correspond to side L and the positive numbers to side R, and vice versa in side B. Two samples are considered; all recorded events and events containing a single cluster. We expect the distribution to be smooth and have the bulk of events contained in the central part of the detector because of the coverage of the scintillators and the solid angle of the cosmics exhibiting the $\propto \cos^2\theta$ dependence [1]. In both side A and B the bulk of events indeed fall within the central part of the chamber. When selecting single-cluster events the coverage of the scintillators becomes even more apparent.

A few issues are noticed that can be related to the mechanics of the detector. In side A a quite apparent dip in the distribution is observed at the center of the chamber, being slightly more dominant at side R. This will be investigated further in Section 8.4.1.

Another feature of the distribution at side AR is the behaviour close to the edge of the chamber. Unlike at the other edges, the distribution is cut of rather abruptly. This particular edge was contaminated with spots of dry glue, and a part of it was thus covered with Kapton® tape like described in Section 8.1.3. It is probable that this altered the behaviour of the chamber in that area.

[3]These results were presented at EPS 2013 [50]

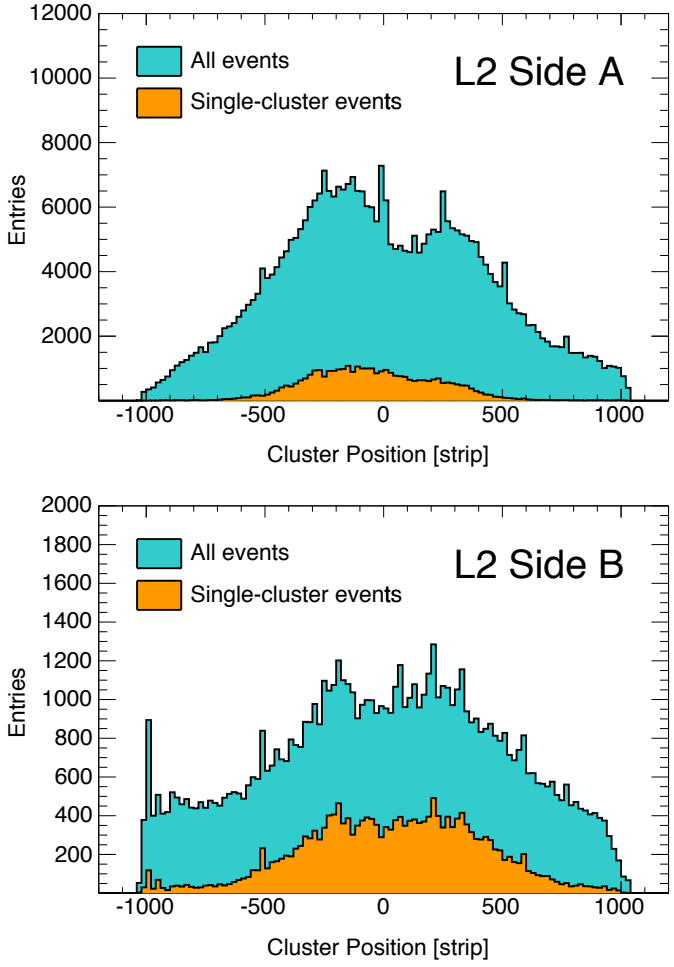

FIGURE 8.11: Distribution of clusters as a function of strip position measured with L2 side A and B.

The cluster distribution recorded with side B does not visibly suffer from any issues and it approximately follows the expected shape.

8.4.1 Surface scan

To investigate the dip in the response at side A, a surface scan was performed with the scintillator configuration shown in Figure 8.12. The bottom scintillator was turned 90° and by placing it at certain positions the events impinging in a specific part of the detector were selected. It was in this way possible to evaluate the response from a subset of the detector. The surface scan was performed in four steps with side A. Step 1 denotes the area closest to the middle of L2 meanwhile step 4 is closest to the read-out. Around 4k events were recorded in each step.

The distribution of clusters as a function of strip position is shown for the four steps in Figure 8.13. In step 3 and 4 a dip is observed in the response around the center of

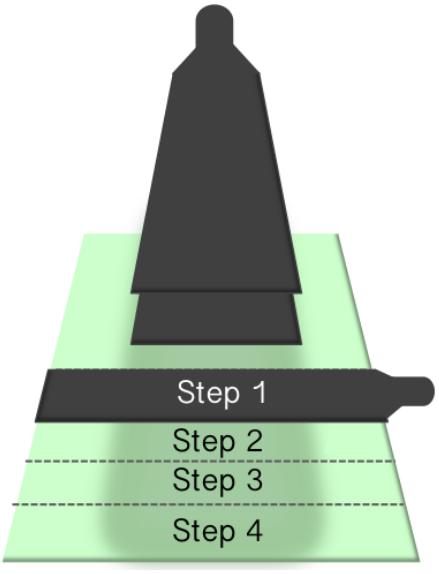

FIGURE 8.12: The scintillator configuration used for the surface scan of L2.

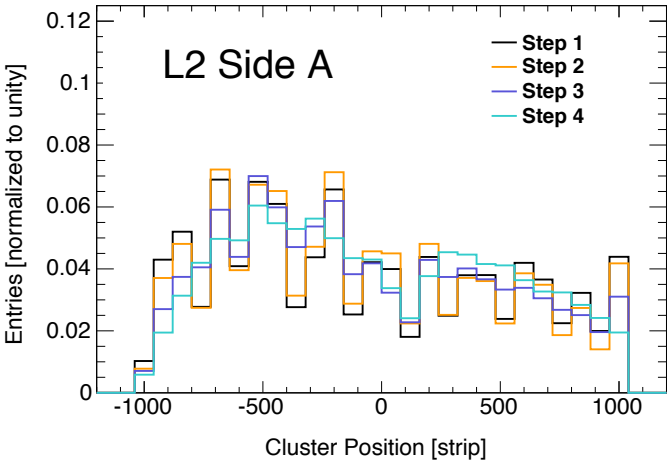

FIGURE 8.13: Distribution of clusters as a function of strip position measured at four different positions on side A.

the detector, which is consistent with the location of the dip in Figure 8.11. Since this behaviour is not observed in the first two steps, we believe that the reason for the dip is a mechanical effect confined to a certain part of the detector; the position of the dip coincides with the rather large deviation in the planarity of the read-out panel found in Section 8.1. The effect from this is discussed in Section 8.4.3.

8.4.2 Charge response

By examining the charge response, characteristics that were not distinguishable with the methods of the previous section become visible. In order to do so, we again consider

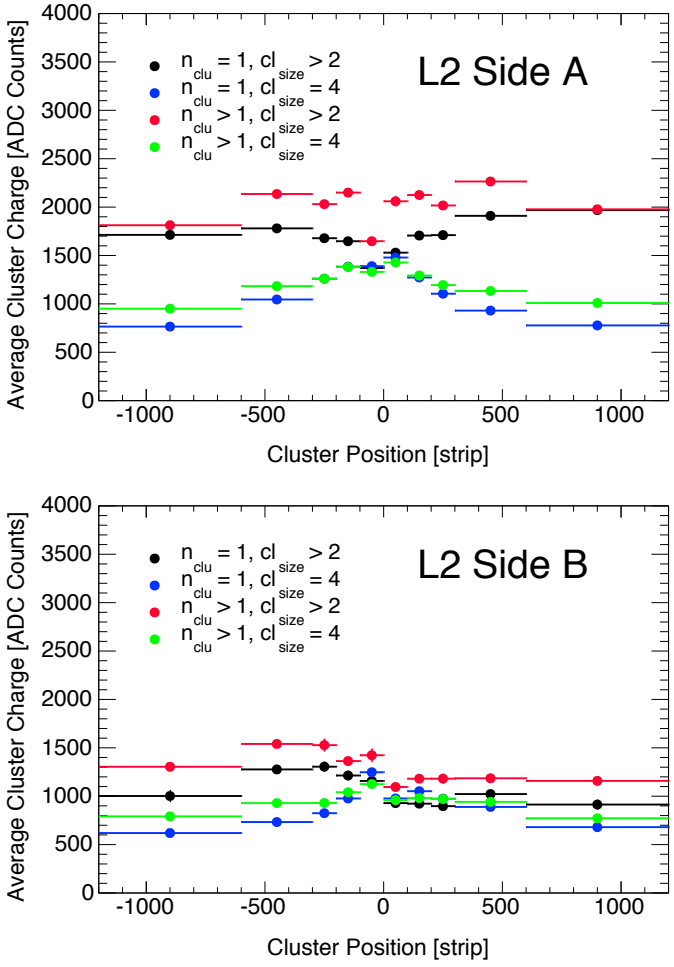

FIGURE 8.14: Average cluster charge measured with side A and B.

the data sets from Section 8.4. The ideal way to probe the uniformity of the charge response is to consider the charge spectra measured with a small group of strips and examine it with a Landau fit like was done in Chapter 7. However, because of limited statistics, the average cluster charge is used instead.

The cluster charge averaged over a group of strips as a function of strip position is shown in Figure 8.14. Four different samples are distinguished: single- and multi-cluster events with both fixed and variable cluster size. The fixed cluster size is required to be 4 strips, which corresponds to the approximate average value. The bins towards the edges of the chamber are larger to maintain a meaningful amount of statistics. Errors are reported as the error on the mean.

In side A, in the curves with unconstrained cluster size the charge yield at the center of the chamber is slightly lower than at the edges. This is considered a geometrical effect; clusters reconstructed near the edges of the chamber on average contain more charge because the particles impinging there will have a larger inclination and thus traverse more gas. Correspondingly, the multi-cluster events contain more charge. Similar effects

are observed in side B, however not as pronounced. With the influence from these geometrical effects it is difficult to draw conclusions on the uniformity of the charge response.

8.4.3 Discussion

The dip in the response at side A is likely to be caused by the dis-planarity observed in Figure 8.6. If the read-out surface deforms rapidly, the floating mesh might not be able to attach properly to the pillars, which would result in a reduced gain and impact the efficiency negatively. We consider this is a plausible explanation. This feature is important because it demonstrates the vulnerability of the large-area MicroMegas detectors to mechanical defects. All future detectors must therefore be constructed with utmost care to avoid these incidences.

If the charge uniformity measurement should be optimized, the data should be recorded with a setup that would not introduce any angular dependence on the selected events. This could for example be done with scintillators covering the full width of the chamber, which is a method that for example was used in the commissioning of the present detectors in the ATLAS Muon Spectrometer. However, with our setup, such was not possible.

8.5 Mesh fixation

Access to the experimental site will be limited once MicroMegas detectors have been installed in ATLAS. Each MicroMegas detector in the NSW will cover one full sector and be equipped with 8 PCBs and one large floating mesh. If defects occur in a confined area of the detectors, the unaffected parts must still be operational. Concerns about the concept of the floating mesh were raised in this context; it was not evident that the mesh would work as intended if either of the detector was switched off. This could be probed quite easily with L2.

The functionality of side BL was studied when side BR was switched off (i.e. no high-voltage was applied to the resistive strips). Any effect in the response was expected to be most pronounced towards the center of the detector, i.e. closer to the side being switched off. To test this, several runs were taken with side B with the trigger configuration in Figure 8.9.

At first a high-voltage scan was performed with side BL from 480 - 580 V in steps of 10 V. To enable comparison with the ideal situation where all parts are switched on, a set of calibration runs were recorded with both side BL and BR being switched on. The calibration runs were recorded at three intermediate high-voltage values at 500, 540 and 580 V.

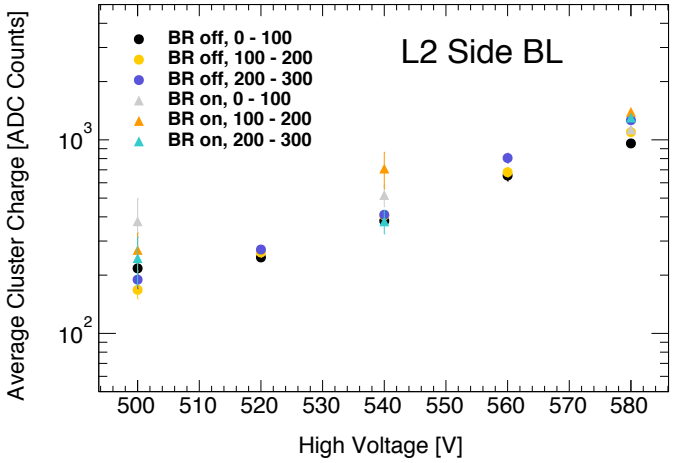

FIGURE 8.15: Average cluster charge measured as a function of high-voltage with side BL when the BR side was switched on and off.

In Figure 8.15 the average cluster charge for single-cluster events measured with side BL is shown for strips in the range 0-100, 100-200 and 200-300. The low strip numbers correspond to the center of the detector. In each strip range two data points are shown, corresponding to side BR being switched on or off. Errors are reported as the error on the mean. When side BR is switched off the charge yield from the strips being closest to the center of the detector is slightly lower. This effect is less pronounced for the strips being further away. In the calibration runs the charge yield is slightly higher in the strips closest to the center, which is the case at all high-voltage values. However, this effect is small when considering the size of the errors.

The effect is investigated further in Figure 8.16, which plots the average cluster charge as a function of strip position for all strips in side BL. The two curves correspond to the calibration run where side BR was switched on and a run where BR was off. The sides were operated with 580 V. In the 200 strips closest to the center, the charge yield is $15 - 20\%$ higher in the calibration run, which is compatible with Figure 8.15. Towards the edge of the chamber it is difficult being conclusive about the behaviour of the calibration run because of the relatively large errors. However, in the intermediate strip range (200 - 600) there is no indications of systematic differences in the charge yield.

8.5.1 Discussion

The geometrical effects discussed in the previous sections will undoubtedly have affected the data presented in Figure 8.15 and 8.16. However, since we compare data to data and the same scintillator configuration was used for all runs, the indications from the results are valid. The above results suggest that the charge yield is suppressed slightly when

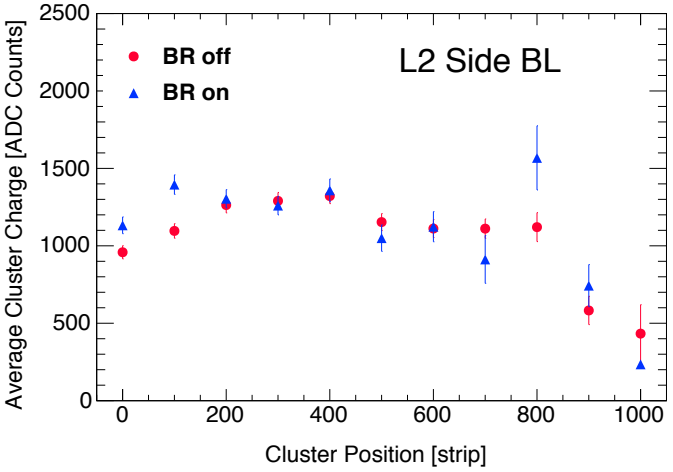

FIGURE 8.16: Average cluster charge measured as a function of strip position at 580 V with side BL when the BR side was switched on and off.

only part of the detector is operated. The interpretation of this is that the floating mesh in the area that is switched off does not confine to the pillars, which pulls the mesh upwards in the adjacent area. Our study indicates that this effect is small and is confined to the 200 strips bordering to the inactive side, corresponding to the closest ≈ 10 cm. The concept of the floating mesh should hence not be a source of concern in the context of partial operation of the large-area detectors.

8.6 Gain dependence on applied voltage

As a basic sanity check we estimate the dependence of the gain on the applied high-voltage. The procedure follows that presented in Chapter 7. A high-voltage scan was performed with both sides of L2 in the range 480 - 580 V in steps of 10 V with the scintillator configuration depicted in Figure 8.9. A selection of cluster charge distributions for single-cluster events measured with side A are shown in Figure 8.17. A Landau fit is imposed to all distributions. Remaining distributions are in Appendix C.

The MPV from each fit is used as an estimator of the gain. In Figure 8.18 the MPV-values extracted from both side A and B are shown as function of the high-voltage. The errors are reported as the uncertainty on the MPV extracted from the fit.

Both curves follow the anticipated exponential trend, except the two first data points that are slightly off. The curve representing side B exhibits some fluctuation around $550 - 570$ V, which causes it to deviate slightly from the overall trend. The reason for this is not known, but is likely to be a result of temporary changes in operational parameters such as the temperature. We furthermore notice that the curves from side

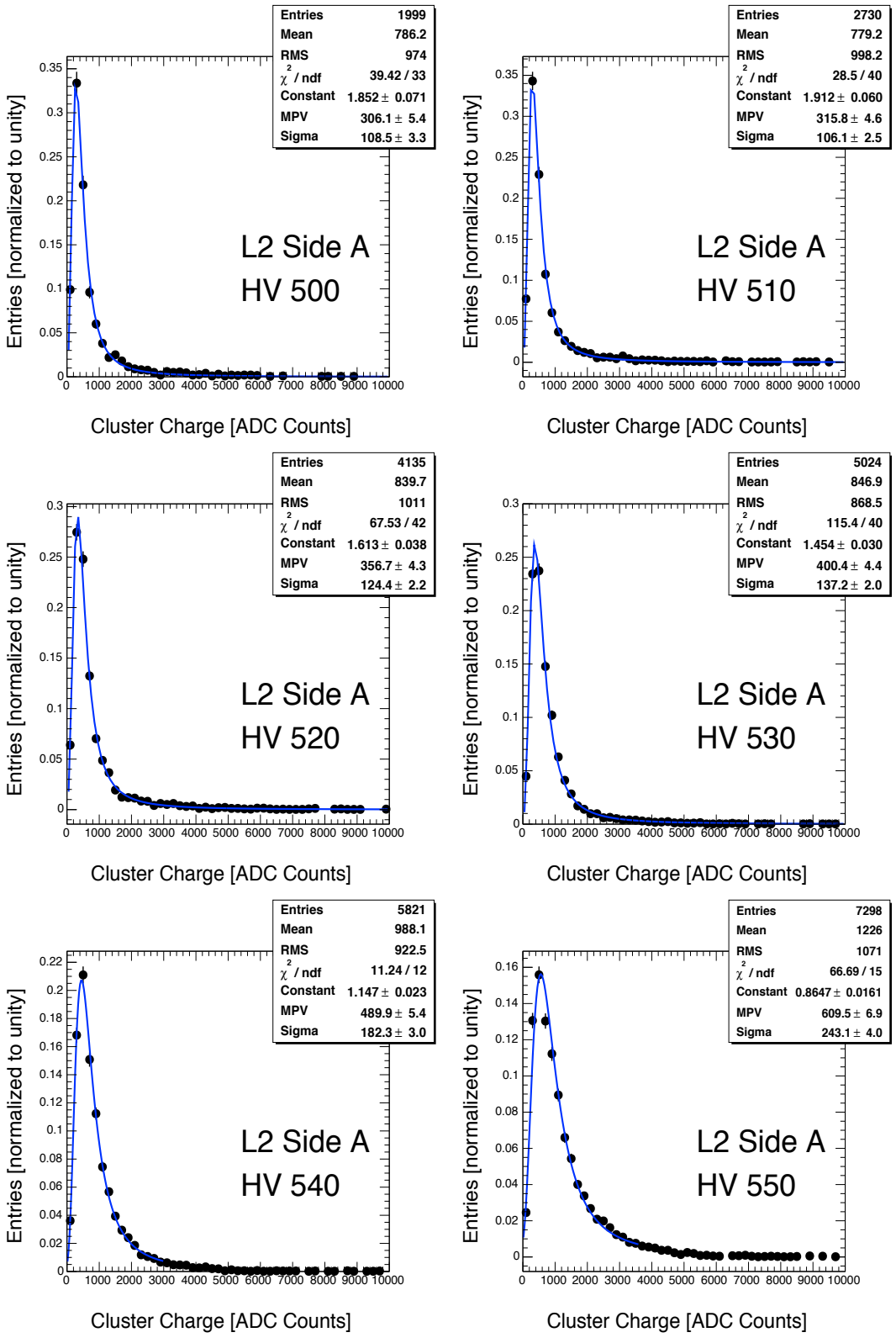

FIGURE 8.17: Integrated cluster charge distributions for single-cluster events measured with side A in the high-voltage range 500 - 550 V. A fit with a Landau function is imposed to the distributions.

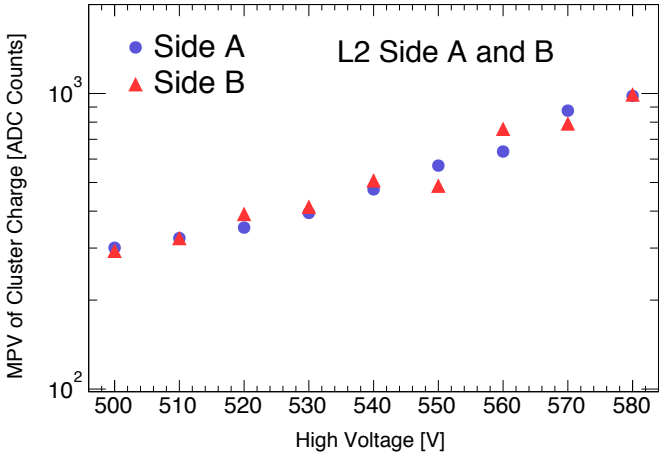

FIGURE 8.18: The MPV-values extracted from the cluster charge distributions as a function of high-voltage.

A and B approximately take on the same values, which means the response from the two sides are comparable.

8.6.1 Discussion

The same concerns about the capacity of the experimental setup and the selection discussed in Section 7.3.1 apply here. It is probable that the charge distributions measured at the two lowest high-voltage values have been truncated towards higher values. This can explain why they are off the general trend of the curves. Given this is only two data points we consider the results valid; the study suggests that the gain of L2 depends exponentially on the applied high-voltage, which is in agreement with the prediction from the Diethorn approximation.

8.7 Conclusion

The task imposed by the milestones concerned demonstrating that a full-sized prototype could be constructed with adequate mechanical precision. This was indeed the case; L2 was, within the limits of our studies, fully functional. With this fact we proved that the two-paneled construction scheme utilizing a floating mesh is suitable for producing detectors at the NSW-scale.

The work with L2 highlighted central issues about the influence from the mechanics on the detector response; even minor imperfections were directly visible. This knowledge will be used to set a high standard for the mechanical accuracy in the construction of future detectors. The need for certain design parameters was moreover learned; for example, an internal system to prevent the chambers for bulging. The implementation

of all future large-area detectors will rely on the experience obtained with L2.

Given that the work with L2 overall was highly successful, another item in the list of milestones has been fulfilled.

Chapter 9

Summary and Outlook

In this thesis the capabilities of the MicroMegas technology were studied and further developed. Since this technology is relatively new compared to wire-based technologies, the work presented throughout the thesis was essential for demonstrating that MicroMegas is mature for the LHC environment and can safely be deployed as tracking detectors in the ATLAS Muon Spectrometer. The aspects that had to be demonstrated were quantified by a list of milestones, which the MAMMA Collaboration had to fulfil.

The NSW must provide space points in the η-coordinate measured with a single-plane resolution of 100 μm or better. To show that this is attainable, a study was performed with test-beam data recorded with the bulk T chambers. A proof of concept of the μTPC technique where the MicroMegas drift region is exploited as a time projection chamber was performed. The resolution obtained with this technique increased with track inclination, which was in direct contrast to that obtained with the traditional charge centroid method. By combining these two techniques, with a simple weighted average, the angular dependence of the resolution diminished in the full range $10^\circ - 40^\circ$. Moreover, the obtained single-plane spatial resolution was close to or below the desired 100 μm (the worst obtained resolution being (111 ± 11) μm). By optimizing the combination method this can be improved further.

A key parameter for the detectors to be installed in the NSW is size. MicroMegas detectors had before the summer of 2012 never been built larger than L1. A vital aspect for the NSW project hence concerned constructing the first functional large-area prototypes. For this endeavour new construction schemes were probed; electrodes were composed of large PCBs and the floating mesh technique was developed.

The first large chamber, L1, measured 1×1 m^2. The test-beam campaign allowed for direct comparison of its response to that of the smaller bulk chambers. Important lessons about the operational characteristics of floating mesh detectors were pinpointed; these have to be operated at a significantly higher voltage to perform comparably to the

bulk chambers. This knowledge was directly applicable to the full-sized prototype.

The full-sized prototype, L2, measured 1×2.4 m^2 and was the largest functional MicroMegas detector built. The construction provided invaluable experience about manufacturing and assembly techniques. L2 was tested in a cosmic stand made for the purpose. Its response indicated that it was well-functioning. However, the sensitivity of the response to mechanical defects was underlined. This knowledge will impose requirements for quality assurance in the construction of future detectors. Furthermore, with L2 it was proven that a full-sized floating mesh works as intended when only a part of the detector is operated. This latter fact makes the technology robust for long-term use.

With the above accomplishments the objectives of the milestones were satisfied. It has been proven that the MicroMegas technology can comply with the characteristics required for tracking detectors in the ATLAS Muon Spectrometer. MicroMegas along with the sTGC technology will be deployed in the NSW, which are to be installed in 2018. This will enable ATLAS to continuously deliver adequate muon performance after the LHC luminosity upgrade.

As a final remark it is worth mentioning that MicroMegas usage is not limited to ATLAS. The technology has furthermore been suggested for experiments at both the International Linear Collider (ILC) and the Compact Linear Collider (CLIC). The high-energy physics community should thus become acquainted with the technology since its use will be common and widespread in the future. MicroMegas belongs to the experiments of tomorrow.

Part III

Appendix

Appendix A

Appendix to Chapter 6

The error on x_{half} can be found by standard error propagation and will be given by the expression [51]

$$\sigma_{x_{half}} = \sqrt{\left(\frac{\partial x_{half}}{\partial \alpha}\right)^2 \sigma_\alpha^2 + \left(\frac{\partial x_{half}}{\partial t_0}\right)^2 \sigma_{t_0}^2 + \left(\frac{\partial x_{half}}{\partial v_{drift}}\right)^2 \sigma_{v_{drift}}^2} \tag{A.1}$$

under the assumption that the errors on t_0, v_{drift} and x_{half} are uncorrelated and that no error on z_{half} is present. Given that

$$\frac{\partial x_{half}}{\partial \alpha} = \frac{t_0 \times v_{drift}}{\alpha^2} \tag{A.2}$$

$$\frac{\partial x_{half}}{\partial v_{drift}} = -\frac{t_0}{\alpha} \tag{A.3}$$

$$\frac{\partial x_{half}}{\partial t_0} = -\frac{v_{drift}}{\alpha} \tag{A.4}$$

the total error on x_{half} becomes

$$\sigma_{x_{half}} = \sqrt{\left(\frac{t_0 \times v_{drift}}{\alpha^2}\right)^2 \sigma_\alpha^2 + \left(\frac{t_0}{\alpha}\right)^2 \sigma_{v_{drift}}^2 + \left(\frac{v_{drift}}{\alpha}\right)^2 \sigma_{t_0}^2} \tag{A.5}$$

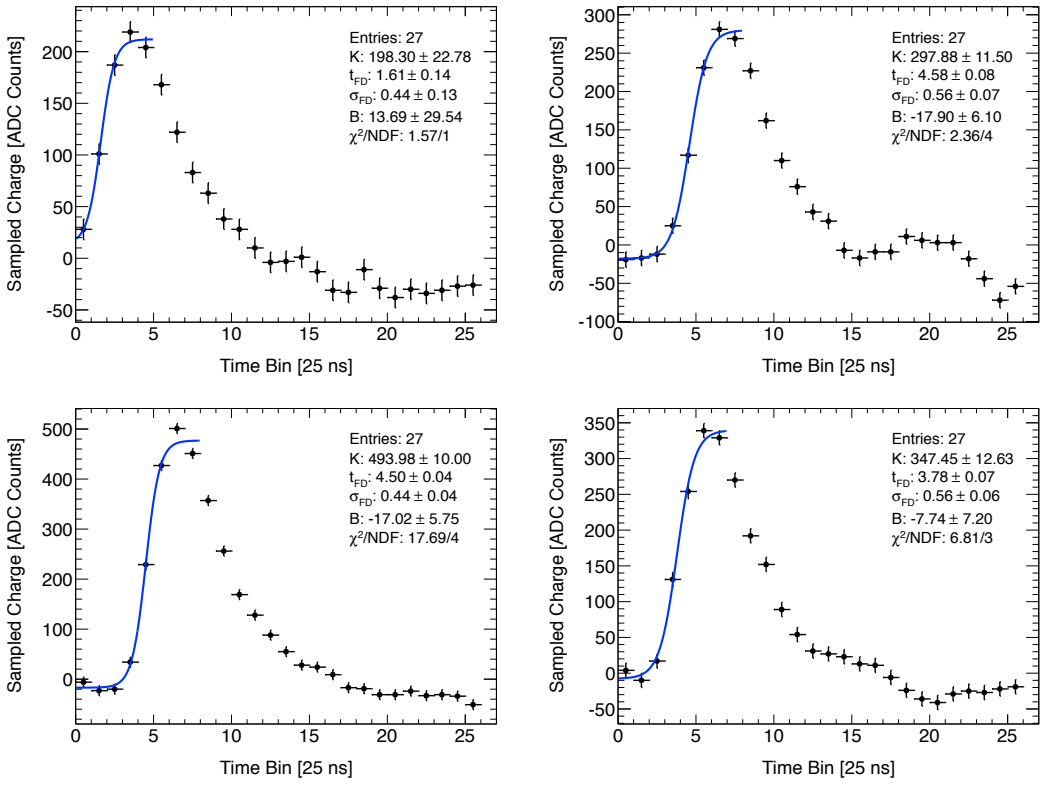

FIGURE A.1: Reconstructed pulses from the T1 chamber with Fermi-Dirac fits imposed.

Appendix B

Appendix to Chapter 7

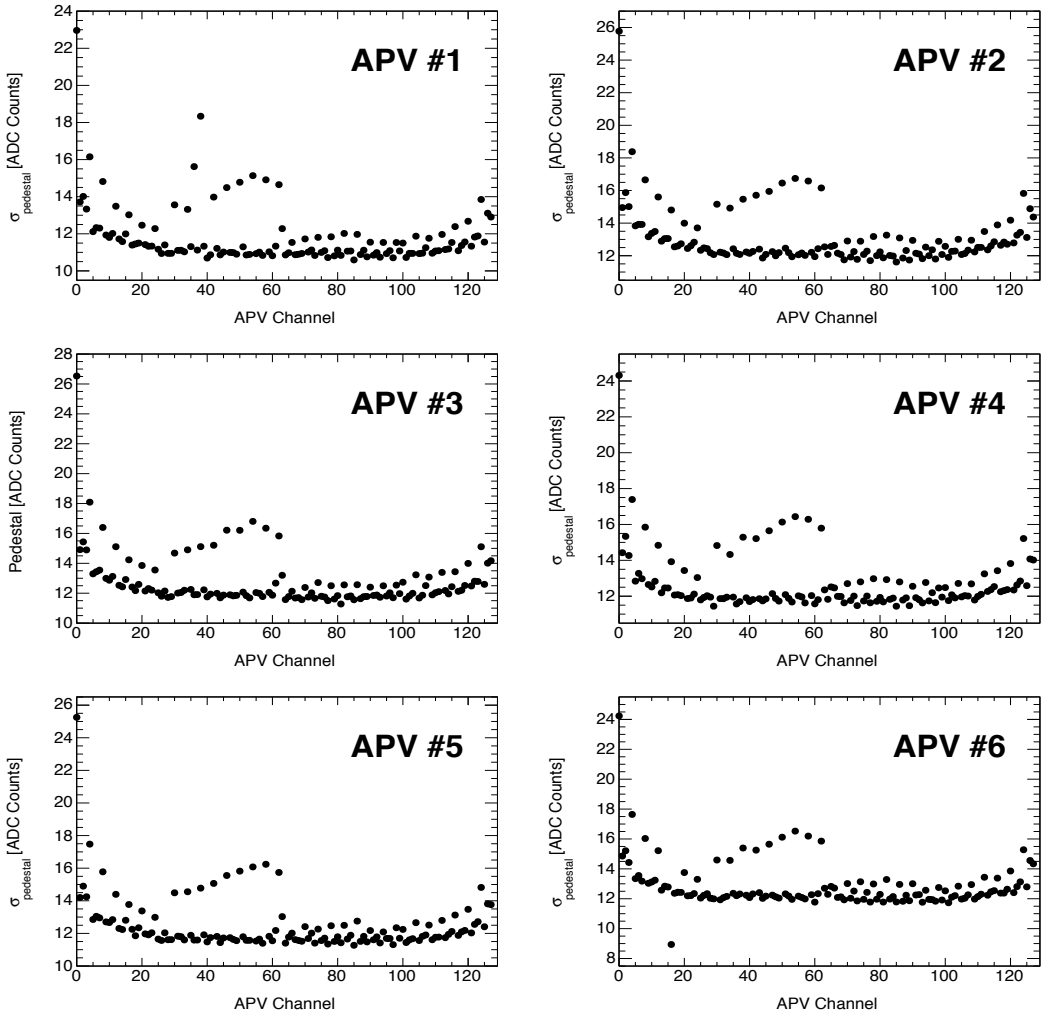

FIGURE B.1: Pedestal standard deviation obtained from the APV hybrids mounted on the T chambers in test-beam.

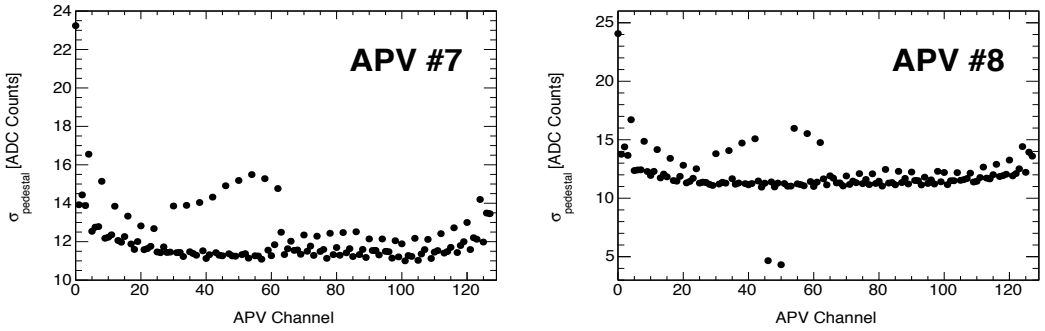

FIGURE B.2: Pedestal standard deviation obtained from the APV hybrids mounted on the T chambers in test-beam.

Appendix C

Appendix to Chapter 8

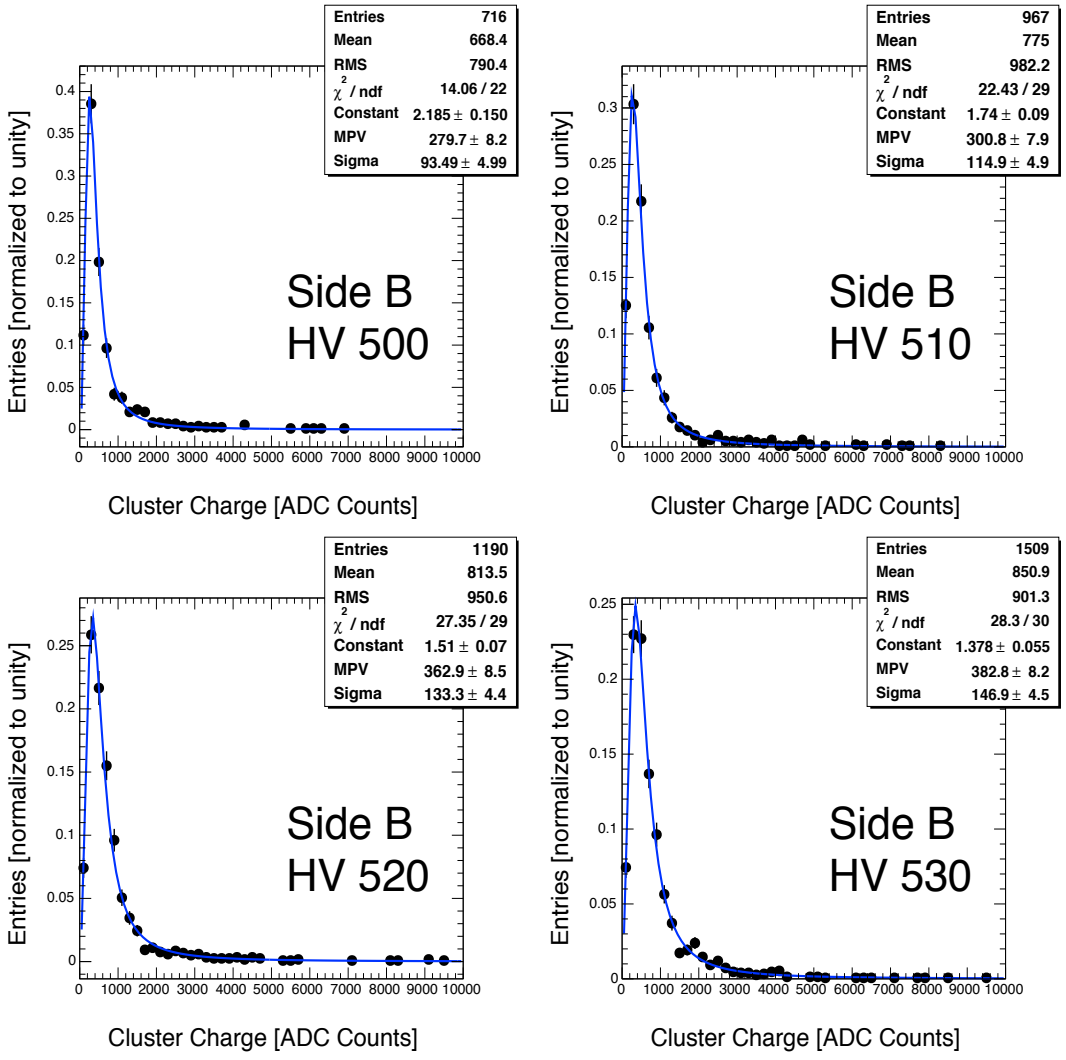

FIGURE C.1: Integrated cluster charge distributions for single-cluster events measured with L2 side B in the high-voltage range 500 V- 530 V.

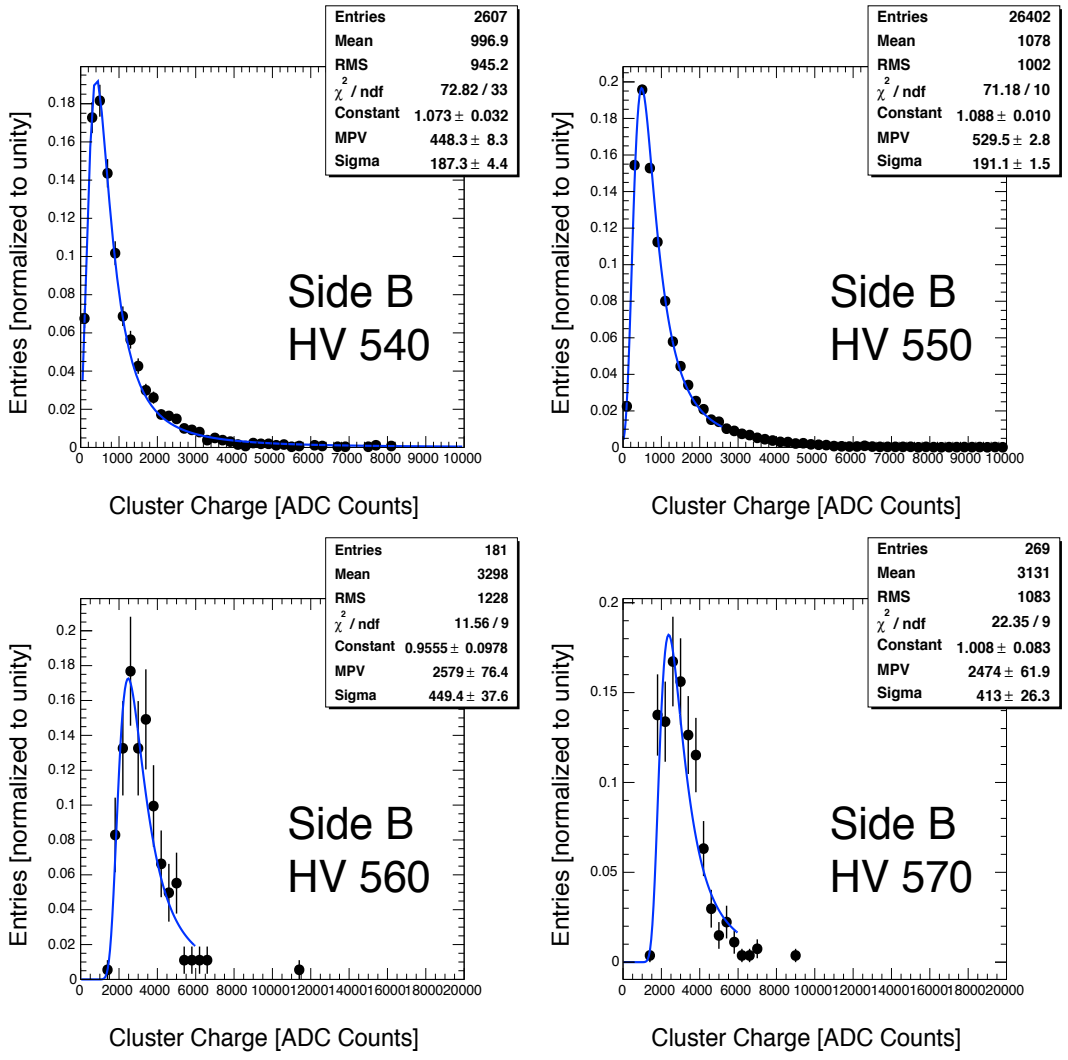

FIGURE C.2: Integrated cluster charge distributions for single-cluster events measured with L2 side B in the high-voltage range 540 V- 570 V.

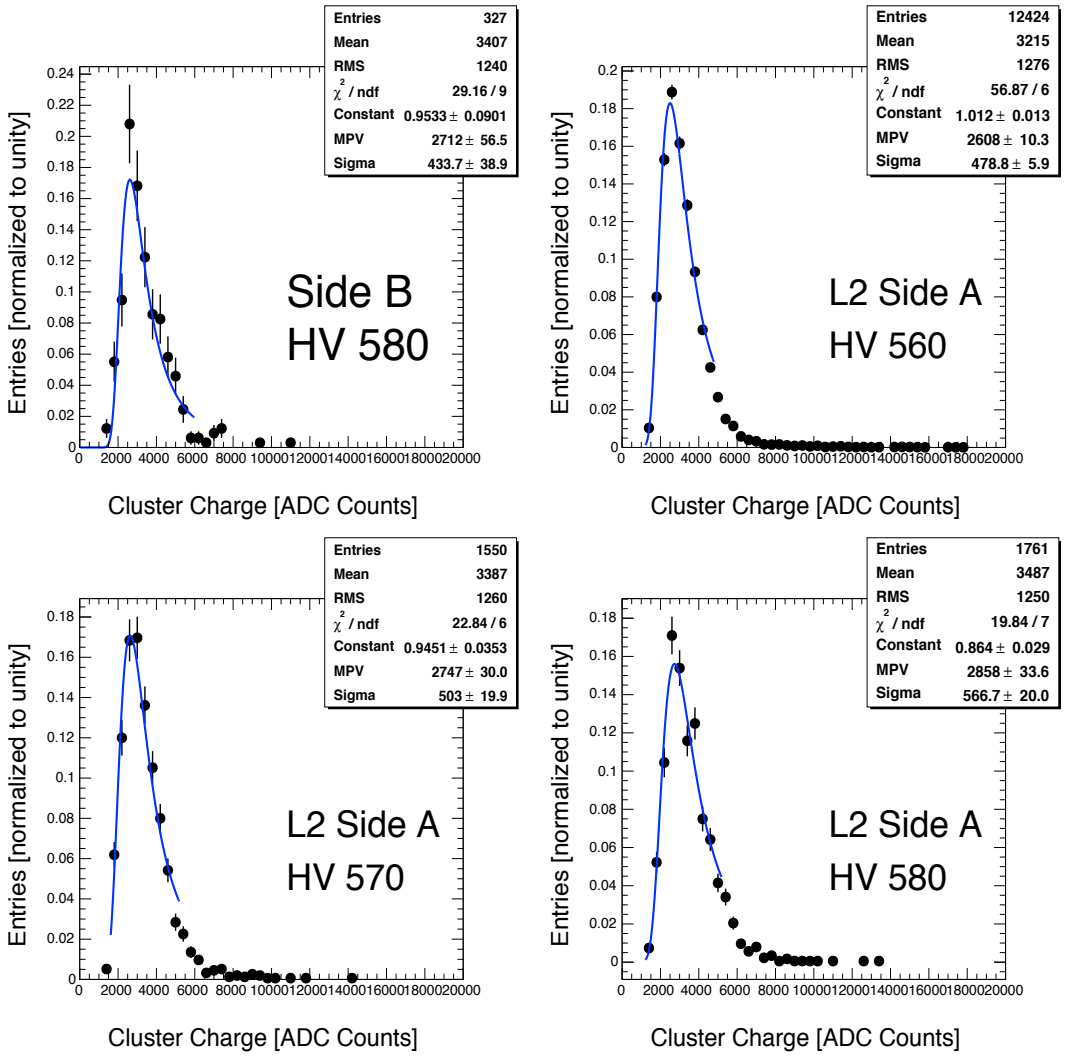

FIGURE C.3: Integrated cluster charge distributions for single-cluster events measured with L2 side B with 580 V and L2 side A 560 V - 580 V.

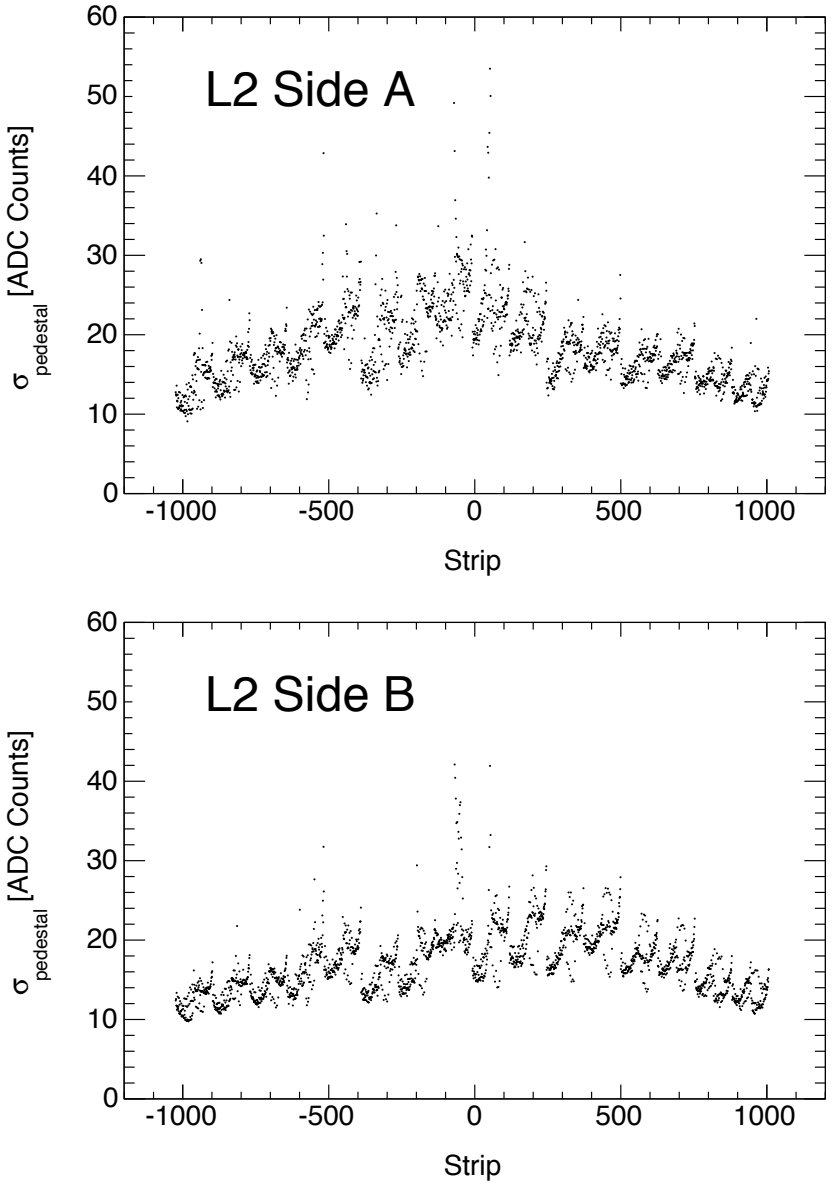

FIGURE C.4: The pedestal fluctuations obtained from L2 side A and B.

Bibliography

[1] J. Beringer and et.al. (Particle Data Group). *The Review of Particle Physics. Phys. Rev. D86*, Nov 2012.

[2] H. Bichsel. *A Method to Improve Tracking and Particle Identification in TPCs and Silicon Detectors. Nucl.Instrum.Meth.*, A562:154–197, 2006.

[3] T. Montaruli. *Detectors: scintillators, photomultipliers, semiconductor detectors and photodiodes*, 2009.

[4] S. Vlachos and et. al. *The New Small Wheel Technical Design Report.* 2013.

[5] T. Alexopoulos, J. Burnens, R. de Oliveira, G. Glonti, O. Pizzirusso, et al. *A Spark-Resistant Bulk-Micromegas Chamber for High-Rate Applications. Nucl.Instrum.Meth.*, A640:110–118, 2011.

[6] Fabio Sauli. *Micro-Pattern Gas Detectors. Nucl.Instrum.Meth.*, A477(1–3):1 – 7, 2002.

[7] CERN. CERN FAQ: LHC the Guide, June 2009.

[8] CERN. CERN Document Server, June 2009.

[9] K. Bachas, N. Benekos, F. Cerutti, M. Hoffmann, J. Meyer, and R. Nicolaidou. *Performance of the Muon Spectrometer in the High Pseudo-Rapidity Region.* (ATL-MUON-INT-2012-002), Apr 2012.

[10] ATLAS Muon Combined Performance group. Muon Combined Performance, June 2009.

[11] G. Aad et al. *The ATLAS Experiment at the CERN Large Hadron Collider. JINST*, 3:S08003, 2008.

[12] T. Argyropoulos and et.al. *Cathode Strip Chambers in ATLAS: Installation, Commissioning and in-situ Performance. IEEE Trans.Nucl.Sci.*, 56:1568–1574, 2009.

[13] C. Bini. *Study of the Performance of the ATLAS Muon Spectrometer.* (ATL-MUON-PROC-2011-008), Nov 2011.

[14] G. Cattani. *Performance of the ATLAS Resistive Plate Chambers.* (ATL-MUON-PROC-2010-001), May 2010.

[15] W. R. Leo. *Techniques for Nuclear and Particle Physics Experiments.* Springer, 1994.

[16] W. Blum, W. Riegler, and L. Rolandi. *Particle Detection with Drift Chambers.* Springer, 2008.

[17] D. Green. *High pT Physics at Hadron Colliders.* Cambridge University Press, 2005.

[18] Donald E. Groom, Nikolai V. Mokhov, and Sergei I. Striganov. *Muon Stopping Power and Range Tables 10 MeV to 100 TeV. Atom.Data Nucl.Data Tabl.*, 78:183–356, 2001.

[19] J.F. Bak, A. Burenkov, J.B.B. Petersen, E. Uggerhoj, S.P. Moller, et al. *Large Departured from Landau Distributions for High-Energy Particles Traversing Thin Si and Ge Targets. Nucl.Phys.*, B288:681, 1987.

[20] D. Green. *The Physics of Particle Detectors.* Cambridge University Press, 2005.

[21] K. Kleinknecht. *Detectors for Particle Radiation.* Cambridge University Press, 1998.

[22] National Institute of Standards and Technology (NIST). Database for Elements, June 2009.

[23] W.W.M. Allison and J.H. Cobb. *Relativistic Charged Particle Identification by Energy Loss. Ann.Rev.Nucl.Part.Sci.*, 30:253–298, 1980.

[24] H. Bichsel and R. Saxon. *Comparison of Calculation Methods for Straggling in Thin Absorbers. Physical Review A*, 11:1286–1296, Apr 1975.

[25] H. Bichsel. *Straggling in Thin Silicon Detectors. Rev. Mod. Phys.*, 60:663–699, Jul 1988.

[26] H. Bichsel. *Comparison of Straggling Functions Calculated with Bethe-Fano, FVP and Rutherford Cross Sections. unpublished*, Nov 2011.

[27] `http://www.nobelprize.org/nobel_prizes/physics/laureates/1992/`, June 2009.

[28] C. Grupen and B. Shwartz. *Particle Detectors.* Cambridge Monographs on Particle Physics, Nuclear Physics and Cosmology. Cambridge University Press, 2011.

[29] J. Townsend. *The Conductivity Produced in Gases by the Motion of Negatively-Charged Ions. Nature*, 62:340–341, August 1900.

[30] J. Cooley. *Fundamentals of Undervoltage Breakdown Through the Townsend Mechanism* . PhD thesis, Princeton University, September 2008.

[31] G. Knoll. *Radiation Detection and Measurement.* Wiley, 2010.

[32] Y. Giomataris, P. Rebourgeard, J.P. Robert, and G. Charpak. *MICROMEGAS: A High Granularity Position-Sensitive Gaseous Detector for High Particle Flux Environments. Nucl.Instrum.Meth.*, A376:29–35, 1996.

[33] P. Horowitz and W. Hill. *The Art of Electronics.* Cambridge University Press, 1980.

[34] ATLAS. Luminosity Public Results, June 2009.

[35] CERN. LHC Introduction, June 2009.

[36] M. Hance and H. H. Williams. *Measurement of Inclusive Isolated Prompt Photon Production in Proton-Proton Collisions at* $\sqrt{s} = 7$ *TeV with the ATLAS Detector.* PhD thesis, Pennsylvania U., Philadelphia, 2011. Presented 11 Jul 2011.

[37] *ATLAS Muon Spectrometer: Technical Design Report.* Technical Design Report. CERN, Geneva, 1997.

[38] E. Diehl. *Calibration and Performance of the ATLAS Muon Spectrometer.* 2011.

[39] M. Iodice. *Calibration and Performance of the Precision Chambers of the ATLAS Muon Spectrometer.* Technical Report ATL-MUON-PROC-2011-009, CERN, Geneva, Nov 2011.

[40] P.s Bagnaia and et.al. *Calibration Model for the MDT Shambers of the ATLAS Muon Spectrometer.* Technical Report ATL-MUON-PUB-2008-004. ATL-COM-MUON-2008-006, CERN, Geneva, Feb 2008. backup paper for Atlas Detector paper.

[41] S. Martoiu, H. Muller, A. Tarazona, and J. Toledo. *Development of the Scalable Readout System for Micro-Pattern Gas Detectors and Other Applications. JINST*, 8:C03015, 2013.

[42] C. Bini. *Studies of Single Chamber MM Space Resolution.* 2012.

[43] M. Bigletti, M. Iodice, V. Lavorini, F. Petrucci, and M. Trovatelli. *Study of uTPC Single Chamber Spatial Resolution from July-August Test-Beam Data.* 2012.

[44] M. Trovatelli. *Study of uTPC Single Chamber Resolution from July Test-Beam Data.* 2012.

[45] M. Bigletti, M. Iodice, P. Petrucci, and M. Trovatelli. *APV25 Data Analysis*. 2012.

[46] H. Spieler. *Semiconductor Detector Systems*. Oxford Science Publications, 2005.

[47] T. Alexopolos, G. Iakovidis, K. Leontsinis, and K. Ntekas. *A Closer Look at the July-August12 Test-Beam Data (Angular Resolution, etc.)*. 2012.

[48] V. Radeka. *Shielding and Grounding in Large Detectors*. *JINST*, 1998.

[49] G. Cowan. *Statistical Data Analysis*. Oxford Science Publications, 1998.

[50] M. Bianco. *Development of Large-Size MicroMegas Detectors for the Upgrade of the ATLAS Experiment.*, June 2009.

[51] R. Barlow. *Statistics - A Guide to the Use of Statistical Methods in the Physical Sciences*. John Wiley & Sons, 1989.